



University of
Massachusetts
Amherst

Numerical Modeling of Fracturing in Non-Cylindrical Folds: Case Studies in Fracture Prediction Using Structural Restoration

Item Type	dissertation
Authors	Shackleton, John Ryan
DOI	10.7275/0x3m-hx17
Download date	2024-12-03 03:51:23
Link to Item	https://hdl.handle.net/20.500.14394/39278

**NUMERICAL MODELING OF FRACTURING IN NON-CYLINDRICAL
FOLDS: CASE STUDIES IN FRACTURE PREDICTION USING
STRUCTURAL RESTORATION**

A Dissertation Presented

by

JOHN RYAN SHACKLETON

Submitted to the Graduate School of the
University of Massachusetts Amherst in partial fulfillment
of the requirements for the degree of

DOCTOR OF PHILOSOPHY

May 2009

Department of Geosciences

© Copyright by John Ryan Shackleton 2009

All Rights Reserved

**NUMERICAL MODELING OF FRACTURING IN NON-CYLINDRICAL
FOLDS: CASE STUDIES IN FRACTURE PREDICTION USING
STRUCTURAL RESTORATION**

A Dissertation Presented

by

JOHN RYAN SHACKLETON

Approved as to style and content by:

Michele L. Cooke, Chair

Sanjay Raja Arwade, Member

Laurie L. Brown, Member

Jaume Vergés Masip, Member

Michael L. Williams, Department Head
Department of Geosciences

DEDICATION

This work is dedicated to my family who have supported me in every endeavor.

ACKNOWLEDGMENTS

I would like to acknowledge my adviser Michele Cooke for her patience, support, and especially for the encouragement to follow my own path in research and career. I would like to thank my committee members, Sanjay Arwade, Laurie Brown, and Jaume Vergés for their comments on this thesis. I would also like to thank Avivia Sussman, Gemma Lebraña, Conxita Taberner, and Toni Simo for advice and constructive comments in the field and on research papers.

The research would not have been possible without funding from the American Chemical Society's Petroleum Research Fund, Sigma Xi, American Association of Petroleum Geologists, the Geological Society of America, the University of Massachusetts, Amherst, and Midland Valley Exploration, Inc. This research would also not have been possible without my field assistants, Micheal Apfelbaum, Chris Gordon, and Scott Marshall, who spent countless hours collecting fracture and paleomagnetic data.

I would like to thank Ashley Griffith, Micheal Apfelbaum, Scott Marshall, Patrick Diggins, Kat Plourde, and Laura Dair for constructive research discussions and less constructive time outside of the office.

I would also like to thank John Jackson and Peg Piwonka for their constant friendship and support during my time in Amherst.

ABSTRACT

NUMERICAL MODELING OF FRACTURING IN NON-CYLINDRICAL FOLDS: CASE STUDIES IN FRACTURE PREDICTION USING STRUCTURAL RESTORATION

MAY 2009

JOHN RYAN SHACKLETON, B.S., UNIVERSITY OF THE SOUTH

M.S., UNIVERSITY OF ALASKA, FAIRBANKS

Ph.D., UNIVERSITY OF MASSACHUSETTS AMHERST

Directed by: Professor Michele L. Cooke

This thesis contains several distinct studies aimed at better understanding fracturing in compressional fault-cored folds.

At outcrops of growth strata in the Oliana anticline in the Spanish Pyrenees, the relationship of two joint sets may reflect changing mechanical properties (i.e. via diagenesis) during the folding process. Using a Schmidt hammer, I assess the rigidity contrast between the individual units and suggest that late-stage, throughgoing joints formed in strata with conditions similar to those of the present day and that early, bed-contained joints formed when the rigidity contrast between beds was significantly greater than the present day contrast.

Modeling algorithms that are used for fracture prediction assume plane strain to construct, model and restore fault-cored folds. Using mechanical models that allow heterogeneous transport in three dimensions, I explore the distribution and magnitude of out-of-plane transport in plunging fault-cored anticlines and provide guidelines of where plane strain should and should not be applied. I show that out-of-plane transport

is significant in the simplest non-cylindrical folds, and suggest that complex non-cylindrical structures should not be modeled using plane strain.

I mapped five bed-orthogonal fracture sets associated with folding and faulting events at Sant Corneli anticline, a non-cylindrical, fault related anticline in the Spanish Pyrenees. Fold axis perpendicular, calcite healed joint sets associated with similarly oriented normal faulting both pre-date, and are cross cut by calcite healed, N-NW striking joints. Later bed strike oblique joint sets are distinguished by the presence of iron oxide mineralization that probably occurred during Paleocene-Oligocene time. This study directly links fold-related fracturing to fold evolution because fracture sets can be dated relative to the structural evolution of the anticline.

I use three-dimensional restorations of Sant Corneli anticline in the Spanish Pyrenees to test the fracture prediction capability of a fully three-dimensional finite element geomechanical restoration algorithm. Reconstruction of the three-dimensional architecture of the syn-tectonic strata provides a template for incrementally unfolding the anticline. Strains predicted by the restorations are compared to the fracture sets that formed over the corresponding time intervals, which are consistent with the observed fracture patterns at Sant Corneli anticline.

TABLE OF CONTENTS

	Page
ACKNOWLEDGMENTS	v
ABSTRACT.....	vi
TABLE OF CONTENTS.....	viii
LIST OF TABLES.....	xi
LIST OF FIGURES	xii
 CHAPTER	
1. EVIDENCE FOR TEMPORALLY CHANGING MECHANICAL STRATIGRAPHY AND EFFECTS ON JOINT-NETWORK ARCHITECTURE	1
1.1 Introduction.....	1
1.2 Mechanical stratigraphic controls on fracture networks.....	2
1.3 Recognition of changing mechanical stratigraphy using joint patterns.....	3
1.4 Stratigraphy and joint patterns at the Oliana Anticline	4
1.5 Rigidity contrast at the Oliana Anticline	6
1.6 Interpretation of joint patterns and rigidity contrast at the Oliana Anticline.....	7
1.7 Implications for past and future studies of jointing related to mechanical stratigraphy	8
1.8 Figures	10
2. WHEN IS PLANE STRAIN A VALID ASSUMPTION IN NON-CYLINDRICAL FAULT-CORED FOLDS?	14
2.1 Introduction.....	14
2.2 Methodology.....	16
2.3 Model Results	18
2.3.1 Final fold and fault shape.....	19
2.3.2 Displacement Vectors	20
2.3.3 Percentage of Out-of-Plane Displacement.....	22
2.3.4 Normalized Ratio of Out-of-Plane Transport	23
2.4 Effect of friction coefficient and spacing of bed slip surfaces on fold shape	25
2.5 Discussion.....	27

2.6 Conclusions.....	30
2.7 Figures	32
3. TEMPORAL CONSTRAINTS ON FRACTURING ASSOCIATED WITH FAULT RELATED FOLDING AT SANT CORNELI ANTICLINE, SPANISH PYRENEES	42
3.1 Introduction.....	42
3.2 Tectono-stratigraphic evolution of the Sant Corneli anticline.....	45
3.3 Stratigraphic history.....	46
3.4 Fold/Thrust Structure of Sant Corneli anticline.....	49
3.5 Secondary Faulting at Sant Corneli anticline	52
3.6 Field mapping of fractures at Sant Corneli anticline	55
3.7 Fractures in the Aren group	57
3.7.1 N-NW striking calcite filled joints (J2)	57
3.7.2 NE striking deformation bands (DB1).....	57
3.7.3 N-NE striking, calcite filled joints (J1/J3).....	58
3.7.4 W-NW striking, locally calcite filled joints (J4).....	58
3.7.5 E-NE striking locally calcite filled joints (J5)	59
3.8 Fractures in the Sant Corneli Sequence	59
3.8.1 Bed strike-perpendicular calcite filled joints (J1/J3).....	60
3.8.2 Bed strike-oblique, calcite filled joints with iron oxidation (J4)	61
3.8.3 Bed strike-oblique, calcite filled joints with iron oxidation (J5)	61
3.9 Discussion and Interpretations of Fold-Fracture Evolution.....	62
3.9.1 J1/J3 Joints.....	62
3.9.2 J2 Joints.....	64
3.9.3 DB1 Deformation Bands.....	65
3.9.4 J4/J5 Joints.....	65
3.10 Implications for the tectonic history of the Sant Corneli-Bóixols anticlines	67
3.11 Conclusions and implications for studies of fold related fracturing, faulting, and fluid flow	68
3.12 Figures	71
4. VALIDATION OF STRUCTURAL RESTORATION TECHNIQUES USING INCREMENTAL RESTORATION OF A WELL CONSTRAINED RESERVOIR ANALOG: SANT CORNELI ANTILCINE (SPAIN)	92

4.1 Introduction.....	92
4.2 Reconstruction of Sant Corneli anticline.....	96
4.3 Restoration of Sant Corneli anticline.....	102
4.3.1 Construction of initial restoration template surfaces.....	102
4.3.2 Restoration step 1.....	104
4.3.2.1 Finite element meshing.....	104
4.3.2.2 Boundary conditions.....	105
4.3.2.3 Geometry of the restored strata.....	106
4.3.2.4 Fault and fracture prediction.....	106
4.3.3 Restoration step 2.....	108
4.3.3.1 Geometry of the restored strata.....	108
4.3.3.2 Fault and fracture prediction.....	109
4.3.4. Discussion.....	110
4.3.4.1 Restoration step 1.....	110
4.3.4.2 Restoration step 2.....	111
4.4 Conclusions and implications for fracture prediction in fault related folds.....	113
4.5 Figures	114
 APPENDIX: METHODOLOGY FOR SCHMIDT DATA COLLECTION AND CONVERSION OF SCHMIDT REBOUND TO SHEAR MODULUS	133
 BIBLIOGRAPHY.....	137

LIST OF TABLES

Table	Page
Table 4.1 Elastic parameters assigned to volumes in the restorations.....	124
Table A1. Published Schmidt rebound, Dry unit weight, Young's modulus, and Poisson's Ratio Data for clastic sedimentary rocks	135

LIST OF FIGURES

Figure	Page
1.1 Geologic map of Oliana anticline.	10
1.2 Cartoons of joint patterns resulting from constant (A and B) and temporally varying (C and D) mechanical stratigraphy.....	11
1.3 Photograph of outcrop with overlaid stratigraphic section and fracture patterns.....	12
1.4 Rigidity profile with stratigraphic section.	13
2.1 Cartoon of a pseudo three-dimensional representation of a three-dimensional structure.....	32
2.2 Incrementing infinitesimal elastic strains to produce finite deformation observed in natural folds.....	32
2.3 Initial setup of the two models.....	33
2.4 Fold shape of two reference horizons within Models 1 and 2.....	34
2.5 Map view of horizontal component of displacement vectors for the two reference horizons superposed onto contour map of fold shape.....	35
2.6 North-south cross sections perpendicular to the contraction direction and parallel to fault strike show displacement vectors superposed on density plots of percentage of out-of-plan transport.....	36
2.7 Schematic diagram of vector components.....	37
2.8 Map view of the percentage of out-of-plane displacement for each point on the reference horizons (thick white contours) overlain on a map of fold shape (shaded with grey contours).....	38
2.9 Ratio of out-of-plane displacement to the average vector magnitude for each horizon (thick white contours) superposed on shaded and contoured (thin lines) map of fold shape.....	39
2.10 North-south cross-section showing the ratio of out-of-plane displacement to the average displacement magnitude within the vertical section.....	40

2.11 Surface uplifts for four different frictional bed slip boundary conditions in FRIC2D.	41
3.1 Generalized map of the Spanish Pyrenees showing the location of the major thrusts.	71
3.2 Geologic map of the Sant Corneli-Boixols-Nargo anticline.	72
3.3 Digital elevation model with orthophoto drape of Sant Corneli anticline.	73
3.4 Simplified stratigraphic section showing the major stratigraphic sequences.	74
3.5 Geologic map of the study area showing the major structural elements and stratigraphic sequences.	75
3.6 Simplified paleogeography and structural evolution of the study area.	76
3.7 Cross sections through Sant Corneli anticline along or near the ECORS transect.	77
3.8 Photos of normal faults in the field area.	78
3.9 View northwest at a pavement outcrop in the Montesquiu sequence near Orcau.	79
3.10 Close up view of calcite fill of J2 joints cross cut by deformation bands (DB1) in pavement view.	80
3.11 Map of J2 joint strikes in the study area.	81
3.12 Map of deformation band strikes in the study area.	82
3.13 J2 joints cross cutting J1 joints in the Montesquiu sequence.	83
3.14 Map of J1/J3 strikes in the study area.	84
3.15 Map of J4 strikes in the study area.	85
3.16 View northwest at a pavement outcrop in marls of the Montesquiu sequence showing relationships of joints to bed strike.	86
3.17 Bed-strike oblique (east) view of a pavement outcrop J4 joints showing reddish goethite “haloes”.	87
3.18 Secondary lisegang banding associated with a J5 joint.	88

3.19 Map of J5 strikes in the study area.	89
3.20 Photograph of an oblique cross section through bedding showing the relationship of J1/J3 to J4/J5 joints in the backlimb of the Sant Corneli Sequence.	90
3.21 Simplified interpretive sketch of joints at Sant Corneli anticline showing the orientations of joints with respect to bedding and structural position.	91
4.1 Sant Corneli sequence near the topographic surface.	114
4.2 Sant Corneli sequence at depth.	115
4.3 Vallcarga sequence.	116
4.4 Montesquiú sequence.	117
4.5 Orcau-Vell unconformity.	118
4.6 Orcau-Vell sequence.	119
4.7 Santa Engracia sequence.	120
4.8 Horizontal slice showing the surface constraint on upwardly projected portions of the reconstruction (NW view).	121
4.9 Creation of restoration surfaces.	122
4.10 Setup for restoration step 1.	123
4.11 Restored geometries for the first restoration step showing the differences between flexural and no flexural slip conditions.	125
4.12 Expanded view of the restored geometries for the first restoration step with the upper Santa Engracia sequence removed.	126
4.13 Comparison of fracture strike predictions from restoration step 1 to observed joint sets.	127
4.14 Setup for restoration step 2.	128
4.15 Restored geometries for the second restoration step showing the differences between flexural and no flexural slip conditions.	129

4.16 Restored geometries for the second restoration step with the lower Santa Engracia and Orcau-Vell sequences removed.	130
4.17 Comparison of fracture strike predictions from restoration step 2 to observed joint sets.	131
4.18 Comparison of fracture strike predictions from step 2 of the flexural slip restoration to young joint sets.	132
A1 Regression line with 95% confidence range (red lines) for converting γ_{2R} to shear modulus (μ)	136

CHAPTER 1

**EVIDENCE FOR TEMPORALLY CHANGING MECHANICAL
STRATIGRAPHY AND EFFECTS ON JOINT-NETWORK ARCHITECTURE**

1.1 Introduction

Whether joints cross many sedimentary layers or terminate at frequent bed surfaces to produce tortuous subsurface flow paths is a consequence of the mechanical properties of the strata that control joint propagation, i.e. the mechanical stratigraphy (e.g. Corbett et al. 1987, Gross et al. 1995, Hanks 1997, Lorenz et al. 2002, Narr & Suppe 1991, Rijken & Cooke 2001, Underwood et al. 2003). Attributes of a stratigraphic section that define its mechanical stratigraphy include the rigidity of each lithologic unit, the relative thicknesses of individual layers, and the nature of the interfaces between those layers (Cook & Erdogan 1972, Gross 1995, Helgeson & Aydin 1991, Ladeira & Price 1981, Lorenz et al. 2002, Underwood et al. 2003).

Whereas previous studies of jointing in stratigraphic sections have presumed that mechanical stratigraphy remains constant throughout fracturing events, I propose that some stratigraphic sections undergo a variety of diagenetic processes during structural deformation that would alter mechanical stratigraphy and give rise to distinct and potentially complex three-dimensional joint networks. Thus, the interpretation of joint networks requires considering potential diagenetic changes to rock properties. Furthermore, because joints in tight sedimentary strata serve as conduits for subsurface fluid flow, constraining temporally changing mechanical stratigraphy is relevant to a

variety of problems including hydrocarbon migration, groundwater-contaminant migration, and basin-scale brine fluxes in foreland fold-and-thrust belts.

Growth strata, such as exposed at the Oliana anticline (Fig. 1.1) in the central Spanish Pyrenees, provide an exemplary setting for investigating changing mechanical stratigraphy during deformation. In syn-deformational strata, jointing can occur at different stages of diagenesis and simultaneous folding can rotate beds so that later joints do not parallel early joints (Fig. 1.2C); this facilitates recognition of distinct joint sets. I have observed two such joint sets in an exposure at the Oliana anticline that demonstrate different bed intersections: one set is contained within beds and another set crosscuts multiple layers. An examination of the rigidity contrast between adjacent interbedded fine and very fine sandstone investigates the hypothesis that this joint network architecture reflects temporal changes of the relative rigidity of adjacent layers.

1.2 Mechanical stratigraphic controls on fracture networks

The architecture of joint networks is controlled by the ability of lithologic contacts to inhibit joint propagation; two primary factors control the propagation of joints across lithologic contacts: (1) interface strength (Cooke & Underwood 2001, Helgeson & Aydin 1991, Renshaw & Pollard 1995, Underwood et al. 2003), and (2) contrast between the rheology of the layers (Cook & Erdogan 1972, Erdogan 1972, Rijken & Cooke 2001). Analog and numerical experiments suggest that weak interfaces inhibit joint propagation by sliding or opening, thereby reducing the stress singularity at the crack tip (e.g. Cooke & Underwood 2001, Renshaw & Pollard 1995). Additionally, cracks may terminate at contacts with softer or more ductile layers as the stress

singularity at the crack tip is dissipated within the softer layer (Erdogan 1972, Renshaw & Pollard 1995, Rijken & Cooke 2001).

Renshaw and Pollard (1995) calculated guidelines for the degree of rigidity contrast needed to reduce the crack-tip stress singularity and promote termination of joints at strong contacts. If the shear modulus ratio of softer to stiffer layer ($\mu_{\text{soft}}/\mu_{\text{stiff}}$) is < 0.4 , the stress singularity at the crack tip within the stiffer layer is significantly less than that of a crack propagating within a homogeneous layered sequence ($\mu_{\text{soft}}/\mu_{\text{stiff}} = 1$). Thus, joints will propagate across a bonded horizon when the rigidity contrast in adjacent units is low (i.e., a high ratio of $\mu_{\text{soft}}/\mu_{\text{stiff}} > \sim 0.4$) (Fig. 1.2B), whereas joint termination is favored when $\mu_{\text{soft}}/\mu_{\text{stiff}} < \sim 0.4$ (Fig. 1.2A). Because the ratio of shear moduli can be assessed for rock sequences, I can confirm the criterion for exposed jointed sequences and/or predict jointing in subsurface sequences. For example, in layered sequences with well-bonded interfaces, joints that cross interfaces at high angles should primarily be present in units whose ratio of shear moduli is $> \sim 0.4$.

1.3 Recognition of changing mechanical stratigraphy using joint patterns

Until now, temporally changing mechanical stratigraphy has gone unrecognized because the rocks I observe only demonstrate the present-day mechanical properties. If exposures are selected to minimize weathering effects, the measured rigidity of a given rock layer only reveals information about the final stage of the layer's diagenetic and deformational history; prior stages of rigidity must be inferred. However, indirect inference of rheology is possible by using joint termination patterns within a stratigraphic section. For example, if I observe a stratigraphic section with strong

contacts where all of the bed-perpendicular joint sets are contained within individual bedded units (Fig. 1.2A), the rigidity contrast between those bedded units at the time of jointing should have been relatively high (i.e., a low ratio of $\mu_{\text{soft}}/\mu_{\text{stiff}} < \sim 0.4$) (Renshaw & Pollard 1995).

Consider the case where I observe two types of bed-perpendicular joint patterns, one joint set that is contained within beds and another that crosscuts the same bed interfaces (Figs. 1.2C and 1.2D). In this case, the rigidity contrast between units must have changed between jointing episodes, because the two joint sets imply different mechanical conditions, one with a high rigidity contrast and the other with a low rigidity contrast between beds. In other words, the two joint sets could not have formed coevally under similar mechanical stratigraphic conditions.

Whereas direct measurement of paleo-rigidity contrasts is impossible, the present-day rigidity contrast can be measured *in situ* or in laboratory experiments. Furthermore, the present-day rigidity contrast should be most consistent with the youngest joint set. Comparing measured rigidity contrast with the rigidity contrast implied by joint-set geometry can support my assertions that joint sets can be used to determine the paleo-rigidity contrast.

1.4 Stratigraphy and joint patterns at the Oliana Anticline

Located in the south-central Spanish Pyrenees, the Oliana anticline is a 15-km-long, northeast-trending, doubly plunging anticline (Fig. 1.1). The anticline is composed mainly of four upper Paleogene syntectonic units (Fig. 1.1), which include conglomerates, mudstones, and siltstones, and is cored by a duplex that has repeated the

Eocene Igualada marls. During the Oligocene, the whole structure was transported ~11 km southward along a detachment in the Eocene Cardona evaporites (Burbank et al. 1992, Vergés 1993, Vergés & Muñoz 1990).

This study focuses on one outcrop along the northwest limb of the Oliana anticline that was analyzed through detailed measurement of stratigraphic sections, characterization of joint systems, and rebound hammer testing (Fig. 1.1).

Stratigraphically, the outcrop consists of interbedded siltstones, very fine grained sandstones, and fine grained sandstones bounded by pebble and cobble conglomerates (Fig. 1.3). Compositionally, the sandstone-siltstone package is relatively uniform, consisting of almost entirely subrounded, poorly sorted, light gray and light brown quartz sand and silt.

The three fine grained sandstone units (labeled on Fig. 1.3) are resistant and have positive relief in outcrop. Contacts between the fine grained sandstones and the surrounding siltstones and very fine grained sandstones are generally gradational, without a sharp break between lithologies, although two sharp contacts were observed (dark lines in the stratigraphic section in Fig. 1.3). These contacts appear to be minor erosional surfaces, and no mudstone or shale is apparent between the two units. Because gradational contacts do not typically slide or open, I consider the majority of contacts in the sequence to be relatively strong.

Characterization of fractures reveals two distinct sets of joints: one set of bed-contained joints and another set of throughgoing joints that crosscut all bed contacts (Fig. 1.3). The bed-contained joints strike east, oblique to both the northeast-trending Oliana fold axis and the local northeast-striking bedding (Fig. 1.3). These steeply

dipping joints are restricted almost entirely to the resistant fine grained sandstone units in the outcrop. In contrast, the throughgoing joints, range in length from a few tens of centimeters to a few meters, range in strike from north to north-northeast and are oblique to the fold axis and to bed strike.

The differing orientations of the two joint sets imply two distinct jointing episodes. Sussman (2002) interpreted the throughgoing joints, which are parallel to large-scale joints observed within the youngest synorogenic unit in the area (unit 4 in Fig. 1.1), as the youngest joint set at the Oliana anticline.

1.5 Rigidity contrast at the Oliana Anticline

To assess the *in situ* rigidity of the different jointed beds I used a Schmidt Mechanical Concrete Test Hammer, which measures the rebound of a piston striking the outcrop (Hucka 1965, Poole & Farmer 1980). Empirical relationships allow conversion of rebound number (R) to shear modulus (rigidity) of each stratigraphic unit (Fig. 1.4, Appendix A). Inaccuracies of the Schmidt hammer and the empirical relationships may not establish precise rigidity; however, this assessment can be used to determine the relative rigidity of units. Because Schmidt hammer tests could not be obtained at every stratigraphic interval, calculation of the rigidity contrast across each contact was not possible. Consequently, I determine the overall rigidity contrast between the less rigid very fine grained sandstones (the white beds in Fig. 1.4) and the resistant and more rigid fine grained sandstones (the gray beds in Fig. 1.4) by averaging the two groups of data. The ratio of the two values yields an average rigidity contrast of

0.57 (Fig. 1.4), indicating that at present-day the very fine sandstone and fine sandstone beds are not greatly different in their rigidity.

1.6 Interpretation of joint patterns and rigidity contrast at the Oliana Anticline

The presence of distinct bed-contained and throughgoing joint sets at the same outcrop suggests that the mechanical stratigraphic conditions changed between episodes of jointing. Furthermore, my rebound hammer measurements suggest that the present-day rigidity contrast between the adjacent units ($\mu_{\text{very fine sand}}/\mu_{\text{fine sand}} = 0.57 > 0.4$) is not sufficient to terminate propagating joints in this stratigraphic section with strong contacts. These results are consistent with the interpretation that the throughgoing joints are the youngest set and formed within mechanical stratigraphy similar to the present-day conditions. Furthermore, the present-day rigidity contrast cannot account for bed-contained joints that terminate at the interfaces between fine grained sandstone and very fine grained sandstone, suggesting that these joints formed when the beds exhibited greater rigidity contrast. For example, the very fine grained sandstones may have been significantly softer than the fine sandstone when the bed-contained joints formed.

A possible scenario for the mechanical stratigraphic evolution at the Oliana outcrop can be assembled by considering likely diagenetic changes within the stratigraphic section. I propose that the fine grained sandstones, which had higher porosity and permeability than the finer units, may have been susceptible to early fluid-precipitated cementation that strengthened the units relatively early in the burial history (e.g. Holbrook 2002). During this time, the very fine grained sandstone may have remained relatively poorly lithified, resulting in a rigidity contrast that was sufficient to

stop propagating joints (David et al. 1998). Later, deeper burial, fluid flux, and compaction of the finer-grained sediments may have strengthened the finer-grained units, thus decreasing the rigidity contrast between the units and allowing throughgoing joints to cross bed contacts (e.g. David et al. 1998, Holbrook 2002). Mechanisms for increasing the rigidity of these units probably include consolidation, dewatering, minor geothermal heating, cementation by mineral precipitation, and recrystallization due to pressure solution (e.g. David et al. 1998, Houseknecht 1987, Maxwell 1960).

1.7 Implications for past and future studies of jointing related to mechanical stratigraphy

Temporally changing mechanical properties may be frequently unrecognized. These changes are probably not restricted to sedimentary environments with growth strata because diagenetic processes occur in many geologic settings. For example, in carbonate sequences, calcite twinning, recrystallization of aragonite to calcite, and dolomitization may significantly alter the rigidity contrast between units (e.g. Eberli et al. 2003, Hanks 1997). In pyroclastic units, processes such as welding and compaction occur simultaneously with thermal cooling and degassing, resulting in a linked deformational and depositional setting in which rigidity contrast is likely to change rapidly through time (e.g. Dunne et al. 2003, Quane & Russell 2002).

The growth strata at the Oliana anticline provide a superlative natural laboratory in which to infer changing mechanical stratigraphic conditions because the two joint sets can be distinguished by their differing orientations (e.g. Fig. 1.2C). Had the two joint sets formed under a similarly oriented stress field, they would have had similar strikes and would seem temporally related despite their differing terminating

relationships with respect to bedding. Figure 1.2D shows two joint sets that are different in their bed intersections, but similar in orientation. I suspect that field geologists (including ourselves!) have grouped such joint sets as one set because of their similar orientation (e.g. Underwood et al. 2003). Further studies relating joint patterns to rigidity contrast and/or interface strength may also reveal the relative ubiquity of temporally changing mechanical stratigraphy.

1.8 Figures

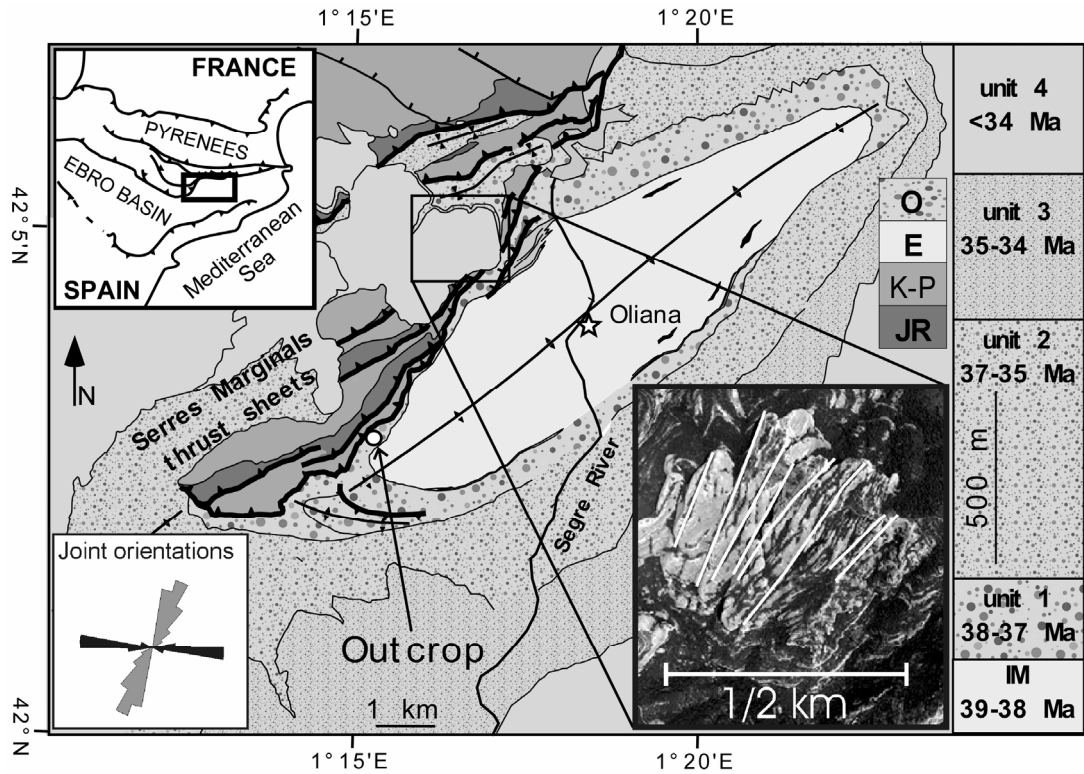


Figure 1.1 Geologic map of Oliana anticline. Location of outcrop is shown in inset map in upper left. Aerial photograph inset shows the orientation of major regional joint sets located in the light-colored youngest growth-strata unit (unit 4). These joints parallel the throughgoing joints observed at my study outcrop (north-northeast joint strike is shown in gray on rose diagram). The black joint strikes on the rose diagram represent bed-contained joints. O—Oligocene; E—Eocene; K-P—Cretaceous-Paleogene; JR—Jurassic; IM—Igualada Marls (modified from Vergés, 1993).

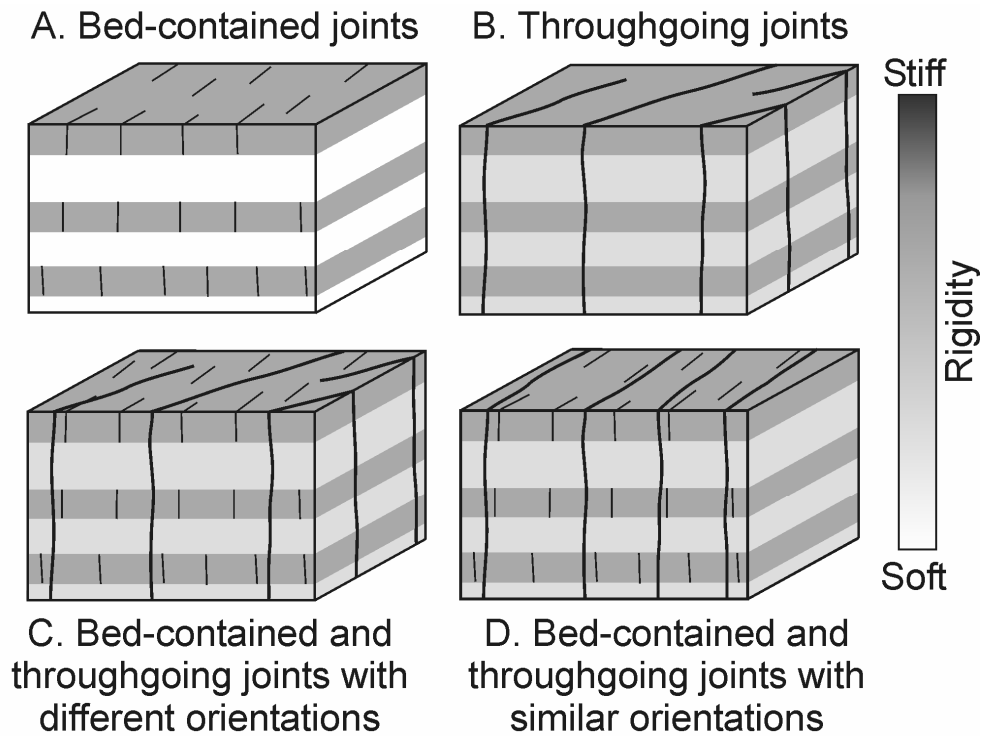


Figure 1.2 Cartoons of joint patterns resulting from constant (A and B) and temporally varying (C and D) mechanical stratigraphy. Bed-contained joints in A form as rigidity contrast between beds is high, whereas throughgoing joints in B form in low rigidity contrast beds. Joint patterns in C and D imply that bed-contained joints formed at one time, when rigidity contrast was high, and that throughgoing joints formed at another time when rigidity contrast was low. Although the observed variations in joint spacing among layers in D could be accounted for by differing degrees of joint infilling, infilling can only influence joint spacing and cannot account for different joint intersections with bedding.

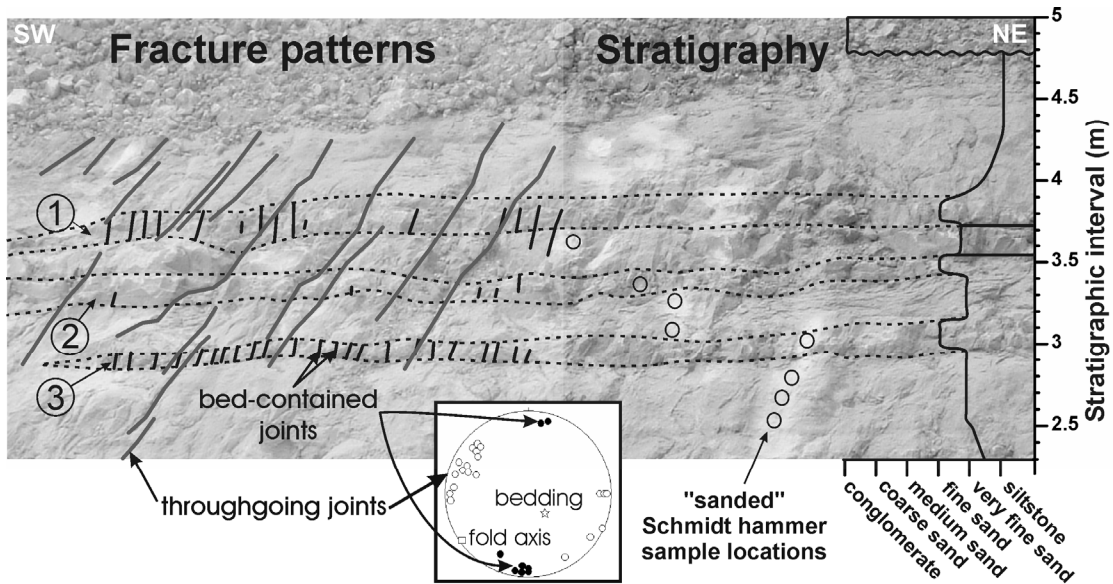


Figure 1.3 Photograph of outcrop with overlaid stratigraphic section and fracture patterns. Schmidt hammer sample locations are shown as unfilled circles to left of stratigraphic section. Siltstones and very fine grained sandstones are interbedded with resistant fine grained sandstone beds that are numbered 1–3 on left side of photograph. Fracture patterns (marked only on left side of photograph): bed-contained joints—black lines and filled black circles on equal-area stereonet; throughgoing joints—gray lines and open circles on stereonet. The mean angle between bedding and joints is 69° for bed-contained joints and 77° for throughgoing joints. Gradational bed contacts are shown as dashed lines.

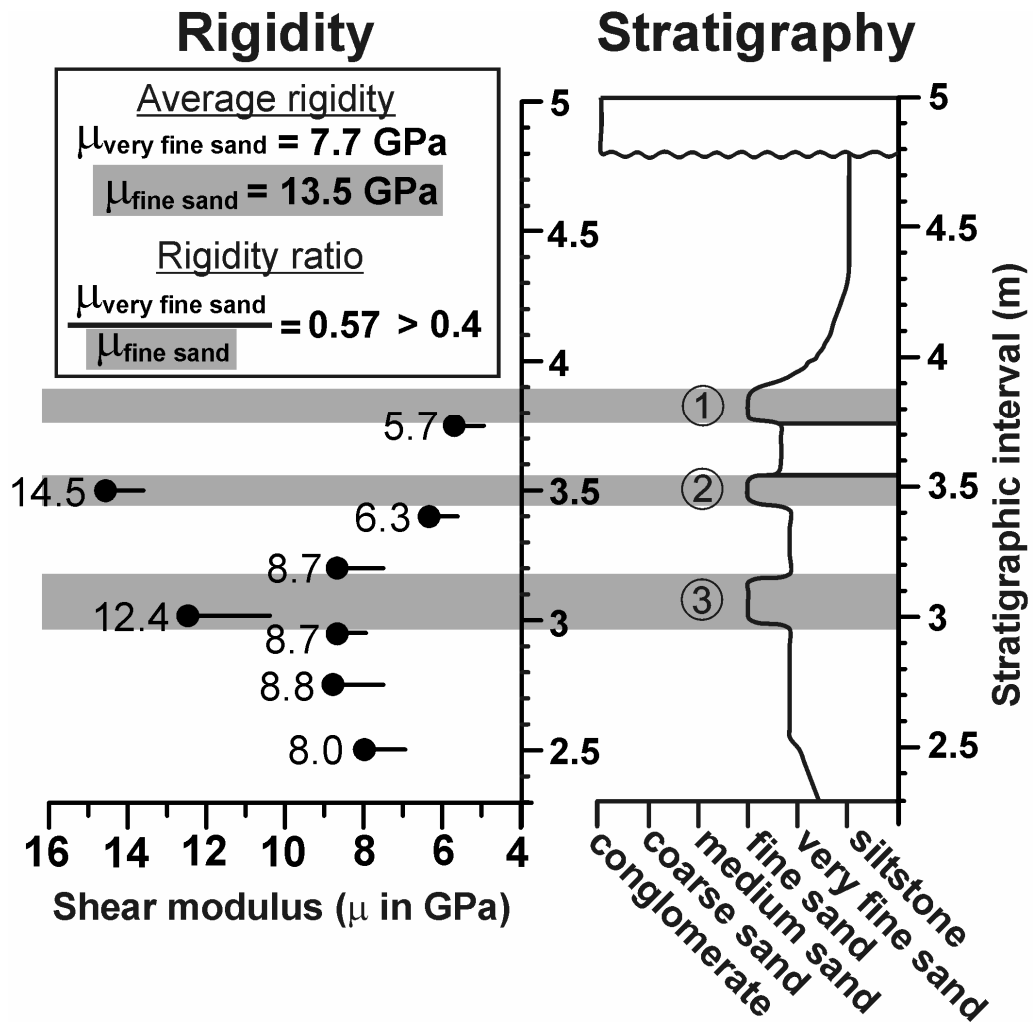


Figure 1.4 Rigidity profile with stratigraphic section. Beds 1–3 (shown in gray) correlate with those in Figure 1.3. The numerically labeled dots indicate maximum shear modulus at each sample location; the largest values measured are considered the most reliable (Poole and Farmer, 1980). Bars indicate the range of possible rigidity indicated by the Schmidt rebound hammer data.

CHAPTER 2

WHEN IS PLANE STRAIN A VALID ASSUMPTION IN NON-CYLINDRICAL FAULT-CORED FOLDS?

2.1 Introduction

Analysis, restoration, and modeling of geologic faults and folds has traditionally been performed on two dimensional cross-sections due to limited techniques for cross-section balancing and construction, as well as computational constraints on forward modeling and restoration. Many current techniques for analyzing three-dimensional models of geologic structures rely on interpolation between serial cross sections to forward model and restore what are termed “pseudo three-dimensional,” or “2D-3D” geologic surfaces (Fig. 2.1) (Bernal & Hardy 2002, Cristallini & Allmendinger 2001, Epard & Groshong 1995, Fischer & Wilkerson 2000, Griffiths et al. 2002, Salvini & Storti 2002). Pseudo three-dimensional models are invaluable for reconstruction of three-dimensional surfaces, but are still bound by the constraint of plane strain and therefore may neglect some inherently three-dimensional aspects of doubly plunging folds (Fig. 2.1a). For example, a common technique for flexural slip unfolding utilizes serial transport planes to geometrically restore three-dimensional surfaces while conserving three-dimensional volume, line length in the transport plane, and orthogonal bed thickness (Griffiths et al. 2002). In this case, the choice of template horizon and location of a fixed pin control the unfolding process and govern the outcome of the restoration.

Pseudo three dimensional restoration and forward modeling of fault-cored folds is appropriate in cylindrical folds where plane strain conditions limit displacement to within a single transport plane, but is not valid in non-cylindrical folds. During the development of non-cylindrical folds a component of out-of-plane motion may develop where material displacement vectors deviate from the transport plane. While out-of-plane transport is very difficult to document in natural folds due to lack of traceable markers, out-of-plane transport has been documented in analog and numerical models (Fischer & Keating 2005, Medwedeff & Krantz 2002, Strayer & Suppe 2002). Because many natural structures display complex, non-cylindrical geometries, an evaluation of the validity of pseudo three-dimensional modeling and restoration methods is needed. Of specific importance is an evaluation of where plane strain can be assumed and how much error will result from assuming plane strain where displacements deviate from the general transport plane.

In the same manner that the choice of pin plane and bed slip system govern the outcome of geometric restorations in two dimensions, I also expect bedding parallel slip to influence the fold shape and particle motion trajectories of three-dimensional mechanical models. Laboratory experiments and natural folds show the strong dependency of fold shape and style on the spacing and density of interlayer slip surfaces (e.g. Chester et al. 1991, Erickson 1996, Johnson & Johnson 2000, Ramsay & Huber 1987). Not coincidentally, flexural slip or layer parallel shear is a fundamental aspect of many two-dimensional geometric and kinematic models for fault related folding (Epard & Groshong 1995, Erslev 1991, Suppe 1983, Suppe & Medwedeff 1990). Despite the recognition that bed slip directly influences fold style, to my knowledge, no

studies to date have evaluated the effect of three-dimensional bed parallel slip on fold shape, nor evaluated the influence of bed slip on out-of-plane transport.

In order to evaluate the validity of the plane strain assumption in non-cylindrical folds, I have constructed two three-dimensional Boundary Element Method models of simple non-cylindrical folds with and without slipping bed surfaces. Using a new technique of incrementally releasing infinitesimal strains and subsequently incrementing displacement on a subsurface fault I am able to model large strains and simulate folds with more realistic amplitudes that can be directly compared to natural folds (Fig. 2.2). My goal is to evaluate the magnitude, structural position, and controls on the distribution of out-of-plane transport in three-dimensional folds and provide guidelines of where pseudo three-dimensional models should and should not be applied. I show that out-of-plane transport is significant in the simplest non-cylindrical folds, and I suggest that complex non-cylindrical structures should not be modeled using plane strain. I also show that bedding slip surfaces exert a significant control on the magnitude and structural position of out-of-plane transport in my models.

2.2 Methodology

This study utilizes the Boundary Element Method (BEM) code Poly3D (Thomas 1994), which solves the governing equations of continuum mechanics for faults in a uniform, linear-elastic half space representing the earth's upper crust. Three-dimensional BEM models (Crouch & Starfield 1990) can solve for the complete three-dimensional deformation of fault-cored folds. Faults in the model are discretized into triangular elements on which either slip and opening or shear and normal tractions can

be prescribed. Such tractions can be imposed by a remote stress or strain on the model. Due to the constraints of linear elasticity, Poly3D evaluates stresses most accurately for infinitesimal strains ($<1\%$), which produce folds of relatively small amplitude (Savage & Cooke 2003). Comparison of BEM models to natural folds with relatively large amplitudes typically requires qualitative comparison between modeled small scale folds and natural folds, or prescribing slip to a subsurface fault in a displacement boundary value problem (Maerten 1999, Maerten 2001, Maerten et al. 2000, Savage & Cooke 2003).

In order to model folds with realistic amplitudes, I have developed an innovative method of incrementally adding infinitesimal strains to the faults and surrounding rock body (Fig. 2.2). At the initial step in the model, a remote strain is applied to faults in a linear elastic half space. Faults are allowed to slip freely, but not open or interpenetrate. Slip on the faults resulting from the applied remote strain produces both displacements in the surrounding linear elastic half space and rotations and translations of the fault surface itself (Fig. 2.2). Displacements within the half space can be recorded by specifying observation points along initially horizontal surfaces representing bedding; these points can be traced during subsequent deformation.

The newly displaced faults and observation points form the input for the next step of the incremental model. At the start of each increment, the model is unstressed so that stresses accumulated in the previous step are assumed to completely dissipate. Inelastic processes such as microcracking, calcite twinning, and pressure solution may dissipate stresses at slow rates during folding. I approximate these inelastic processes by allowing stresses to relax between elastic growth increments. Iterating the process

with constant increments of remote strain produces folds of realistic amplitude and maintains accuracy of the mechanical model. The method also allows us to examine the finite deformation of interacting faults and slipping bedding planes during folding.

In order to simulate fault related folding and examine the effect of bed parallel slip on out-of-plane transport, I compare two fault models. Both models have a 35° dipping, elliptical fault that is elongate in the strike direction and centered at 4 kilometers depth. Model 1 has only the elliptical fault in a uniform elastic half space (Fig. 2.3). Model 2 is constructed with two freely slipping bed surfaces (initially horizontal at 2 and 1 kilometer depths) between the elliptical fault and the model's free surface (Fig. 2.3). These models represent two scenarios within a continuum from no bed slip to significant slip along beds overlying the fault. To simulate sedimentary rocks near the earth's surface, I have assigned shear modulus of 15,000 MPa and 0.25 for Poisson's Ratio (Birch 1966). Each model undergoes 50 increments of 1% strain, with the horizontal remote contraction parallel to the dip direction of the elliptical fault, and zero remote shear and zero remote strike parallel strain.

2.3 Model Results

I qualitatively compare fold shape and displacement trajectories at the two reference horizons in the models and in cross sections (Figs. 2.4-2.6). To evaluate the influence of bed parallel slip on out-of-plane transport, I quantitatively compare the percentage of out-of-plane transport for each reference horizon, and normalize the out-of-plane displacement to account for differences in displacement vector magnitude (Figs. 2.7-2.10).

2.3.1 Final fold and fault shape

After 50 increments of strain, both models produce a prominent doubly-plunging anticline above the upper fault tip (Fig. 2.4). Model 1 has a broad anticline with low limb dips and small amplitude (Fig. 2.4A and 2.4C). The deeper horizon has similar shape to the shallow horizon, but slightly greater amplitude, indicating amplitude increase with proximity to the fault tip. With the inclusion of bed slip surfaces in Model 2 (Fig. 2.4B and 2.4D), the amplitude of folding increases significantly; that the difference in amplitude between the two models is more than 300 meters. The fold width to strike length ratios are also significantly different as flexural slip tightens the fold (Fig. 2.4) (Chapple & Spang 1974, Johnson & Johnson 2000, Ramsay & Huber 1987).

The dipping fault and bed slip surfaces change shape and orientation due to deformation. Linear elastic fracture mechanics predicts that slip along a mode II crack is associated with a small degree of rotation (e.g. Lawn). Within my model, this rotation is about the strike of the fault and serves to steepen the fault. In Model 1, the initially 35° dipping fault steepens to an average dip of 40°. In Model 2, bed slip surfaces are folded into an anticline along with the nearby reference horizons. The dipping fault in Model 2 steepens to an average dip of 53° and shows non-planar surface topology that is probably a result of interactions with the overlying bed slip surfaces. Flexural slip along dipping fold limbs produces an overall downward movement of material out of the anticline core, which lies directly above the upper fault tip. This out-of-core displacement distorts the dipping fault.

2.3.2 Displacement Vectors

In map view, displacement vectors are strikingly different between models with and without flexural slip. Model 1 without slipping bedding planes has displacement vectors forming a half-radial pattern in the hanging wall (Figs. 2.5A & 2.5C). The distribution of horizontal displacement differs with depth in Model 1; at shallow depths, horizontal displacements reach a maximum above the upper fault tip (Fig. 2.5A), whereas at greater depths, the largest horizontal displacements are in the hanging wall above the lower fault tip (Fig. 2.5C). Model 2 has a more symmetrical pattern of horizontal displacement than Model 1, with areas of large horizontal displacement to the east and west of the anticline, and relatively little horizontal displacement on the crest (Figs. 2.5B & 2.5D). Although vectors at the crest of the anticline in Model 2 appear relatively small in Fig. 2.5, they have a large vertical component and are some of the largest displacements in the anticline. Horizontal displacement vector magnitudes are largest at the shallow reference depth in the model with flexural slip (Fig. 2.5B), but the general pattern of horizontal displacement does not change significantly between 0.5 and 1.5 km (Figs. 2.5B & 2.5D).

The fold-strike parallel, or out-of-plane component of transport is evident from the obliquity of horizontal displacement vectors from the contraction direction. Displacement vectors are approximately parallel to the contraction direction at the apex of the anticline (north position 0 km) and approximately perpendicular to the contraction direction near the lateral fault tips (north positions 4 and -4 km). In general, the component of out-of-plane transport is negligible near the apex of the anticline, and

increases outward along strike. This trend is observed in both models, and at both reference horizon depths (Fig. 2.5).

The degree of out-of-plane transport varies with depth in both models. In general, the magnitude of out-of-plane displacement increases with vertical distance from the fault (Fig. 2.6A). The vertical displacement field in Model 1 is relatively continuous, with a smooth transition between sub-vertical displacements near the fault, and oblique displacements near the free surface of the model above the lateral fault tip (Fig. 2.6A). The same trend of decreasing out-of-plane transport with depth is also present in Model 2, although bed slip surfaces affect the spatial pattern of out-of-plane displacement (Fig. 2.6B). Below the lower bed slip surface, Model 2 resembles the displacement field of Model 1, with a smooth transition between sub-vertical vectors near the fault and oblique vectors near the lower bed slip surface (Fig. 2.6B). Above the lower bed slip surface are two discrete mechanical units bounded by upper and lower bed slip surfaces and the free surface of the model (Fig. 2.6). Within the lower unit, displacement vectors are vertical and parallel to the remote contraction direction near the center of the mechanical unit and oblique near the bed slip surfaces, forming a symmetrical pattern about the neutral surface of this unit. The upper mechanical unit has an asymmetric pattern with a relatively smooth transition from sub-vertical displacement vectors near the bed slip surface, to highly oblique vectors near the free surface of the model (Fig. 2.6).

Because out-of-plane displacement varies with depth in Model 2, the location of reference horizons biases the degree of out-of-plane displacement interpreted from the reported results. For example, the lower reference horizon lies at the center of the

lower mechanical unit, which is a neutral surface where out-of-plane displacements are minimal (Fig. 2.6B). Therefore, the map view of the displacement field in Figure 2.5D represents the minimum out-of-plane transport in that mechanical unit; reference horizons located near the bed slip surfaces would show significantly greater out-of-plane transport. Similarly, the upper reference horizon lies at the center of the upper mechanical unit, which displays intermediate degrees of out-of-plane transport for that mechanical unit; more out-of-plane transport occurs above the reference horizon, whereas less out-of-plane transport occurs below the reference horizon (Fig. 2.6B).

2.3.3 Percentage of Out-of-Plane Displacement

The percentage of out-of-plane displacement can be calculated by dividing the out-of-plane component of motion by the total displacement (Fig. 2.7). This provides a quantitative measure of the percentage of out-of-plane displacement in order to highlight structural positions where out-of-plane transport may be more or less prevalent in plunging anticlines. This calculation represents the percent error that might be incurred when incorrectly assuming plane strain in a pseudo three-dimensional forward model or restoration of a non-cylindrical fold.

In the absence of flexural slip, a significant percentage of out-of-plane displacement occurs near the plunging termination of the anticline. Along the upper reference horizon of Model 1, up to 90% of the displacement is out-of-plane in this location (Fig. 2.8A). Along the lower reference horizon in Model 1, up to 70% of the displacement is out-of-plane near the plunging termination of the anticline (Fig. 2.8C).

In general, the greatest percentage of out-of-plane displacement tends to occur near the lateral fold terminations and near the free surface of the model (Fig. 2.6A).

Model 2 has a significantly different distribution of out-of-plane transport than Model 1 (Fig. 2.8B & D). The maximum percentages of out-of-plane transport at the most distal tips of the folds are the same for both models, but larger portions of the anticline in model 2 have lesser percentage of out-of-plane transport than model 1. The flexural slip within model 2 complicates the pattern of out-of-plane transport. Because the lower reference horizon of model 2 samples the neutral surface of the lower mechanical unit, this horizon shows negligible out-of-plane transport along much of the fold (Fig. 2.6B). In cross section, out-of-plane displacements within the lower mechanical unit are as much as 40% near the bed slip surfaces and 0% along the neutral surface at the same structural position (Fig. 2.6B). Thus, the neutral surface sampled in Figure 2.5D provides a minimum estimate of out-of-plane transport.

2.3.4 Normalized Ratio of Out-of-Plane Transport

While useful for comparing the amount of out-of-plane displacement at specific points along the fold, the percentage of out-of-plane transport does not take into account variations in the displacement magnitudes at different structural positions. For example, Figure 2.5 shows that percentages of out-of-plane transport are largest near the lateral fold tips, however, displacement magnitudes in this structural position are insignificant compared to displacements near the center of the anticline. To highlight areas where the magnitudes of out-of-plane displacement are significant, I normalize the out-of-plane component of displacement by the average displacement magnitude for

all points in each reference horizon. For example, the average displacement magnitude for the upper reference horizon in Model 1 is 77.4 meters, so the out-of-plane component of each displacement vector in the upper reference horizon in Model 1 is divided by 77.4. This calculation downplays the insignificantly small displacement vectors, and highlights areas where out-of-plane displacement is close, equal to, or greater than the average displacement for a given reference horizon (values near 1 on Fig. 2.9).

When normalized by the average displacement, the most significant magnitudes of out-of-plane transport are located near the anticlinal axis between the apex (north position 0) and the lateral fold tips for both models (north positions -4 km and 4 km, Fig. 2.9 & 2.10). The position of highest normalized out-of-plane transport is the same along all reference horizons and occurs above the lateral fault tips. The reference horizon at 500 meters depth in Model 1 has the largest ratios, with out-of-plane transport nearly equaling the average displacement along parts of the fold axis (Fig. 2.9A). The deeper reference horizon in Model 1 has less out-of-plane displacement, with ratios up to 0.6 (Fig. 2.9C).

Flexural slip within Model 2 significantly reduces out-of-plane transport at the reference horizons. The upper reference horizon in Model 1 has relatively large out-of-plane displacement, with normalized out-of-plane displacement up to 0.5 along the fold axis. In contrast, out-of-plane displacement appears to be relatively insignificant in the deeper bed in Model 2, with ratios of 0.1. However, this reference horizon may not be sampling a representative out-of-plane displacement for the lower mechanical unit.

In cross section, both models show increasing out-of-plane displacement with distance above the fault tip, although this pattern is complicated by the effects of flexural slip in Model 2 (Fig. 2.10). Near the fault, displacements are constrained to follow the slip direction along the fault while far away, the displacements reflect the uplift and arching of the folded material. Flexural slip within model 2 augments out-of-plane displacement at the tops of mechanical units and reduced these displacements at the bases. This asymmetry arises from fold-associated tilting of both the mechanical unit and the displacement field within that unit (Fig. 2.10B). In the absence of any tilt of flexural-slipping layers, the lower half of the mechanical unit moves upwards and toward the apex of the anticline, the center moves directly up, and the upper half moves upwards and away from the apex (Fig. 2.6B). The tilting of this displacement pattern away from the apex of the fold during folding rotates the displacements in the top and center of the mechanical unit away from vertical and rotates the displacements in the lower half closer to vertical (inset Fig. 2.10B). Consequently, out-of-plane displacements are greater at the top than at the base of individual mechanical units.

2.4 Effect of friction coefficient and spacing of bed slip surfaces on fold shape

The models presented thus far represent two scenarios: a condition of no flexural slip or all bonded layer contacts (Model 1) and a condition of frictionless slip on two bed slip surfaces (Model 2). The conditions of bonded and freely-slipping beds represent end-members of the expected conditions along natural layer contacts. Natural bedding surfaces will have some cohesion and frictional resistance to slip due to asperities that would yield flexural behavior between that of bonded layers or freely

slipping layer contacts. Furthermore, natural stratigraphic sequences typical have greater than two contacts to accommodate flexural slip. To assess the effects of friction coefficient on and spacing of sliding bed surfaces, I investigate two-dimensional models through the center of the three-dimensional fold, where I have showed out-of-plane transport to be negligible (Figs. 2.8 & 2.9).

The two-dimensional formulation allows us to use an existing BEM code, FRIC2D, that incorporates frictional slip and reduces computational demands so that I may explore the effects of more than two sliding contacts. Along frictional faults within FRIC2D, the material properties of the faults are prescribed (e.g. cohesion and friction coefficient) rather than the displacements and/or tractions as with other BEM elements (Cooke 1997, Crouch 1979, Crouch & Starfield 1990). FRIC2D has been used to examine the influence of bedding-plane slip within folds (Cooke et al. 2000, Cooke & Pollard 1997), the influence of bedding-plane slip on fracture propagation (Cooke & Underwood 2001), compaction of sediment over buried craters (Buczowski & Cooke 2004), and the interaction of faults within the Los Angeles metropolitan region (Cooke & Kameda 2002).

The two-dimensional models investigate 4 cases of layer contacts overlying a fault: 1) bonded layer contacts, 2) two evenly spaced frictionally slipping layer contacts, 3) two evenly spaced freely slipping layer contacts, and 4) frictional slip along 5 contacts (Fig. 2.11: inset). The initial geometry of faults and bedding surfaces within the two-dimensional model is chosen as step 25 (of 50) from the three-dimensional incremental model. This ensures that the results are applicable to most stages of folding when beds are not horizontal. The right hand side of the model is translated to the left

275 m to provide about 1% contraction. Lithostatic gravitational stresses are superposed onto the model to give realistic resistance to slip; I use sediment density of 2700 kg/m^3 . Because frictional slip is inelastic and subsequently path-dependent, I apply the contraction monotonically within four steps. The dipping fault is free to slip while bed contacts have a moderate friction coefficient of 0.65 and 3.25 Ma cohesion (Cooke & Underwood 2001).

Comparison of uplift patterns in the two-dimensional frictional and free slip models provides a qualitative calibration of the three-dimensional free slip model results to more realistic frictional behavior of layered sequences. The bonded and two freely slipping layer contact conditions correspond to conditions in the three-dimensional Models 1 and 2 respectively. The uplift patterns of these two conditions plot as distinct extremes, with the bonded layers producing a broad uplift pattern, and the two freely slipping layer contacts producing a localized uplift. The 2D model with two frictional slip contacts produces fold shape intermediate to the bonded and two freely slipping contact models, suggesting that frictional resistance between contacts significantly affects fold shape, and therefore displacement vectors in the model. With the addition of additional frictional contacts, the fold tightens and more closely resembles the model with two freely slipping contacts. This suggests that Model 2 with limited freely slipping contacts can approximate a case of many frictional contacts.

2.5 Discussion

The results of this study suggest that out-of-plane transport can be significant in plunging fault-cored folds. Large components of out-of-plane transport arise in models

with no bed slip above the fault, suggesting that out-of-plane transport is most significant in relatively massive rocks that resist flexural slip. Thick sequences of massive carbonates, intrusive igneous rocks, and basement uplifts may provide such conditions. However, because fault-cored folds often form in layered stratigraphy where bed slip is an important aspect of the folding process, Model 2 may be a more representative model of folding conditions.

The three-dimensional models presented here highlight structural domains where out-of-plane displacement is significant and where plane strain can be assumed. For example, out-of-plane displacement is localized above the lateral fault tips and plane strain assumptions should be avoided at this structural position (Figs. 2.9 and 2.10). Although flexural slip reduces the overall errors incurred by assuming plane strain near the fault tips (Fig. 2.10), local errors may be quite significant. Within cross-section, bed slip surfaces serve to compartmentalize out-of-plane displacement within distinct mechanical units. Although my model has only two mechanical units I can generalize from these results that out-of-plane displacement within folded sedimentary strata is enhanced at the tops of mechanical units (Figs. 2.6B & 2.10B). Consequently, when utilizing plane strain fold restorations and models, consideration should be given to the errors that arise in these regions.

Three-dimensional restorations are commonly designed to predict the location and orientation of secondary structures such as faults and joints that may serve as subsurface flow conduits for hydrocarbons, groundwater contaminants, and other subsurface fluids (e.g. Hennings et al. 2000). Fracture orientations in these cases are usually inferred from maximum or minimum curvature direction, or from inference of

strains from shear between transport planes (Fischer & Wilkerson 2000, Hennings et al. 2000). A fracture prediction using fully three-dimensional models may locally differ significantly from a pseudo-three dimensional one because the out-of-plane component of displacement near flexural slip surfaces and the free surface of the model may strongly affect the orientation of strain axes that are used to predict fault and fracture orientations.

The new incremental models of this study show some new results that may have implications for the development of fault systems. During progressive folding, the underlying thrust fault is expected to both steepen and distort, due to slip along the fault overlying bedding planes (see Supplemental Model2.pdf). During later stages in folding I might expect that the thrust fault that was ideally configured to accommodate horizontal contraction later to have inefficiently steep dips and rough topology. At some point inefficient thrust faults may become inactive in favor of the development of new more shallowly dipping and more planar faults. Although the ceasing of fault slip due to progressively unfavorable dips has been described (e.g. Jackson and McKenzie, 1983; Sibson, 2001), to my knowledge the influence of progressive surface roughness has not yet been examined.

The results presented in this paper focus on the overall displacement trajectories during the entire evolution of a fault-cored fold. Future studies will examine the temporal development of displacement trajectories and stresses in the incremental model. For example, slip along bed surfaces in the initial stages of folding are only due to slip on the underlying fault because bed slip surfaces are oriented parallel to the contraction direction (Cooke & Pollard 1997, Nino et al. 1998). As folding progresses,

bed slip surfaces rotate toward angles more favorable to slip, thus contributing to fold amplification (Chapple & Spang 1974, Johnson & Johnson 2000, Ramsay & Huber 1987). The initial displacement and stress field is dramatically different than stresses in the later stages of folding due to fold tightening and amplification by flexural slip. The changing stress state during fold evolution has important implications for structural restoration and joint and fracture prediction.

2.6 Conclusions

Displacement trajectories in three-dimensional BEM models show that out-of-plane transport accounts for a significant component of the total displacement in fault related folds. These results have significant implications for restoration and modeling of plunging folds. The most significant out-of-plane transport occurs where there are no slipping bed surfaces and above the lateral fault terminations. Therefore, plane should not be assumed in massive strata that resists slip and across the lateral terminations of folds. Furthermore, out-of-plane transport increases with distance above the fault, so the most significant errors may arise near the earth's surface in plane strain models.

Fault-cored folds are commonly found in layered sedimentary strata where flexural slip is common (Epard & Groshong 1995, Erslev 1991, Suppe 1983, Suppe & Medwedeff 1990). Where bedding plane slip occurs in non-cylindrical folds, out-of-plane displacement is heterogeneously distributed because individual slip surfaces compartmentalize out-of-plane transport within each mechanical stratigraphic unit. Mechanical units bounded by bed slip surfaces generally have little out-of-plane

transport in the middle of the mechanical unit, but large out-of-plane displacements near the upper portions of the mechanical unit.

My results have implications for current and future forward models and restorations of fault related folds. I have highlighted structural domains on non-cylindrical folds where the plane strain assumption of zero out-of-plane displacement will produce errors. My results also suggest that inferring stress or strain from the plane strain models may be problematic for plunging fault-cored anticlines, as plane strain models may not account for the heterogeneity of out-of-plane stresses that would likely occur on the scale of each mechanical unit.

2.7 Figures

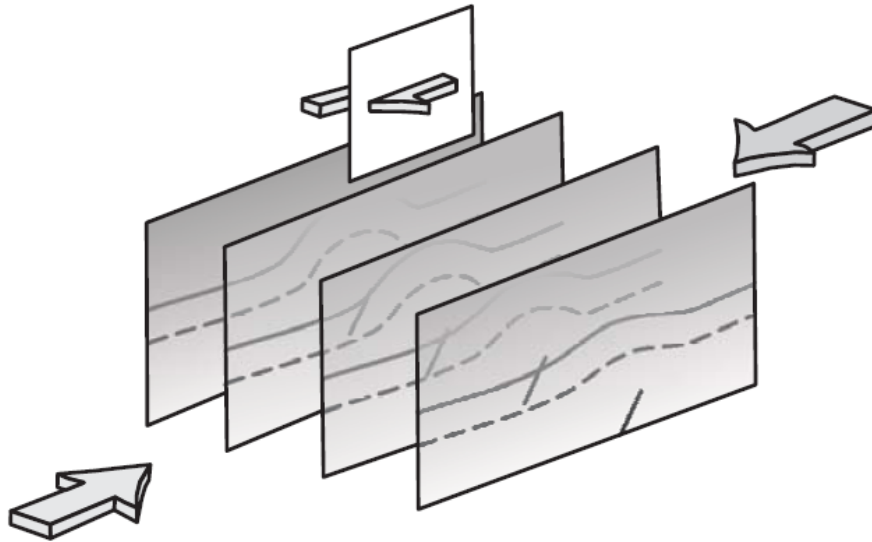


Figure 2.1 Cartoon of a pseudo three-dimensional representation of a three-dimensional structure. Restoration or forward models using 2D-3D methods would only resolve displacement and shear in the plane of section. Shear between the individual planes is neglected.

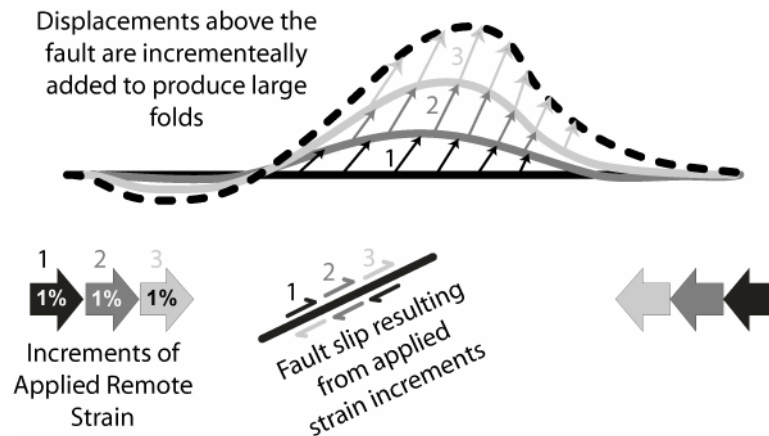


Figure 2.2 Incrementing infinitesimal elastic strains to produce finite deformation observed in natural folds. Each increment of 1% strain induces slip on the fault and deformation of the suprajacent beds. These newly displaced beds form the input for the following increment in the model, such that infinitesimal strains are summed to produce finite deformation. Although not sketched here for simplicity, the fault surface also deforms with incremental strain.

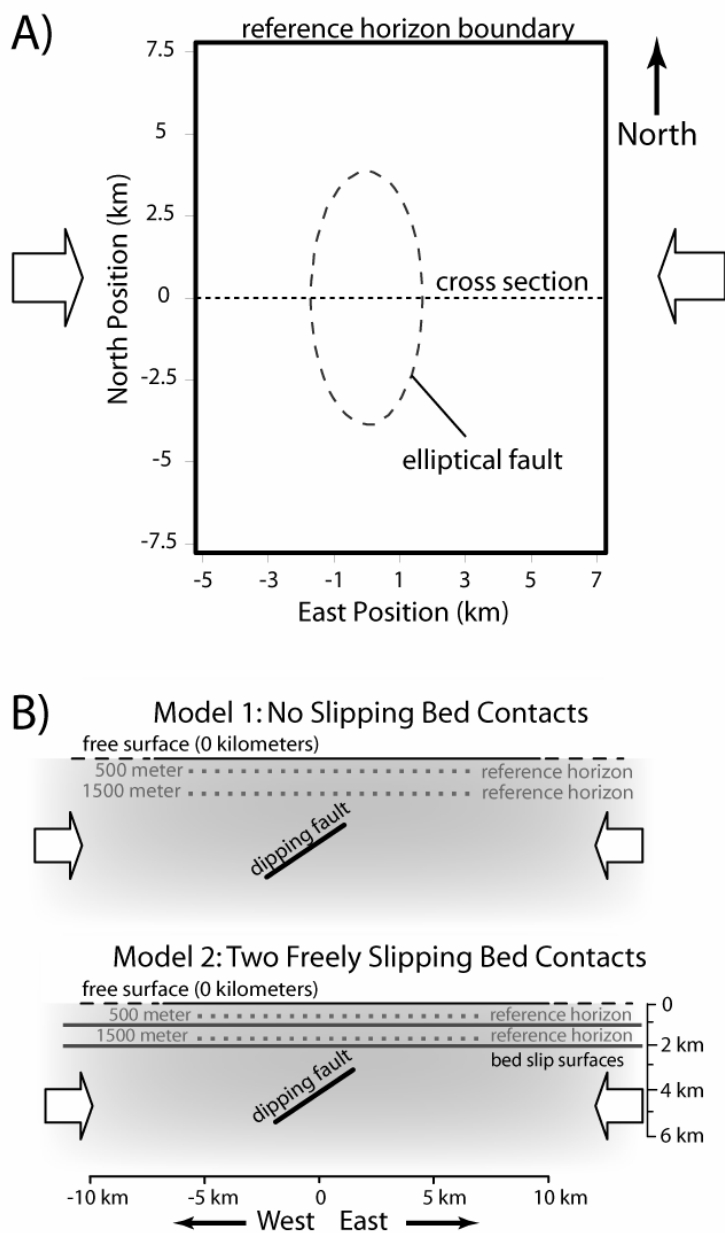


Figure 2.3 Initial setup of the two models. A) Map view of fault and horizontal extent of the reference horizon. The elliptical fault (dashed ellipse) strikes north-south, has a westerly dip of 35° , is 8 km long in the north-south direction, 4 km long in the east-west direction, and is centered at 4 km depth. The dotted line corresponds to the cross sections in part B. B) Cross sectional views of the two initial model boundary conditions. Reference horizons (dotted lines) placed at 5 and 1.5 kilometers depth are used to track folding deformation. In Model 2, bed slip surfaces (thin solid lines) extend laterally until the required condition of no slip at the lateral tips does not affect folding in the model.

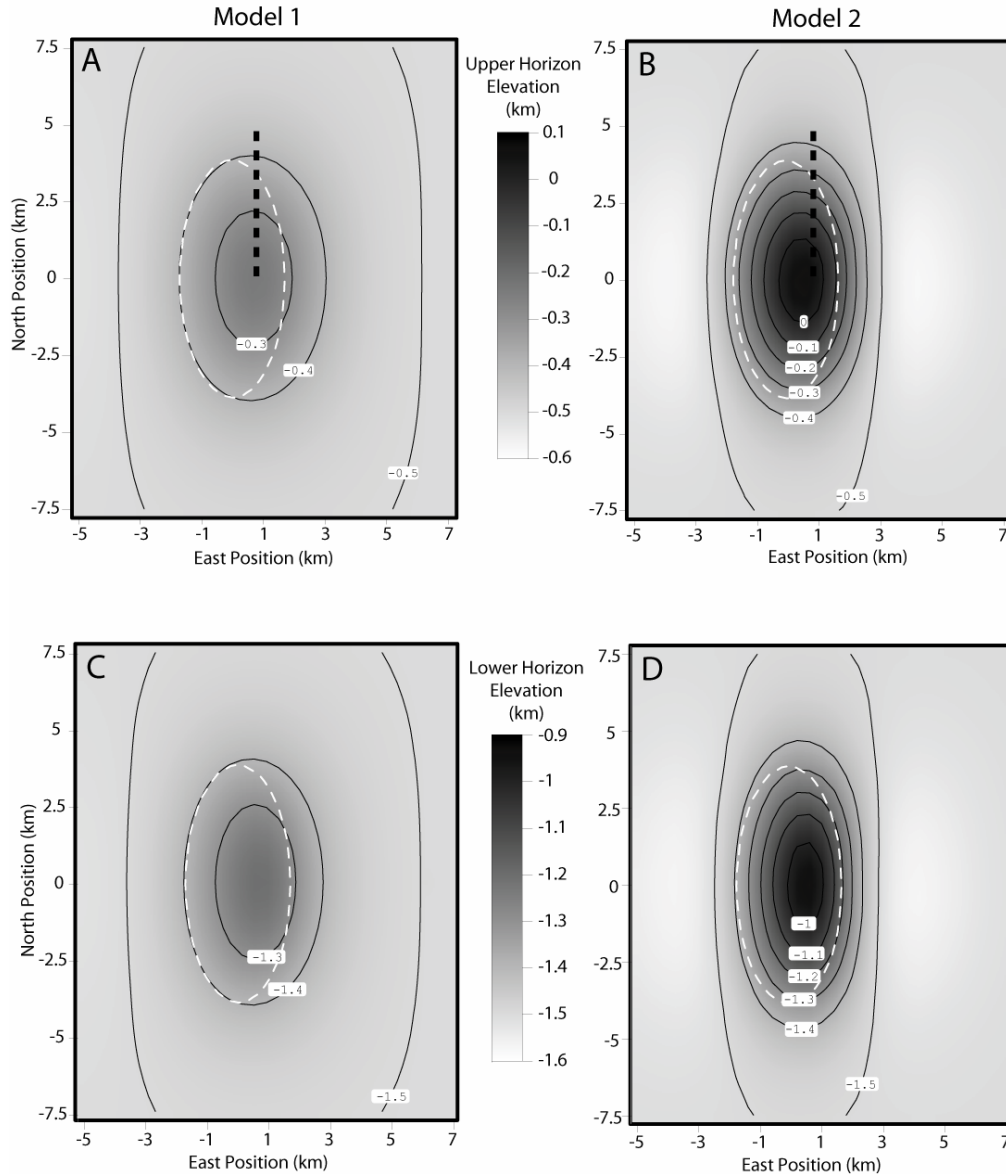


Figure 2.4 Fold shape of two reference horizons within Models 1 and 2. Dashed ellipse shows the projection of the fault. Grayscale map is the same for each reference horizon (e.g. A & B have the same scale, and C & D have the same scale). Note the increasing fold amplitude and decreasing fold width (strike perpendicular) in Model 2 with bedding plane slip. The straight dotted lines show the locations of cross sections in Figure 2.5. In Model 1 the width (east direction) to strike length (north direction) of the fold is 0.125, whereas the width to strike length of the fold is 0.03 in Model 2.

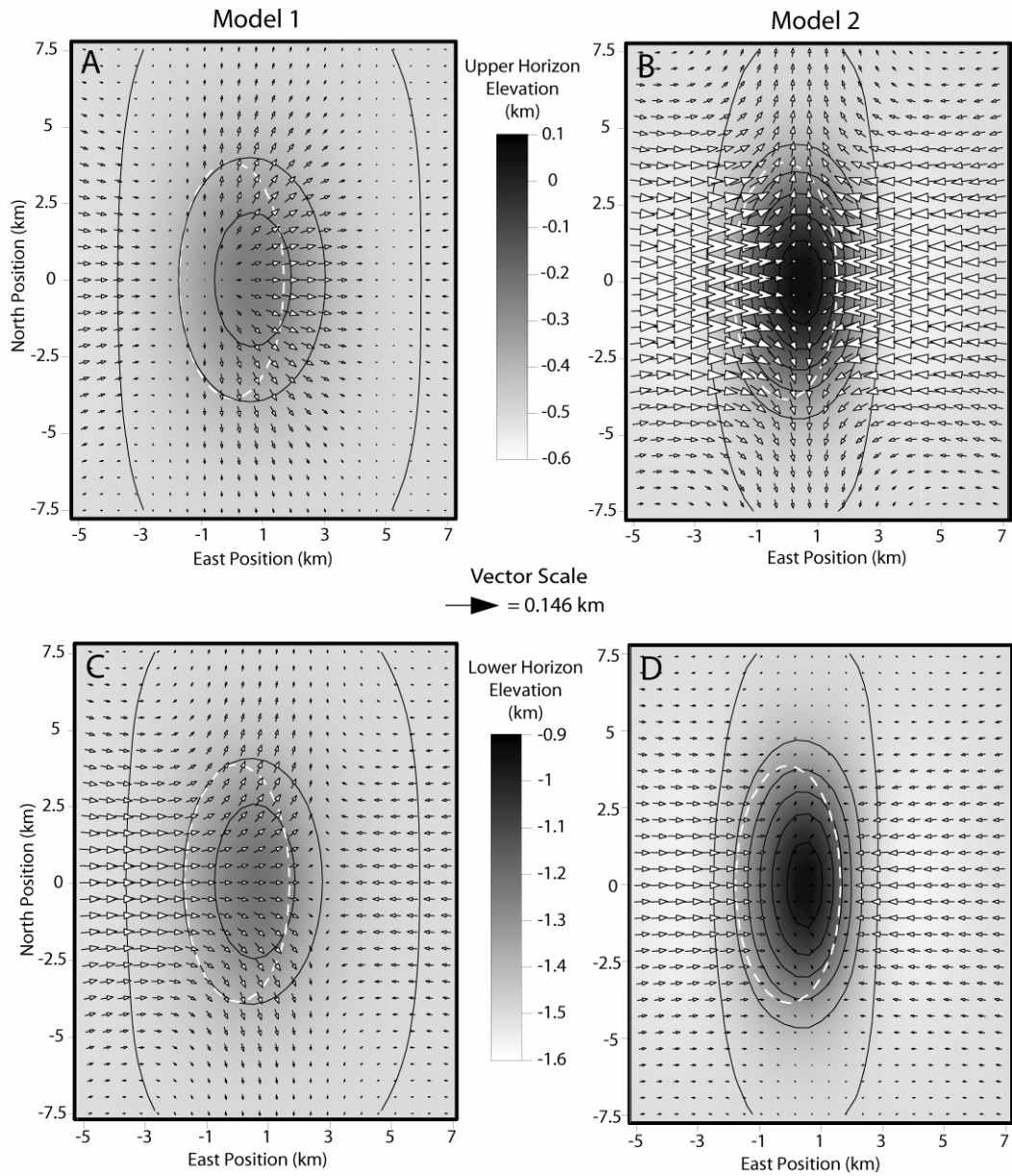


Figure 2.5 Map view of horizontal component of displacement vectors for the two reference horizons superposed onto contour map of fold shape. A) Model 1, upper reference horizon, B) Model 2, upper reference horizon, C) Model 1, lower reference horizon, D) Model 2, lower reference horizon. Grayscale map shows fold elevation at the surface. Points generally move away from the apex of the anticline and show considerable out-of-plane movement near the lateral fold tips.

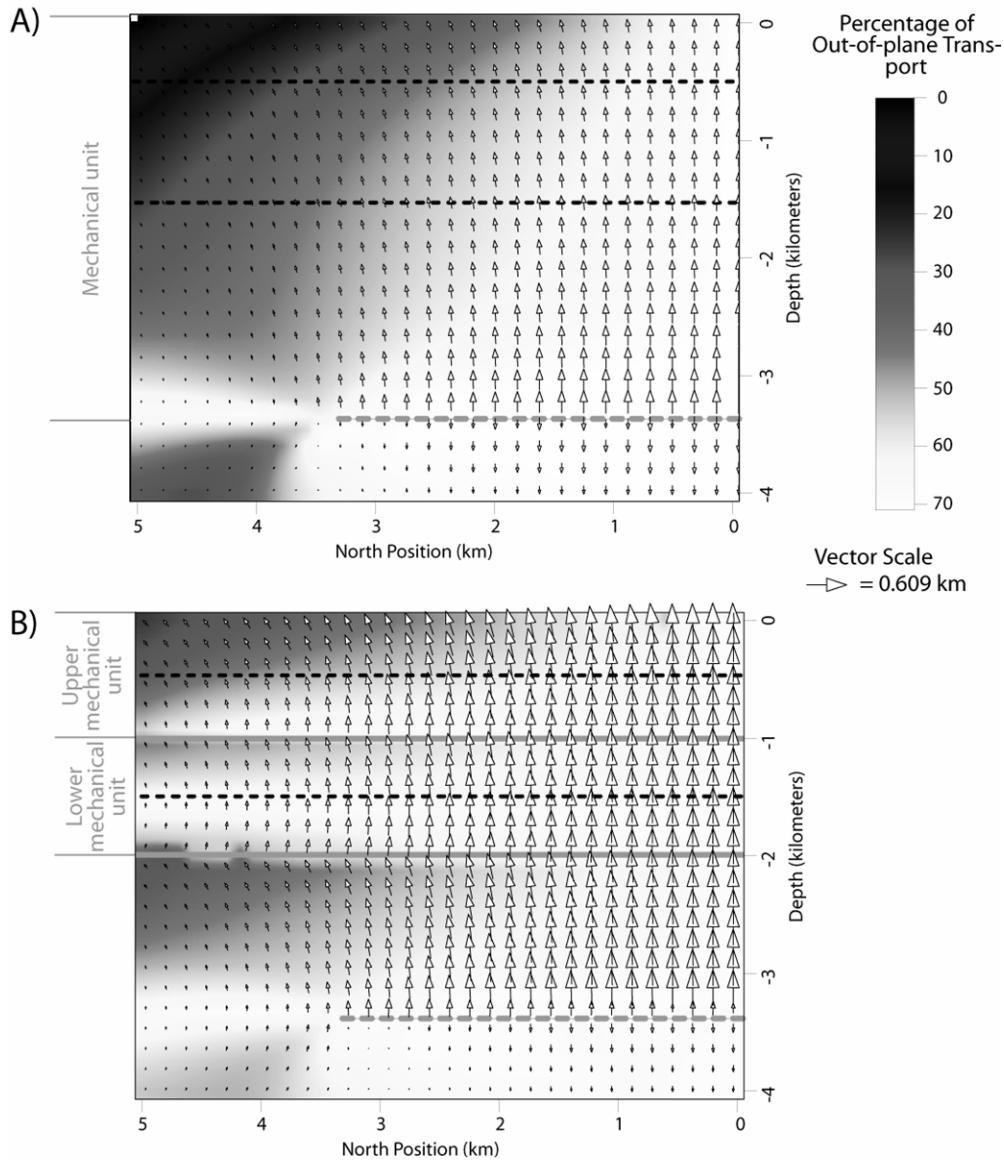


Figure 2.6 North-south cross sections perpendicular to the contraction direction and parallel to fault strike show displacement vectors superposed on density plots of percentage of out-of-plan transport. A) Model 1 results with no flexural slip. B) Model 2 results with two freely slipping bed slip surfaces. Location of the cross sections is shown in figure 2.4. This figure shows the initial geometry of the fault (dashed gray lines), bed slip surfaces (solid gray lines), and reference horizons (dashed black lines); final positions of these surfaces can be inferred from the displacement pattern. The degree of out-of-plane transport decreases with depth and increases with proximity to the lateral fault tip. In Model 2, out-of-plane displacement is localized near bed slip surfaces and/or the free surface of the model. The lower reference horizon in Model 2 is located at a neutral surface, where out-of-plane displacement is at a minimum. Within Model 2, vectors change direction above and below bed slip surfaces.

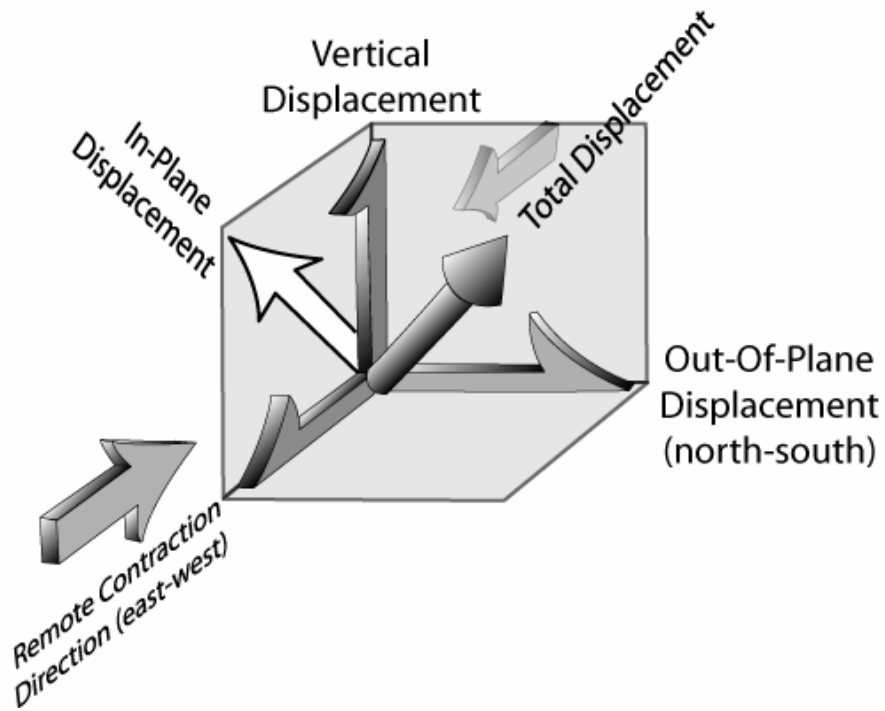


Figure 2.7 Schematic diagram of vector components. The white arrow indicates the in-plane displacement vector that is the sum of the vertical and contraction parallel (east-west) vector components. The arrow pointing to the right indicates the out-of-plane displacement vector, which is the north-south component of displacement parallel to the fold axis.

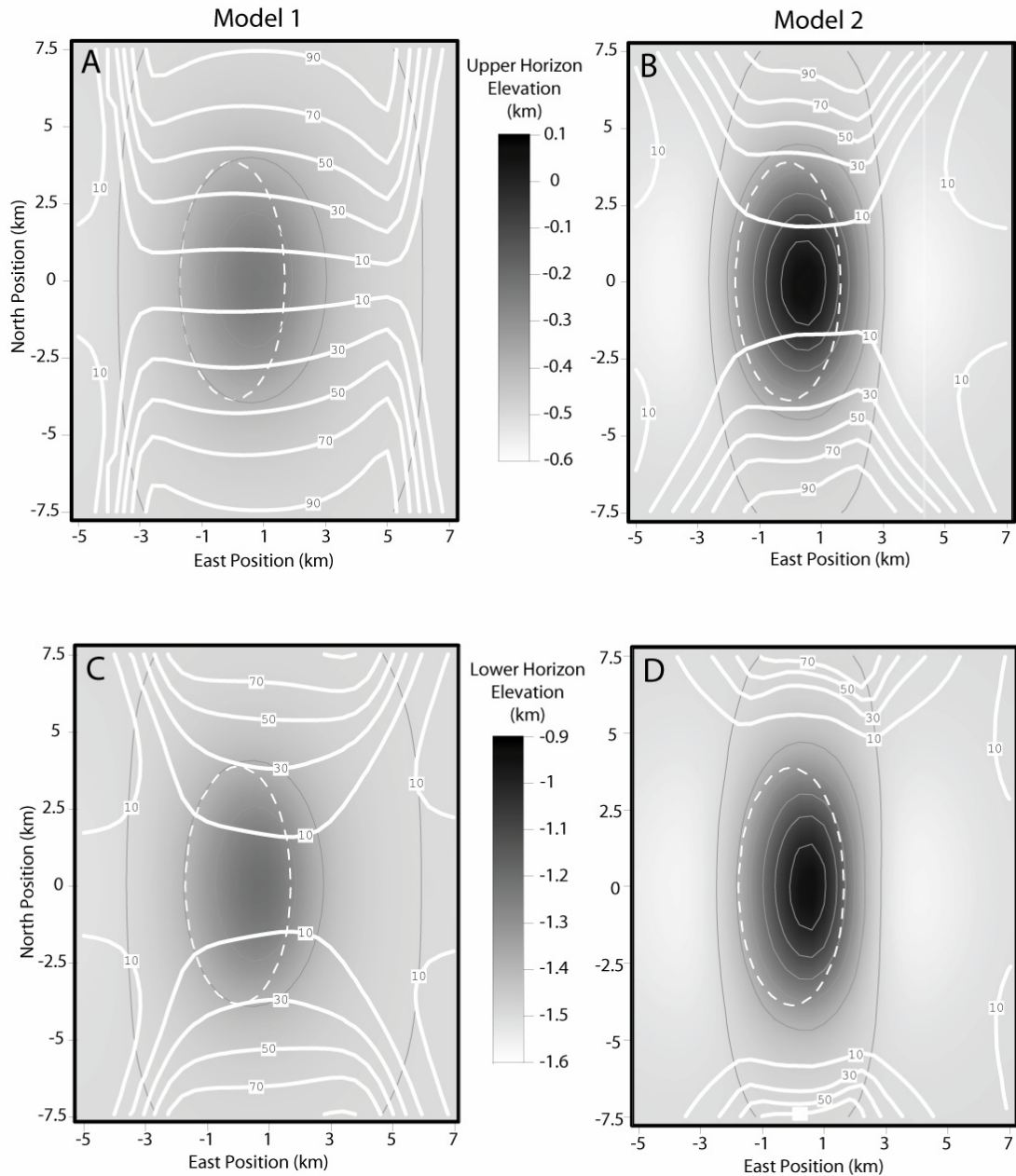


Figure 2.8 Map view of the percentage of out-of-plane displacement for each point on the reference horizons (thick white contours) overlain on a map of fold shape (shaded with grey contours). A) Model 1, upper reference horizon, B) Model 2, upper reference horizon, C) Model 1, lower reference horizon, D) Model 2, lower reference horizon. Dashed white ellipse shows the outline of the fault. The largest percentage of out-of-plane transport in all models occurs along plunging terminations of the anticline.

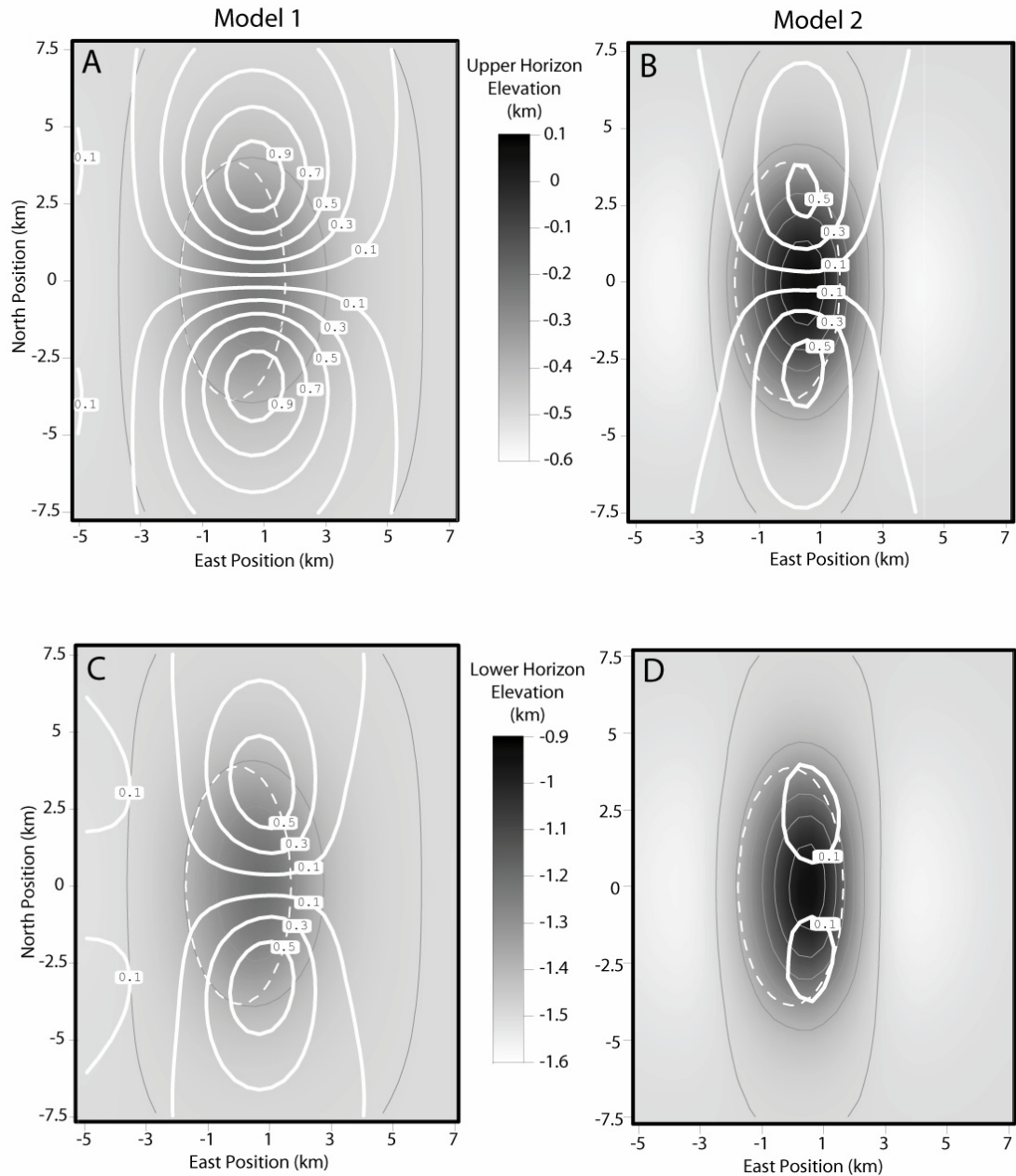


Figure 2.9 Ratio of out-of-plane displacement to the average vector magnitude for each horizon (thick white contours) superposed on shaded and contoured (thin lines) map of fold shape. A) Model 1, upper reference horizon, B) Model 2, upper reference horizon, C) Model 1, lower reference horizon, D) Model 2, lower reference horizon. Values near 1 represent locations where the out-of-plane component of transport is roughly equal to the average displacement magnitude for that horizon. Greatest normalized out-of-plane displacement occurs near the fold axis between the apex and the plunging terminations of the fold.

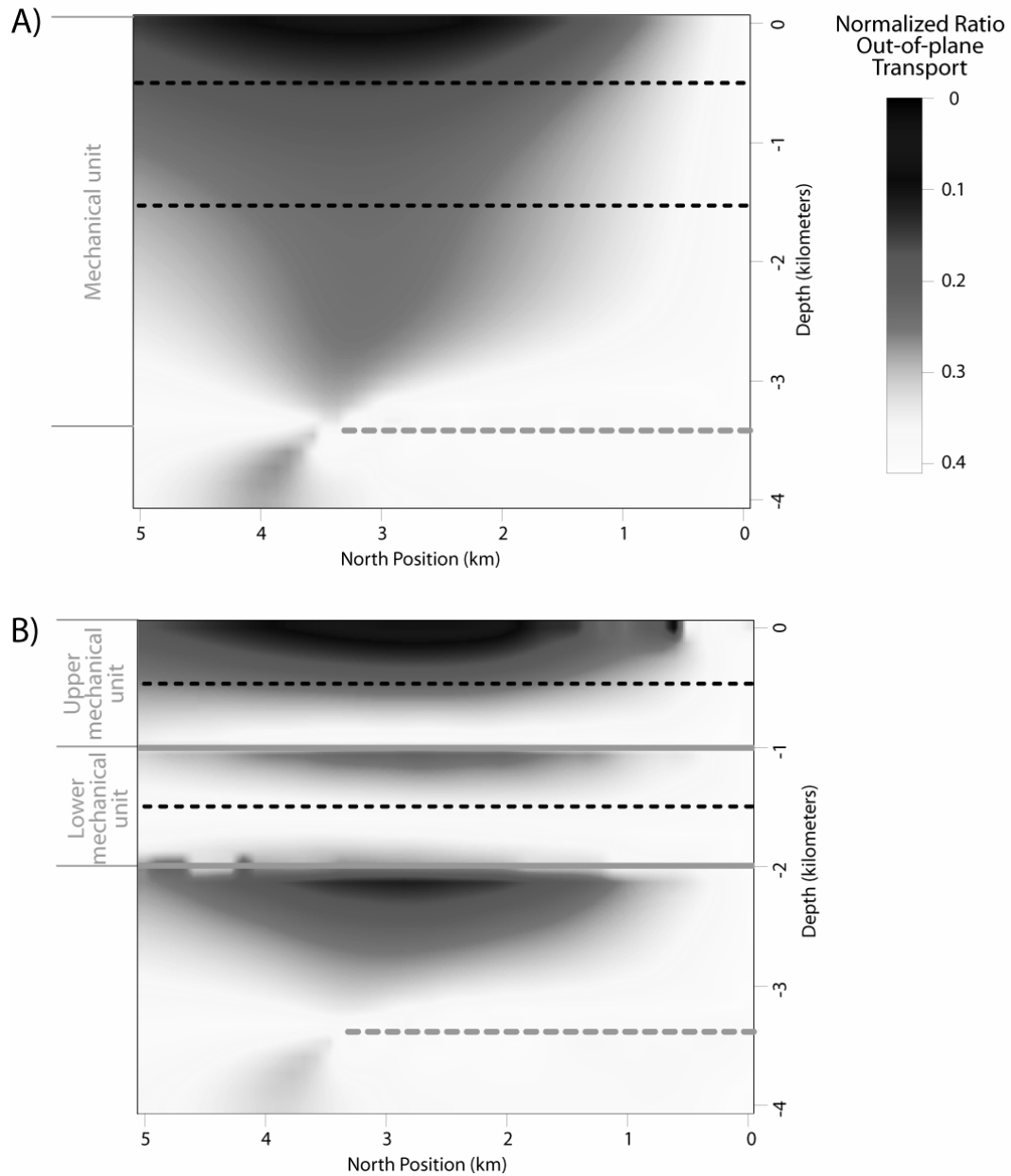


Figure 2.10 North-south cross-section showing the ratio of out-of-plane displacement to the average displacement magnitude within the vertical section.
 A) Model 1 with no flexural slip. B) Model 2 with two freely slipping bed slip surfaces. Section location is shown in figure 2.4. This figure shows the initial geometry of the fault (dashed gray lines), bed slip surfaces (solid gray lines), and reference horizons (dotted black lines). Significant out-of-plane displacements arise above the lateral fault tip in both models. Generally out-of-plane displacement increases with distance above the fault. Flexural slip in Model 2 adds complexity to this pattern by reduced out-of-plane displacement near the base of each mechanical unit and augmenting out-of-plane slip near the top of the unit.

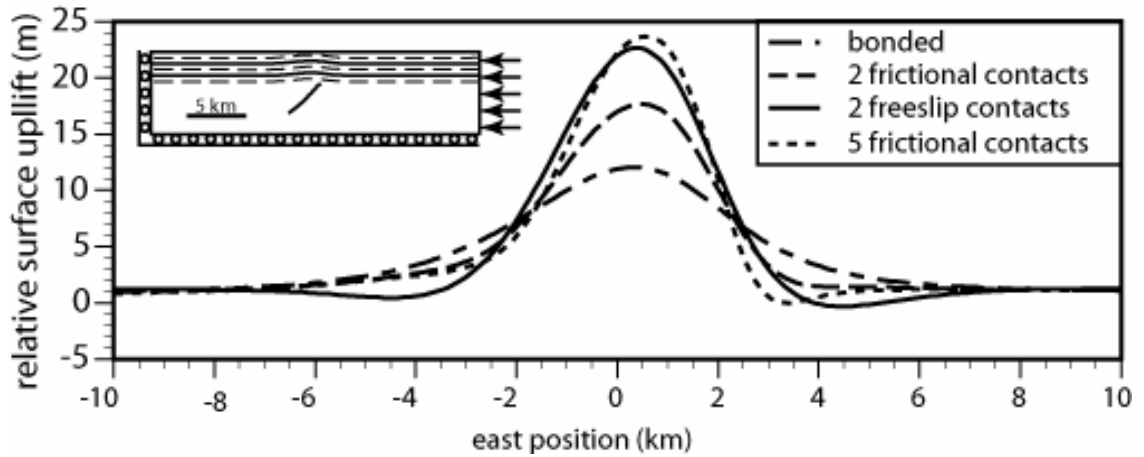


Figure 2.11 Surface uplifts for four different frictional bed slip boundary conditions in FRIC2D. Inset figure shows the model boundary conditions, which are derived from the 25th increment in the three-dimensional Model 2. A model with two freely slipping contacts may approximate the condition of five or more frictional contacts.

CHAPTER 3

**TEMPORAL CONSTRAINTS ON FRACTURING ASSOCIATED WITH
FAULT RELATED FOLDING AT SANT CORNELI ANTICLINE, SPANISH
PYRENEES**

3.1 Introduction

The ability to quantitatively predict the orientation and density of natural fractures is advantageous in many industries because subsurface fracture networks form fluid flow pathways in groundwater aquifers, hydrocarbon reservoirs, and hydrothermally active basins. Fracture prediction in layered sedimentary rocks relies heavily on layer shape (fold shape) and fault shape. Fold shape affects fracturing because bending stresses control the density and orientation of fractures in three-dimensions (e.g. Fischer & Wilkerson 2000, Szilard 1974). Faults exert a significant control on both the overall fold shape and the stress field near fault tips (e.g. Bellahsen et al. 2006, McGrath & Davison 1995, Pavlis & Bruhn 1988, Rudnicki & Wu 1995, Savage & Cooke 2004). Field studies of fracturing in fault related folds serve two roles in fracture prediction. First, natural structures can be used to test theoretical predictions for fracturing based on plate bending, faulting, or other models for fracture formation (e.g. Bellahsen et al. 2006, Bergbauer & Pollard 2004, Hennings et al. 2000). Second, field studies can inform subsurface predictions fracture networks, which are commonly below the resolution of many geophysical techniques.

Interpretation of fracturing associated with fault related folding is complicated by the fact that geologic timescales prohibit direct observation of the temporal changes

in an evolving structure; in most cases geologists can only observe the present day patterns of layers, faults, and fractures. Geologists have devised a variety of techniques to infer intermediate stages in the formation of fault related folds. Some examples of such techniques are forward geometric and geomechanical fold modeling (e.g. Erslev 1991, Johnson & Johnson 2002, Poblet & McClay 1996, Suppe 1983, Suppe & Medwedeff 1990), structural restoration algorithms (e.g. Griffiths et al. 2002, Maerten & Maerten 2006, Rouby et al. 2000, Thibert et al. 2005), and studies of natural folds and numerically modeled folds with syn-tectonic strata (Ford et al. 1997, Novoa et al. 2000, Poblet et al. 1998, Salvini & Storti 2002, Vergés et al. 1996). Natural folds with syn-tectonic strata provide the most direct evidence of changes in fold shape because each syn-tectonic horizon can be individually restored to document a different transitional fold shape, thus constraining crucial aspects of folding that affect fold related fracturing (e.g. Bernal & Hardy 2002, Ford et al. 1997, Novoa et al. 2000, Poblet et al. 1998, Salvini & Storti 2002, Vergés et al. 1996). While syn-tectonic strata have been used extensively to understand fold evolution, relatively few studies have utilized syn-tectonic strata to understand the evolution of fracturing and small scale structures associated with folding (e.g. Nigro & Renda 2004).

Field studies of fractures associated with fault related folding have suffered from a crucial lack of data linking the changes in fold shape through time to specific fracturing events. Early conceptual models for fold related fracturing (Stearns 1967, Stearns & Friedman 1972) have been criticized because their predictions are based entirely on the final fold shape, neglecting transitional fold shapes, pre-existing fracture patterns, and stresses associated with an underlying fault tip (Bellahsen 2006,

Bergbauer & Pollard 2004, Fischer & Wilkerson 2000, McGrath & Davison 1995, Savage & Cooke 2004). More recent studies have focused on distinguishing fold related fractures from pre- and post-fold fractures, however, fold related fractures are usually grouped into “early folding” or “late folding” episodes with little direct evidence for fracture timing relative to specific folding events (e.g. Bellahsen 2006, Bergbauer & Pollard 2004, Cooper 1992, Engelder 1997, Hanks 1997, Hennings et al. 2000, Shackleton 2003). The disconnect between evidence for fracture evolution and fold evolution largely stems from the fact that cross cutting relationships between fractures only reflect the *relative* timing of fracturing events without the context of fold evolution.

The Sant Corneli anticline is a plunging thrust-related anticline in the Spanish Pyrenees that offers a unique opportunity to document the history of fracturing in the context of a well constrained fold history (Figs. 3.1 & 3.2). The anticline is well exposed in three dimensions and has excellent outcrop exposures that are well suited to field mapping of fractures (Fig. 3.3). Additionally, the geometry of adjacent syn-tectonic strata constrains aspects of the fold evolution such as limb rotation and lateral fold propagation (e.g. Bernal & Hardy 2002, Ford et al. 1997, Guillaume et al. 2008, Maerten & Maerten 2006, Novoa et al. 2000, Vergés et al. 1996). I present the sequence of fracturing at Sant Corneli anticline relative to specific depositional and structural events that occurred during folding, thus directly linking fold evolution to fracturing. I first outline the structural/stratigraphic framework of Sant Corneli anticline as documented by previous research and deduced from my own field mapping.

I then present the results of detailed fracture mapping and interpret the fracture history in the context of the structural/stratigraphic evolution of Sant Corneli Anticline.

3.2 Tectono-stratigraphic evolution of the Sant Corneli anticline

The Sant Corneli anticline, situated in the southern central Pyrenees of Spain (Fig. 3.1), formed during the Late Cretaceous and Eocene-Oligocene periods in response to the collision of Iberia with Europe (Puigdefàbregas & Soquet 1986, Roest 1991). Sant Corneli anticline is an asymmetric, westerly plunging anticline that forms the termination of the Bóixols thrust, a nearly 40 km long, east-west trending, south vergent thrust (Berástegui et al. 1990, Bond & McClay 1995, García-Senz 2002, Puigdefàbregas et al. 1992). The Sant Corneli- Bóixols -Nargó anticlines lie above detachments in Triassic evaporites. These fault-related anticlines are a result of inversion of the lower Cretaceous Organyà extensional basin (Berástegui et al. 1990, Bond & McClay 1995, Déramond et al. 1993, Vergés 1993).

Evidence for the structural history of the Sant Corneli-Bóixols-Nargó anticlines is contained in the sedimentary record of the late Cretaceous-Oligocene strata that overlie the anticline. Thus, I summarize previous research on the stratigraphic history of the area to provide a framework for understanding the timing of structural deformation at Sant Corneli anticline. I then describe the local structure of Sant Corneli anticline as it relates to the stratigraphic history, to the structure of the adjacent Bóixols anticline, and to documented Pyrenean deformation events.

3.3 Stratigraphic history

At the first-order, the Sant Corneli anticline exposes a core of highly fractured and faulted carbonate rocks capped by gray marls, all of which are overlain by a sequence of syn-tectonic marls and sandstones (Figs. 3 & 4, Garrido-Megías & Ríos Aragües 1972). The core of the anticline is primarily composed of Triassic to mid Cretaceous terrestrial and carbonate rocks of the Organyà basin (Simó 1989, 1985b). Only rocks as old as, or younger than the mid Cretaceous carbonates of the Sant Corneli sequence are exposed at the surface in the field area (Fig. 3.5). The Sant Corneli sequence consists of platform carbonates and calc-arenites representing the edge of a basin that deepened to the northwest during the Coniacian-Santonian (late Cretaceous, Puigdefàbregas & Soquet 1986, Simó 1985a, 1989, 1985b). A regional angular unconformity separates the Sant Corneli sequence from the overlying Vallcarga sequence, which in the study area consists primarily of turbiditic marls, limestones, and clays (Ardévol et al. 2000, Nagtegaal 1983). Paleocurrents and dramatic thickening of the Vallcarga sequence to the northwest of the Sant Corneli anticline indicate that the area was paleo-high during Campanian time, although it is unclear whether the Sant Corneli anticline was tectonically active during deposition of the marls (Ardévol et al. 2000, Garrido-Megías & Ríos Aragües 1972, Nagtegaal 1983, Van Hoorn 1970). The upper boundary of the Vallcarga sequence and the overlying Aren group is a regional angular unconformity (Simó 1989, 1985b).

Though the Aren group has been subdivided differently by different authors (Ardévol et al. 2000, Déramond et al. 1993, Garrido-Megías & Ríos Aragües 1972, Nagtegaal 1983, Puigdefàbregas & Soquet 1986, Simó 1989, 1985b, Specht et al.

1991), this paper will use the naming conventions delineated by Deramond and others (1993) and revised by Guillaume and others (2008). The base of the Montesquiú sequence is formed by the Puymanons olistostrome, which is deposited unconformably on the Vallcarga sequence. Olistoliths and growth faulting within the unit are interpreted to be associated with basin margin collapse, possibly resulting from the first phase of folding at Sant Corneli anticline (Fig. 5A, Simó 1985a). The olistostrome is overlain by the Salas Marls, which represent the deeper basinal rocks of a northwestward prograding sequence of nearshore to offshore siliciclastic rocks (Fig. 5B, Déramond et al. 1993, Nagtegaal 1983, Simó 1989, 1985b). The Montesquiú sequence is cut deeply at Sant Corneli by a karst surface with locally incised valleys indicating subaerial erosion and sedimentary transport toward the northwest (Fig. 5B, Ardévol et al. 2000, Nagtegaal 1983, Simó 1989, 1985b). The overlying Orcau-Vell sequence consists of fluvial channel fill to the east and tide influenced bioclastic bars to the west, which form the base of a lowstand systems tract (Déramond et al. 1993, Guillaume et al. 2008). This unit thickens abruptly westward near Orcau, corresponding to a rapid deepening of the basin to the west (Ardévol et al. 2000, Nagtegaal 1983). The Boixols thrust may have breached the surface and been fossilized by Aren group rocks as early as Orcau-Vell time. Deramond and others (1993) and Guillaume and others (2008) interpreted that the Orcau-Vell sequence consists of a lowstand systems tract, followed by a transgressive systems tract, which is overlain by a final highstand systems tract (Fig. 3.6C).

An erosional surface forms the base of the Santa Engracia sequence, which consists of significantly more terrigenous and coarser facies than the underlying Orcau-

Vell sequence (Guillaume et al. 2008, Simó 1989, 1985b). Part of the basal surface of the Santa Engracia sequence has been interpreted to be formed by a north-northwest oriented, gravity driven fault based on the interruption of the underlying systems tracts in the Orcau-Vell sequence (Figs. 3.5 & 3.6D). Déramond and others (1993) and Guillaume and others (2008) suggest that the fault created significant accommodation space for channelized, quartz rich slope fan and Gilbert type deltaic deposits with transport directions toward the southwest; these are interpreted as a falling stage systems tract (FSST) (Déramond et al. 1993, Guillaume et al. 2008, Simó 1985b). The upper surface of the slope fan and deltaic deposits is oxidized and represents significant base level fall and subaerial erosion (Guillaume et al. 2008). The upper Santa Engracia sequence consists of a carbonate marine transgressive systems tract overlain by a deltaic highstand systems tract (Déramond et al. 1993, Guillaume et al. 2008). Terrestrial fluvial deposits of the Garumnian facies overlie the Santa Engracia sequence and were deposited subsequent to late Cretaceous and earliest Paleocene folding and uplift of Sant Corneli anticline (Cuevas 1992, Rosell et al. 2001). The Garumnian facies are interpreted to have been deposited during a period of relative tectonic quiescence in the southern Pyrenees (Bond & McClay 1995, Déramond et al. 1993, Guillaume et al. 2008, Nagtegaal 1983, Simó 1985b). Subsequent uplift during the latest Eocene and Oligocene resulted in deposition of the Collegats conglomerates to the north of the study area (Mellere 1993, Puigdefàbregas et al. 1992).

3.4 Fold/Thrust Structure of Sant Corneli anticline

The major geomorphic expression of Sant Corneli anticline is defined by the Sant Corneli sequence, which is folded into an asymmetric, open anticline at the surface with a steep westward plunge of approximately 25° . While the backlimb is relatively planar, the transition on the fold nose from $\sim 25^\circ$ north dips in the backlimb to $\sim 50^\circ$ south dips in the forelimb occurs without significant kinking or faulting as evidenced by the continuous outcrop trace of the contact of the Sant Corneli sequence with the overlying marls (Fig. 3.5). In contrast, the transition from nearly horizontal dips on the crest of the anticline to steeper dips on the forelimb is abrupt in the core of the anticline (Fig. 3.5).

The subsurface structure of Sant Corneli anticline is only constrained by one ~ 3000 meter deep well in the backlimb of the anticline (SC-1, Fig. 3.5). The Sant Corneli-1 well penetrates an upright sequence of Triassic, Jurassic, and Cretaceous rocks overlying a fault, below which is an inverted and condensed Jurassic and Cretaceous sequence (Berástegui et al. 1990, Déramond et al. 1993, García-Senz 2002, Specht et al. 1991). Berástegui and others (1990) interpreted the fault to be the continuation of the Bóixols thrust, and García-Senz (2002) estimated between 2650 and 3580 meters of displacement at Sant Corneli anticline depending on the subsurface fault configuration. No evidence for large displacement faults is observed at the surface. A high angle, $\sim 80^\circ$ north dipping fault in forelimb of Sant Corneli Anticline separates rocks of approximately the same age (Santonian), but this fault does not appear to offset the top of the Sant Corneli sequence to the west (Fig. 3.5). Similar observations have been made in the Bóixols anticline to the east of Sant Corneli anticline (Fig. 3.2), where

a spectacularly exposed thrust fault with approximately 160 meters of displacement is fossilized by an unconformity at the base of the Aren group at Abella de la Conca (Banbury 2001, García-Senz 2002).

Various interpretations have been proposed that may account for the discrepancy between the displacement implied by the Sant Corneli-1 well and the lack of significant surface faulting. Specht and others (1991) and Deramond and others (1993) interpreted each of three successive unconformities in the Aren group to represent a blind thrusting episode, with each thrust steepening and accommodating some of the thrust displacement, but never emerging at the surface (Fig. 3.7A). Vergés (1993) interpreted the thrust to breach the surface within the Montesquiú/Vallcarga sequences in the forelimb of the anticline (Fig. 3.7B). Bond and McClay (1995) proposed that the Bóixols anticline may have formed by non-emergent fault propagation folding or break-thrust folding (Fisher et al. 1992, Suppe & Medwedeff 1990), though the authors do not explicitly address the discrepancy in displacement. Numerous authors have interpreted that the main Bóixols thrust breached the surface and was eroded by one or more of the intra-Campanian or Maastrichtian unconformities (Berástegui et al. 1990, García-Senz 2002, Garrido-Megías & Ríos Aragües 1972). According to this interpretation, the Bóixols thrust continues beneath Sant Corneli anticline and is buried by the Aren group somewhere beneath Orcau (Figs. 3.2 & 3.5).

Abrupt westward thickening of the Vallcarga and Aren groups results in significant discordance in orientation between the Campanian-Maastrichtian units and the Sant Corneli sequence (Fig. 3.5). The Aren group is only present in the forelimb and on the fold nose, where progressive folding during deposition is indicated both by

changes in sedimentary facies and sediment transport direction, as well as by progressive unconformities (Figs. 3.2 & 3.5). The Aren group thins dramatically to the east, where it lies unconformably on Santonian and older carbonate units showing the overall westward direction of lateral growth. In the forelimb east of Orcau (Fig. 3.5), the Sant Corneli sequence dips approximately $\sim 5\text{-}10^\circ$ steeper than the overlying Montesquiu/Orcau Vell sequence, which indicates relatively low structural relief of Sant Corneli anticline during deposition of the Montesquiu sequence (Figs. 3.5 & 3.6C). In the forelimb of the Bóixols anticline to the east (Fig. 3.2), the discrepancy in dip across the same boundary increases to $\sim 10\text{-}15^\circ$ (Banbury 2001), indicating that the Bóixols anticline probably had steeper forelimb dips than the Sant Corneli anticline during Montesquiu deposition. At Sant Corneli anticline, the next significant discrepancy in dip ($\sim 15^\circ$) within the Aren group is across the unconformity at the base of the Orcau-Vell sequence near Orcau. The dip discrepancy between the Orcau-Vell and the Santa Engracia sequences in the forelimb of the anticline is up to 35° in the eastern end of the study area, indicating significant folding and tilting of the strata east of Orcau during deposition of the Santa Engracia sequence.

The present limb dips of the Aren group at Sant Corneli anticline ($15\text{-}50^\circ$), as well as tilting of the overlying Garumnian rocks indicate that further folding and limb rotation occurred after deposition of the Aren group and the overlying Garumnian terrestrial deposits (Fig. 3.6F). The timing of this event is evidenced by deposition of the Collegats conglomerates (Fig. 3.5), which dip shallowly north, and unconformably overlie the Vallcarga sequence north of the study area (Fig. 3.4). These conglomerates filled an intramontane basin during Eocene-Oligocene time that is interpreted to have

formed in response to reactivation of the Bóixols thrust (Bond & McClay 1995, Mellere 1993, Puigdefàbregas et al. 1992).

3.5 Secondary Faulting at Sant Corneli anticline

N-NE to N-NW striking normal faults are the most predominant second order structures of Sant Corneli anticline (Figs. 3.5 & 3.8). Normal faults are best exposed in the backlimb of the anticline in the Sant Corneli sequence, though I also observe normal faulting in the Sant Corneli sequence in the forelimb, as well as in the Vallcarga and Montesquiu sequences in the forelimb, nose and backlimb (Fig. 3.8A). The largest N-NW striking fault in the backlimb offsets the top of the Sant Corneli sequence by approximately 100 meters with displacement down to the west (Fig. 3.5). Abundant smaller scale faults with meter and sub-meter scale offsets have $\sim 70^\circ$ dips and similar strike to the larger fault (Fig. 3.8B). Many of the fault planes are mineralized with sparry calcite fill and matrix supported fault breccias that thicken to cm scale where fault asperities create openings along the fault plane. In general, N-NW and N-NE striking normal faults in the Sant Corneli sequence contain only sparry calcite, with the exception of one well-exposed, low angle (NW striking, $\sim 45^\circ$ W dipping) normal fault east of the Sant Corneli-1 well (Fig. 3.5); this fault contains a 0.5 meter zone of brecciated wall rock fragments in a matrix of sparry calcite and hematite.

I mapped distributed normal faulting along the length the Sant Corneli anticline from the fold nose to the cylindrical part of the anticline to the east. Faults in the backlimb strike N-NW, while normal faults in the forelimb strike N-NE, forming an approximately radial pattern, although no significant E-W striking faults were observed

on the fold nose (Fig. 3.5). E-W striking normal faults radiate from the crest of the Bóixols anticline, but curve to a N-NW striking orientation as they approach Sant Corneli anticline (Banbury 2001, Grelaud et al. 2003). Banbury (2001) interpreted these fold-axis parallel normal faults to be a result of outer arc extension at Bóixols anticline. In addition to E-W, or fold-axis parallel normal faults, Banbury (2001) observed N-NW striking faults in the backlimb and N-NE striking faults in the forelimb of the Bóixols anticline that is similar to the pattern observed at Sant Corneli anticline. Banbury (2001) interpreted that these fold axis perpendicular faults also formed as a result of outer arc extension related to the plunge of the anticline based on the observation that displacement decreases toward the lower tips of many of these faults (Banbury 2001). Though the lower fault tips of fold axis sub-perpendicular normal faults are not observed at Sant Corneli anticline, the similarity in structural setting and the significant E-W curvature of the Sant Corneli sequence in the anticline suggests that these faults may have also formed in response to outer arc extension.

A preliminary study of paleo-fluid composition in the Sant Corneli-Bóixols anticlines reveals some insights into the fluid compositions of faults and thrusts at Sant Corneli anticline. Lebraña (2004) sampled calcites from sheared veins associated with thrusting in the Bóixols anticline, as well as a NW striking normal fault originating from the core of the Bóixols that intersects the Sant Corneli anticline (location “A” in Fig. 3.5). By sampling along grain transects in normal fault and thrust veins, Lebraña (2004) was able to document changes in fluid compositions within the veins. Fluids in the thrust and some normal faults show progressively increasing $\delta^{18}\text{O}$ at relatively constant $\delta^{13}\text{C}$ values, which may suggest that burial depth was increasing as fluids

precipitated in the thrust and some normal faults (Lebraña 2004). Fluids associated with a different normal fault exhibited similarly increasing $\delta^{18}\text{O}$, but with decreasing values of $\delta^{13}\text{C}$ over time. This evidence led Lebraña (2004) to suggest that hydrothermal fluids had infiltrated the normal fault during precipitation of vein fluids and that fluids in this normal fault were distinct from the thrust fault.

A relatively minor set of W-NW striking, apparent normal faults is also present in the backlimb. Only three faults of this orientation are mapped, though the parallel orientation of the River Carreu with respect to this set may hinder their recognition; two faults on the south side of the River Carreu dip north, while one fault on the north side of the river dips south (Fig. 3.5). Smaller scale faults of the same orientation are filled with calcite and hematite cements, many of which have slickensurfaces indicating normal displacement. The W-NW orientation of this set likely controls the present orientation of the River Carreu, which flows in a W-NW direction punctuated by abrupt bends near some of the larger N-NW striking faults. These faults are similar in orientation to axis sub-perpendicular faults in the core of the Bóixols anticline, but have significantly less displacement and are only observed in the backlimb of Sant Corneli anticline.

Extension associated with normal faulting in the Sant Corneli sequence is manifested as distributed low angle apparent normal faulting in the overlying Vallcarga and Aren marl units (Fig. 3.8A). Normal faults in the marls commonly have thin (1-3 cm) calcite fill, exhibiting multiple generations of slickensides that indicate predominantly normal displacement. Almost all faults in the Vallcarga and Aren marls have a ~5 cm oxidation halo of iron and goethite mineralization of the wall rock

surrounding the faults (Fig. 3.8A). The majority of these faults strike N-S (in their restored state), dip east, and appear to sole into shallow detachments above the top of the Sant Corneli sequence. Displacement on faults in the Vallcarga increases to the west, in some cases forming large blocks with growth stratigraphy. Simó and others (1989) attribute such structures to the onset of N-S compression and collapse of the outer margin towards the W-NW, forming the Pumanyons Olistostrome (Fig. 3.6A). Several N-S striking calcite veins with over a meter of coarse blocky calcite fill in the Orcau-Vell Sequence east of Orcau indicate that at least one phase of east-west extension also occurred after deposition of the Aren group.

N-NW striking, $\sim 50^\circ$ W dipping normal faults are also present in the Aren group, the most predominant fault being an inferred growth fault with approximately 150 meters of displacement in the upper Aren group (Figs. 3.5 & 3.6D) (Dérmond et al. 1993, Guillaume et al. 2008, Specht et al. 1991). Guillaume and others (2008) interpreted the fault to be a gravity driven collapse resulting from tilting and lateral propagation of Sant Corneli anticline at approximately 69 Ma.

3.6 Field mapping of fractures at Sant Corneli anticline

My field mapping of fractures (joints, small faults, and deformation bands) in the Aren and Sant Corneli sequences constrains the stress-strain history of the anticline. Fracture mapping of pavement outcrops facilitates documentation of the relative timing between fracture sets. Pavement outcrops of sandy lithologies in the Aren group provide the most robust timing relationships due to the size and quality of outcrop. In contrast, pavement outcrops in the less resistant Sant Corneli Sequence are generally

smaller with fewer cross cutting relationships preserved. Data collected at each site includes the orientation, length (parallel to bedding), height (perpendicular to bedding), presence or absence of fracture fill, fracture fill type, and terminations or cross cutting relationships. Because the focus of this study is to document the timing relationships between fracture sets and document the fracture history of the anticline, fracture intensity data was not extensively collected.

I first describe fracturing in the Aren group, where outcrops provide robust timing relationships between fracture sets. Because fractures in the Aren group are almost entirely on the forelimb of the anticline, I group fracture sets by orientation. I then describe fracturing in the Sant Corneli sequence and, where possible, relate fracture sets in the Aren group to fractures in the Sant Corneli sequence that have been distinguished based on orientation with respect to bedding, mode of formation, fracture fill, and scale with respect to bedding. In the following description and discussion, the term “joint” to refer to fractures with evidence of opening during formation, such as sparry or euhedral calcite fill, joint surface textures, planar and through-going fracture faces, and systematic fracture spacing (Pollard & Aydin 1988). I use the term “shear fracture” where fractures clearly initiated in shear and the term “fracture” where the mode of formation is unclear. Some fractures are not included in any fracture set in the field area. In many cases, such fractures may be similarly oriented to fractures of a nearby set, but are not included in the set because they have different distinguishing characteristics such length, width, fill type, or deformation mode (opening vs. shear).

3.7 Fractures in the Aren group

3.7.1 N-NW striking calcite filled joints (J2)

N-NW striking calcite filled joints in the Aren group are generally 0.5-3 meters in length and are very planar and systematic with spacing on the order of a meter to a few meters (Fig. 3.9). These joints are locally echelon and commonly have large apertures up to 4 mm that are healed by sparry and locally fibrous calcite cement (Fig. 3.10). Where observable, the spacing of N-NW filled joints scales to the thicknesses the shoreface and shallow marine sandstone lithologies in the Montesquiou and Orcau-Vell sequences, which tends to be 1-5 meters (Ardévol et al. 2000). N-NW striking joints maintain a consistent orientation for at least a few kilometers on either side of Orcau, but are not observed in the underlying Sant Corneli Sequence (Fig. 3.11).

3.7.2 NE striking deformation bands (DB1)

NE striking deformation bands with grain size reduction are only well developed in some of the shoreface and near shore sandstone facies (Fig. 3.12). Deformation bands are 2 – 50 cm in length, and are very sinuous, with variable orientations and locally anatomizing patterns. The spacing between deformation bands is usually similar to their length, and most appear to be approximately orthogonal to bedding. Deformation bands cross cut the calcite fill of N-NW striking filled (J2) joints and are therefore interpreted to post date the N-NW set (Fig. 3.10). Some deformation bands show indications of offset along their length, however, their mode of formation as compaction bands or shear bands has not been verified by thin section analysis.

3.7.3 N-NE striking, calcite filled joints (J1/J3)

In the Aren group, N-NE striking calcite filled joints range in length from a few centimeters to 2 meters in length with apertures up to 4 mm (Figs. 3.13 & 3.14). Cross cutting calcite fill of the different healed joint sets provides definitive evidence of joint relationships, but the relative timing of this set is complicated by conflicting cross cutting relationships. Though the orientation, size, and fill of N-NE striking joints is indistinguishable to the naked eye, some N-NE striking joints are cross cut by (Fig. 3.13), and therefore pre-date, N-NW striking calcite filled joints (J2); other N-NE striking joints post date and/or are associated with the N-NW striking (J2) set. Further evidence for late N-NE striking jointing includes N-NE striking joint splays off of N-NW striking joints and swarms of N-NE striking joints near some N-NW striking (J2) joints. Some N-NE striking joints cross cut NE striking deformation bands (DB1), which in turn, post date N-NW striking (J2) joints. This N-NE striking joint set probably includes at least two subsets formed before (J1) and after (J3) the N-NW striking (J2) set. Because I cannot distinguish these sub sets, I refer to this set at J1/J3.

3.7.4 W-NW striking, locally calcite filled joints (J4)

W-NW striking joints are among the most systematic in the Aren group, with lengths greater than 5 meters and spacing on the order of 1-5 meters (Figs. 3.9 & 3.15). W-NW joints usually span the thicknesses of the sandy facies in the Aren (1-5 meters thick) and are also commonly observed in the more resistant units of the finer grained, gray marls and deeper water facies, which suggests that they may span multiple stratigraphic units (Fig. 3.16). Many W-NW striking joints contain 1-3 mm of calcite

fill, though one of the defining features of the W-NW set is commonly reddish iron oxidation and goethite mineral staining along and in the wall rock adjacent to such fractures. Wall rock staining spans the range from 5-10 cm haloes of light colored goethite mineralization (Fig. 3.17) to lisegang banding in and around fractures (Fig. 3.18). W-NW striking joints consistently post-date both the N-NE striking joints (J1/J3) and the N-NW striking joints (J2) as indicated both by cross cutting calcite fill and by joint termination relationships (Figs. 3.9, 3.17, & 3.18). Some joints of this set are sinuous along their length. The tips of at least one W-NW striking joint is dissected into multiple en echelon segments, possibly indicating a mixed mode genesis or opening followed by left lateral shear; however, the systematic nature of this set suggests that they formed as opening mode.

3.7.5 E-NE striking locally calcite filled joints (J5)

E-NE striking calcite filled joints of the Aren group are similar in character to the W-NW striking joint, with lengths greater than 5 meters, local apertures of 1-2 mm, and similar iron oxidation and goethite mineralization (Fig. 3.18). E-NE striking joints are generally more poorly developed than W-NW striking joints and are more commonly observed in the western end of the field area (Fig. 3.19). E-NE joints locally cross cut the W-NW striking (J4) set, but the two sets may be coeval (Fig. 3.16).

3.8 Fractures in the Sant Corneli Sequence

Because bed strike changes rapidly in the Sant Corneli sequence (Fig. 3.5), absolute fracture orientation, or even fracture orientation after unfolding cannot be the sole criterion that delineates fracture sets; sets of fractures are distinguished by a variety

of characteristics including fracture orientation with respect to bed strike, fracture fill type or absence of fill, fracture scale (length and width), and timing relationships with respect to other fractures. I group fractures in the Sant Corneli sequence by their orientation with respect to present day bed strike at each sample site, although I acknowledge that bed strike may have changed during fold evolution. Each fracture set maintains consistent timing relationships within the Sant Corneli sequence and with respect to fracture sets within the Aren group, which suggests that distinguishing fractures based on present day bed strike is a valid first approximation.

3.8.1 Bed strike-perpendicular calcite filled joints (J1/J3)

N-NW striking (backlimb) and N-NE striking (forelimb) calcite filled joints are present at a variety of scales, from cm to meter scale in the Sant Corneli sequence. These joints usually have 1-4 mm of sparry calcite fill, with sharp, planar contacts with the surrounding wall rock (Fig. 3.20). Joints of this set have similar strike to, and consistently increase in intensity near, N-NW striking normal faults in the backlimb (Figs. 3.5, 3.8, & 3.14) and N-NE striking normal faults in the forelimb (Fig. 3.5). Bed strike-perpendicular joints are also observed where no normal faults have been observed (Fig. 3.14), though their spacing increases from less than half a meter near faults to meter scale spacing in un-faulted areas. This joint set is similar to J1/J3 joints in the Aren group in three ways. First, they span a wide range of length/height scales from cm to meter scale, and have similar sparry calcite fill. Second, both sets have a wide dispersion in dip, and have similar strike when grouped by structural position (Fig. 3.14 inset stereonet). Third, bed-strike perpendicular joints in the Sant Corneli

sequence consistently pre-date bed-oblique joint sets in the same way that J1/J3 joints in the Aren sequence pre-date J4/J5 joints.

3.8.2 Bed strike-oblique, calcite filled joints with iron oxidation (J4)

Bed strike-oblique, locally calcite filled joints in the forelimb of Sant Corneli anticline have outcrop trace lengths on the order of a meter or larger, with spacing greater than 0.7 meters (Fig. 3.15). The trace in pavement outcrop of these joints is usually oriented less than 45° from bed strike in a clockwise sense (Fig. 3.21). These joints have relatively thin (<2mm) to absent calcite fill and are locally mineralized with reddish iron oxidation and goethite mineral staining. In coarser wackestone/packstone lithologies, joints of this set are sinuous along their traces, with deviations from planarity on the order of a few millimeters to 2 cm (~0.5 cm “wavelength”). Cross sectional exposures in the backlimb of the anticline indicate that some joints of this set have heights (perpendicular to bedding) of 10’s of meters. Bed strike-oblique joints of this set consistently cross cut bed strike-perpendicular joints of the J1/J3 set (Fig. 3.20).

3.8.3 Bed strike-oblique, calcite filled joints with iron oxidation (J5)

I distinguish a second bed strike-oblique, calcite filled joint set in the Sant Corneli sequence, whose trace in pavement outcrops is oriented 45° or less counterclockwise from bed strike (Figs. 3.19 & 3.21). Joints of this set are similar in character to J4 joints in the Sant Corneli sequence and the Aren group in that they are locally sinuous, locally calcite filled, have associated iron oxidation, and post date bed strike-perpendicular joints (Fig. 3.20). Like J5 joints in the Aren group, this joint set is generally smaller in scale, has larger spacing, and is poorly developed relative to the J4

set in the Sant Corneli sequence, though the two sets intersect and share calcite fill at at least one sample site (Fig. 3.20).

3.9 Discussion and Interpretations of Fold-Fracture Evolution

While the tectono-stratigraphic evolution of the Sant Corneli-Bóixols anticlines has been well documented, relatively few studies have extensively incorporated faulting and fracture timing relationships into their structural evolution. Here I discuss the relative timing of fracture sets with respect to the major structural and depositional episodes at Sant Corneli anticline.

3.9.1 J1/J3 Joints

N-NE striking joints in the forelimb and N-NW striking joints in the backlimb form an approximately radial set of joints at Sant Corneli anticline, and may be associated with similarly oriented fold axis sub-perpendicular normal faults (Figs. 3.5 & 3.14). This interpretation is supported by increasing intensity of J1 joints near these faults, the similarity in strike of the joints and faults, and that both the faults and the joints are mineralized with sparry calcite. While many of the axis sub-perpendicular faults and joints could potentially be as old as the basin margin collapse during Pumanyons time (Simó 1989), some J1 joints must have formed after deposition and lithification of the Orcau-Vell sequence that they fracture. This suggests that axis sub-perpendicular normal faulting occurred throughout the early development of Sant Corneli anticline.

The orientation of J1/J3 joints and similarly oriented normal faults in the study area (e.g. Fig. 3.8) imply approximately fold axis-perpendicular stretching, although the

radial pattern of their strikes in map view suggests some stretching parallel to bed strike (Figs. 3.5 & 3.14). The lack of faulting and J1/J3 jointing on the outer fold nose where bed strike approaches N-S (Fig. 3.5) suggests that these structures are not due exclusively to bed strike-parallel stretching, which should produce a uniform distribution of faults and joints around the anticline. The stratigraphic history of Sant Corneli anticline indicates a predominantly westward deepening basin and multiple stages of collapse of the margin (Fig. 3.6). Thus, these structures may be associated with collapse of the basin margin toward the west, but were clearly influenced by folding as indicated by their radial pattern about the anticline.

An alternative hypothesis is that J1/J3 joints and similarly oriented faults accommodated outer arc stretching associated with the relatively steep plunge of the anticline. Banbury (2001) observed that the displacement of radial normal faults in the Bóixols anticline decreased downward toward their lower fault tips, consistent with an interpretation of outer arc stretching. Despite the lack of exposure to document displacement profiles of similar faults at Sant Corneli anticline, the similarity in structural position and strike of these fault and joint sets at Sant Corneli and Bóixols anticline suggests that they may have formed due to similar mechanisms. Radial faults in the Bóixols anticline were also interpreted to have localized sediment dispersal during earliest Maastrichtian time when the Bóixols anticline was a relatively low-relief structure (Banbury 2001). Growth strata relationships suggest that Sant Corneli anticline formed after the Bóixols anticline, therefore while the development of the folds is similar, the timing of radial faults and J1/J3 joints would be different in the two anticlines.

3.9.2 J2 Joints

I propose two hypotheses for the formation of J2 joints in the study area. J2 joints may have formed in response to flexure and/or layer parallel extension within the footwall of the interpreted gravity driven fault in the western end of the field area (Figs. 3.5 & 3.6B). Such faulting is expected to produce opening mode fractures parallel to the fault and localized within the units above the detachment, however, the orientation of the fault is not well constrained because the fault is not well exposed at the surface. J2 joints are localized within the Aren group, which is consistent with the interpretation that the detachment soles into the lower the Montesquiou or Vallcarga sequence (Guillaume et al. 2008). Guillaume and others (2008) interpreted the gravity driven fault to have resulted from westward propagation of Sant Corneli anticline from the Bóixols anticline to the east. If westward propagation of Sant Corneli did cause gravity faulting, J1 and J2 joints should have formed at approximately the same time.

An alternative hypothesis for J2 joints is that they are associated with outer arc stretching of the underlying Sant Corneli sequence. J2 joints are perpendicular to bed strike in most of the Aren sequence, but are also approximately perpendicular to the direction of curvature in the Aren Group as the sequence wraps around the anticline (Fig. 3.20). Decoupling of the Aren Group from the underlying Sant Corneli sequence probably occurs along the structurally compliant Vallcarga sequence, which should allow the Aren Group to behave independently from the Sant Corneli sequence. Thus, I cannot rule out folding, or more specifically plate bending, as a direct mechanism for J2 joint formation.

3.9.3 DB1 Deformation Bands

Because the deformation mode of deformation bands in the Aren group is unclear, their origin is difficult to interpret. Deformation bands post date J2 joints, but are cross cut by J3, J4, and J5 joints, which implies that they occurred in the early or intermediate stages of folding. Further microstructural analysis to document the mode of formation of these structures is required to understand their context within the structural evolution of Sant Corneli anticline.

3.9.4 J4/J5 Joints

J4/J5 jointing is distinguished from older joint sets in the area by cross cutting relationships, the close association of J4 and J5 joints with each other, and by distinct iron oxidation and goethite mineralization of the wall rock along the two sets (Figs. 3.17, 3.18, & 3.20). Oxidation of J4 and J5 joints is probably not solely a result of recent flow of groundwater along these fractures because oxidation haloes are observed along healed joints that are not conducive to present-day fluid flow (Figs. 3.17 & 3.18). Similarly, joints healed by calcite cannot effectively conduct subsurface fluids, thus oxidation haloes along healed joints suggest that either the oxidizing fluids pre-date the calcite mineralization or that the calcite precipitating fluids are caused the oxidation. Regardless of the timing of oxidation, the geochemistry of fluids associated with J4/J5 joints was distinctly different from fluids associated with older sets that do not have wall rock oxidation.

J4/J5 joints are interpreted to be a result of outer arc extension of the anticline during the main stage of flexure and folding of Sant Corneli anticline. Regional studies

and growth strata relationships suggest that the Bóixols thrust was active during the latest Cretaceous and earliest Paleocene and was reactivated during the Eocene-Oligocene time (Muñoz 1992, Puigdefàbregas et al. 1992, Vergés 1993). Therefore, J4/J5 jointing may have occurred as the last stage of Cretaceous-Paleocene(?) deformation or during reactivation of the Bóixols thrust in the Eocene-Oligocene. J4/J5 joints are oblique with respect to bed strike and the fold axis, and therefore are not consistent with conceptual models for fold related fracturing (Stearns 1967, Stearns & Friedman 1972); however, plate bending models of non-cylindrical folds like Sant Corneli anticline predict joints oriented oblique to bed strike and the fold axis (Davis 2004, Fischer & Wilkerson 2000). Structural restoration and unfolding of the Garumnian units may constrain the fold shape during this period, which could be used to test the hypothesis that J4/J5 resulted from outer arc extension of the anticline.

The presence of iron oxidation and goethite mineralization along healed joints suggests a significant influx of fluids enriched in meteoric water during or shortly after J4/J5 jointing (Fig. 3.17 & 3.18) (e.g. Chan et al. 2004, Chan et al. 2006). Oxidizing fluids clearly penetrated through the Vallcarga sequence into the Sant Corneli Sequence, as indicated by dark, hematite mineralization associated with N-S and N-NW striking faults in the backlimb of the structure, as well as J4/J5 joints (Figs. 3.8 & 3.20). Oxidizing fluid mineralization may have been facilitated by fluid flow along ~N-S striking normal faults in the marls of the Montesquiú and Vallcarga sequences (Fig. 3.8A), which pre-date the J4/J5 joints and show similar wall rock staining and calcite fill.

The source and timing of meteoric fluid infiltration of J4/J5 joints is uncertain. Direct infiltration of meteoric fluids into joints in the Aren group during J4/J5 jointing is plausible because the anticline may have been active during deposition of terrestrial rocks in the earliest Paleocene (youngest Santa Engracia sequence and oldest Garumnian facies, Figs. 3.4, 3.6E, 3.6F). J4/J5 jointing during the latest Cretaceous or earliest Paleocene would require that the Santa Engracia sequence, which contains J4/J5 fractures, be lithified relatively shortly after deposition. Terrestrial rocks were also in direct contact with the Aren group during later Eocene-Oligocene reactivation of the Bóixols thrust, which could have provided a potential source for oxidized Fe bearing fluids. Ar^{40}/Ar^{39} geochronology has been used to date iron and manganese mineralization along veins and fractures to date the influx of meteoric waters (Chan et al. 2001, Vasconcelos 1999). Such analyses could provide a means of testing my interpretations by bracketing the age of J4/J5 jointing.

3.10 Implications for the tectonic history of the Sant Corneli-Bóixols anticlines

Fracture timing relative to stratigraphic and structural events provides insights into the structural evolution of Sant Corneli anticline. The timing of J1, J2, and J3 joints relative to one another suggests that fold-axis perpendicular normal faulting was a relatively continuous process throughout the early growth of the anticline, which probably occurred during Campanian and Maastrichtian time (Figs. 3.5 & 3.6D). I suggest two hypotheses for the formation of radial normal faults. Outer arc extension parallel to the fold axis as suggested by Banbury (2001) could produce radial joint and fault patterns, however, I cannot rule out basin margin collapse throughout fold growth

as a mechanism for radial normal fault formation. Both processes would likely occur throughout the folding process, which is consistent with my observations of fault related joints (J1 and J3) that occur during multiple stages of folding. J2 joints may have formed in response to gravity faulting interpreted by Guillaume and others (2008) or as a result of outer arc extension of the Aren Group. The similarity of calcite precipitated along joints and associated faults (Figs. 3.10 & 3.13), as well as the lack of significant oxidation in J1, J2 and J3 joints (Fig. 3.17 & 3.18) suggests that these joints formed in a system dominated by hydrothermal fluids, possibly when the anticline was at or below sea level.

Late stage joints (J4/J5, Figs. 3.15, 3.17, 3.18, 3.19, 3.20, & 3.21) are generally closer to bed strike and are commonly associated with goethite and iron oxidation, which I interpret to be a result of infiltration of meteoric fluids into the system. Thus, I can constrain the timing of the fracturing relative to not just other fracture sets, but to the structural/stratigraphic context. I suggest that J4/J5 jointing occurred either during the last stages Cretaceous-Paleocene(?) thrusting or during Eocene-Oligocene reactivation of the Bóixols thrust (Fig. 3.6F). Further studies could refine the timing of J4/J5 jointing by dating the timing of oxidation of the joints.

3.11 Conclusions and implications for studies of fold related fracturing, faulting, and fluid flow

The results of this study demonstrate the necessity of distinguishing fracture sets based on a variety of characteristics and not solely on their present orientation. Plate bending models and mechanical models for folding predict spatially heterogeneous stress fields around non-cylindrical structures where local bed orientation may change

rapidly over short distances (Fischer & Wilkerson 2000, Hennings et al. 2000, Maerten 1999, Moretti et al. 2006, Stearns 1967, Stearns & Friedman 1972, Szilard 1974). Thus, the fracture sets associated with non-cylindrical folding may correlate better with local bed strike than with a fixed structural orientation (Fig. 3.21). Fracture, mode, mineralization, and size can be used in conjunction with orientation to group fracture sets that may have formed in response to spatially heterogeneous stress fields. Additionally, sequential restoration of syn-tectonic strata can constrain transitional fold shapes and the stress/strain history of fault related folds. Where syn-tectonic strata are absent, forward modeling and interpolation between deformed and restored states may be used to constrain transitional fold shapes.

Many of the fracture sets and faults at Sant Corneli anticline are mineralized with calcite and other cements that indicate the importance of such structures for fluid flow in the anticline. The distinct difference in cementation between J1, J2, J3 joints (calcite only) and J4/J5 joints (calcite with hematite/goethite) indicate that fluid flow regimes may change drastically during folding. Furthermore, cross cutting relationships of different phases of calcite fill (e.g. Figs. 3.13, 3.17, 3.18, & 3.20) suggest that healing of joint sets can be relatively common. I have also documented selective fluid flow along J4/J5 joints and not J1, J2, and J3 joints (Fig. 3.17) that I interpret to have occurred during the late stages of folding. Geochemical analyses and fluid inclusion analyses of calcite filled fractures and faults could further constrain the timing and boundary conditions (pressure/temperature) under which many of the fracturing events occurred. While healing of fractures has long been known to decrease or prohibit fracture permeability, the observation of multiple fluid flow regimes within Sant

Corneli anticline along different joint sets has implications for fluid flow modeling in fault related folds. Specifically, this suggests that fluid flow through fractures should not be modeled assuming all fractures are conductive at the same time; in fact, at Sant Corneli anticline fluids may have only migrated through a single fracture set over a specific time interval before being healed.

3.12 Figures

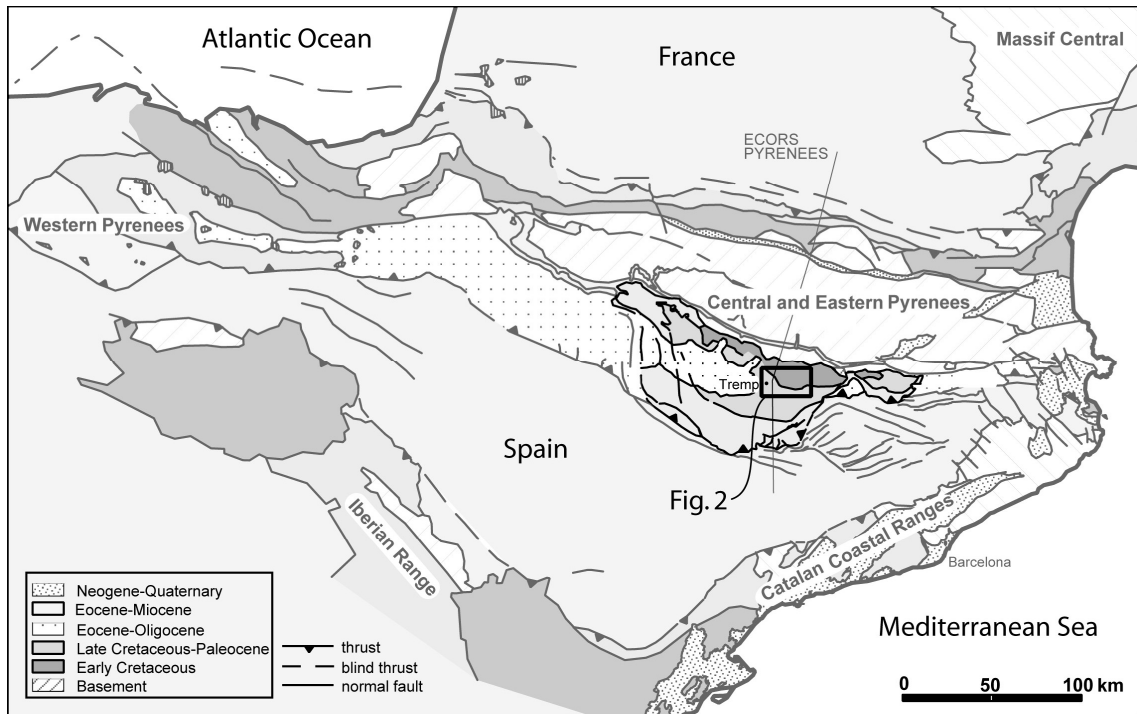


Figure 3.1 Generalized map of the Spanish Pyrenees showing the location of the major thrusts. The Southern Central Unit, a thrust bounded block containing the Boixols thrust and Sant Corneli Anticline, is highlighted in the center of the map. (modified from Vergés, 1993).

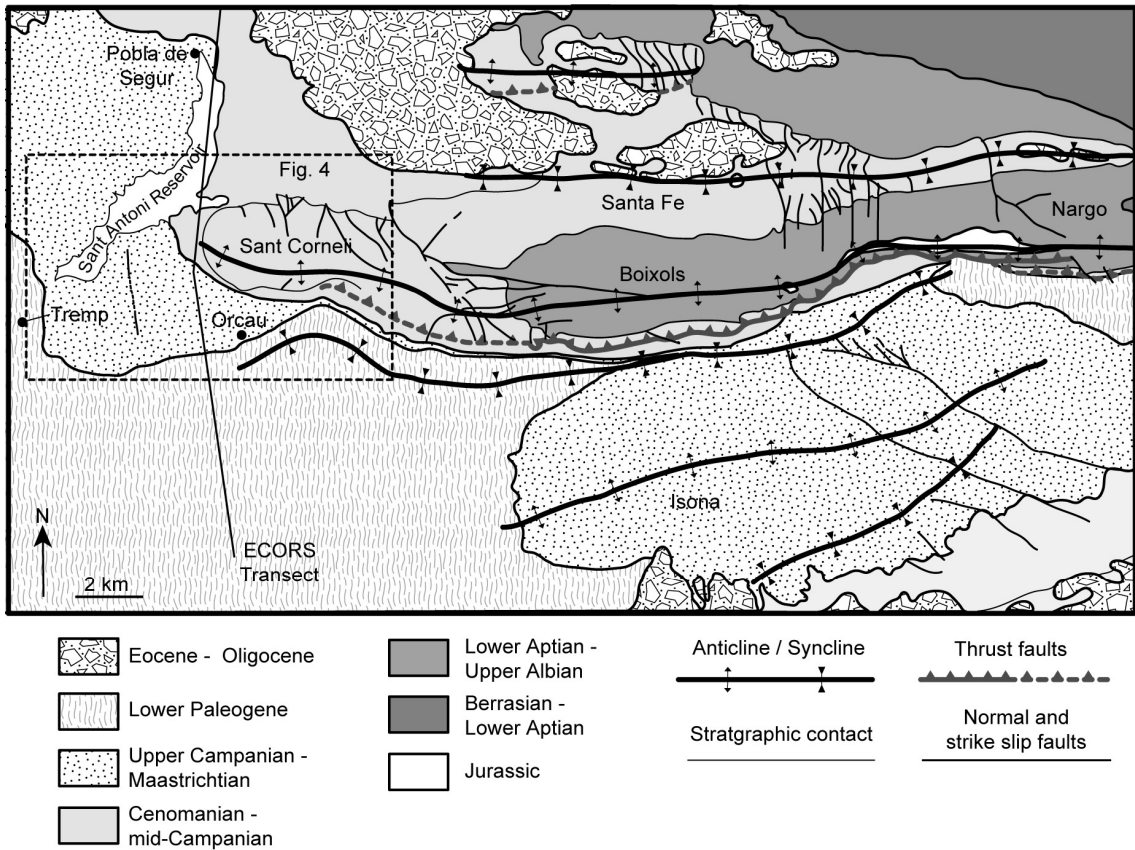


Figure 3.2 Geologic map of the Sant Corneli-Boixols-Nargo anticline. Thrusts shown at the surface south of the Sant Corneli and Boixols anticlines represent relatively small displacement thrusts that splay off of the main Boixols thrust, which is not exposed at the surface. The dotted box indicates the boundaries of the study area and the location of Fig. 3.5. (modified from Bond & McClay, 1995).

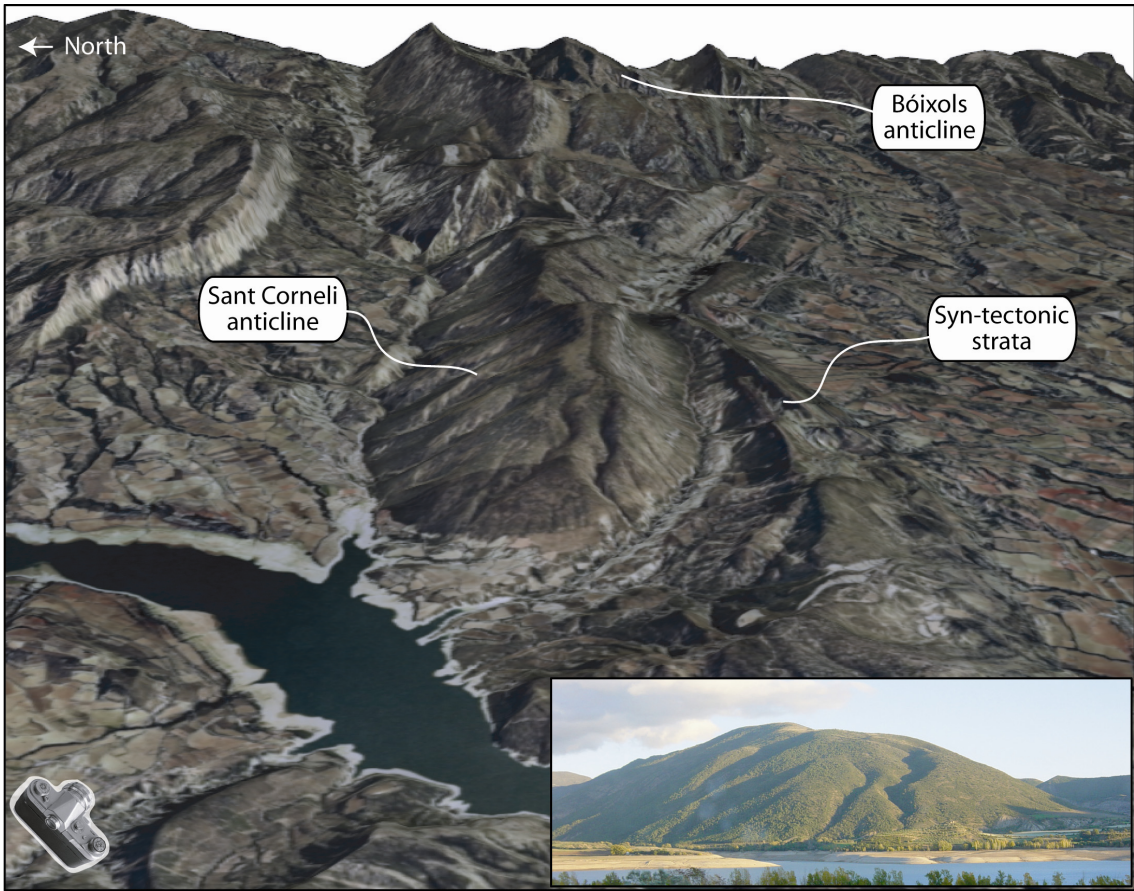


Figure 3.3 Digital elevation model with orthophoto drape of Sant Corneli anticline.

View is east. The topographic expression of Sant Corneli mountain roughly corresponds to the shape of the Sant Corneli sequence. Camera image (bottom right) shows the viewing direction of the inset photo, which shows the shape of the backlimb and fold nose.

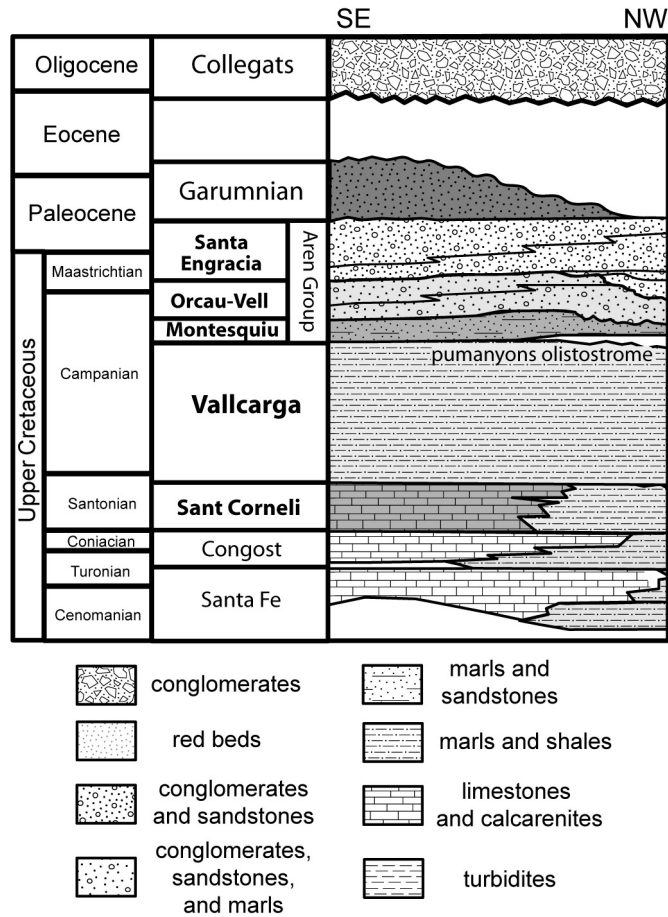


Figure 3.4 Simplified stratigraphic section showing the major stratigraphic sequences. Names in bold represent sequences referred to in the text and shown on Fig. 3.5, other names (non-bold) refer to formation or facies names unless otherwise specified. (modified from Deramond and others, 1993, Bond & McClay, 1995, and Ardevol and others, 2000).

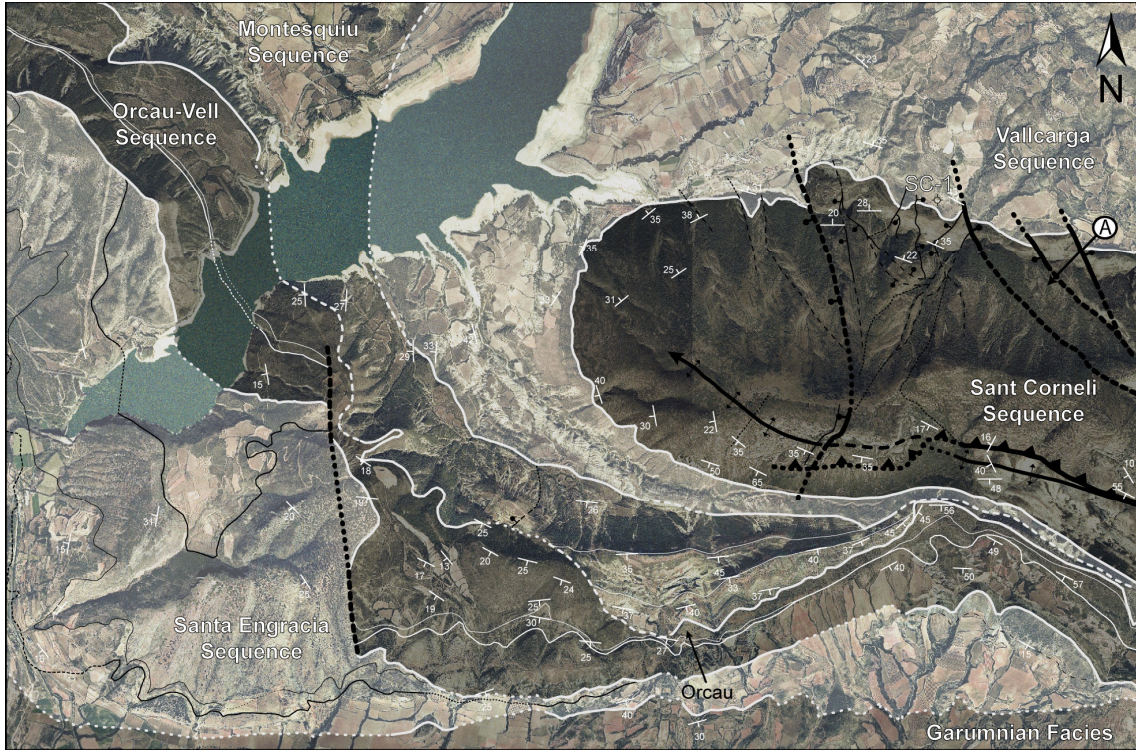


Figure 3.5 Geologic map of the study area showing the major structural elements and stratigraphic sequences. Solid lines indicate exposed contacts, dashed lines indicate covered or poorly exposed contacts, and dotted lines indicate inferred contacts. The location of fluid inclusion sample by Lebraña (2000) is indicated at A (see text for details). SC-1 indicates the location of the Sant Corneli-1 well. (Orcau-Vell and Santa Engracia contacts modified from Guillaume and others, 2008).

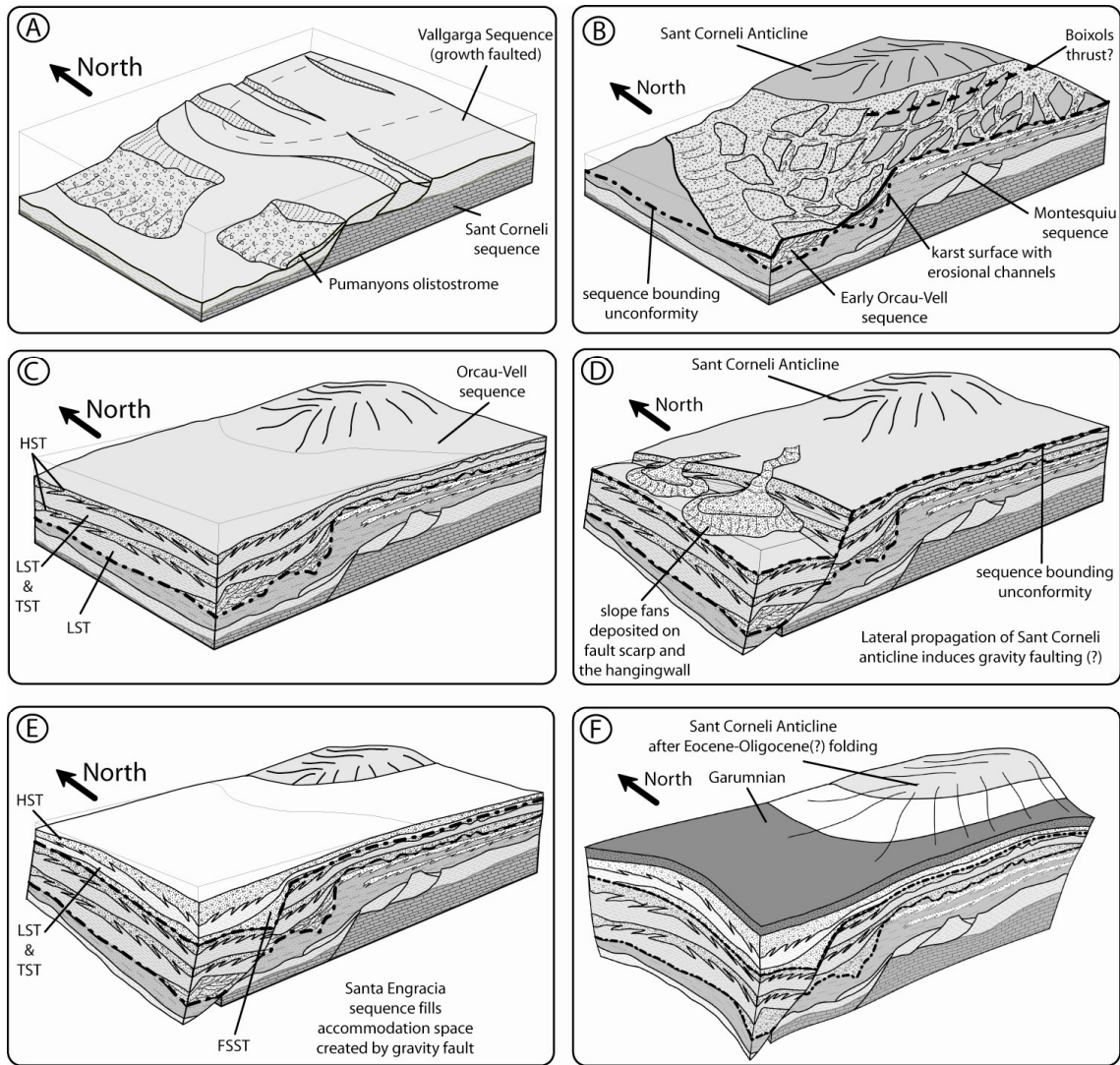


Figure 3.6 Simplified paleogeography and structural evolution of the study area. A) earliest Montesquiu time, B) earliest Orcau-Vell time, C) end of Orcau-Vell time, D) earliest Santa Engracia time, E) end of Santa Engracia time, F) after (Eocene-Oligocene) folding of the Santa Engracia and Garumnian sequences. HST: highstand systems tract, LST: lowstand systems tract, TST: transgressive systems tract, FSST: falling stage systems tract.

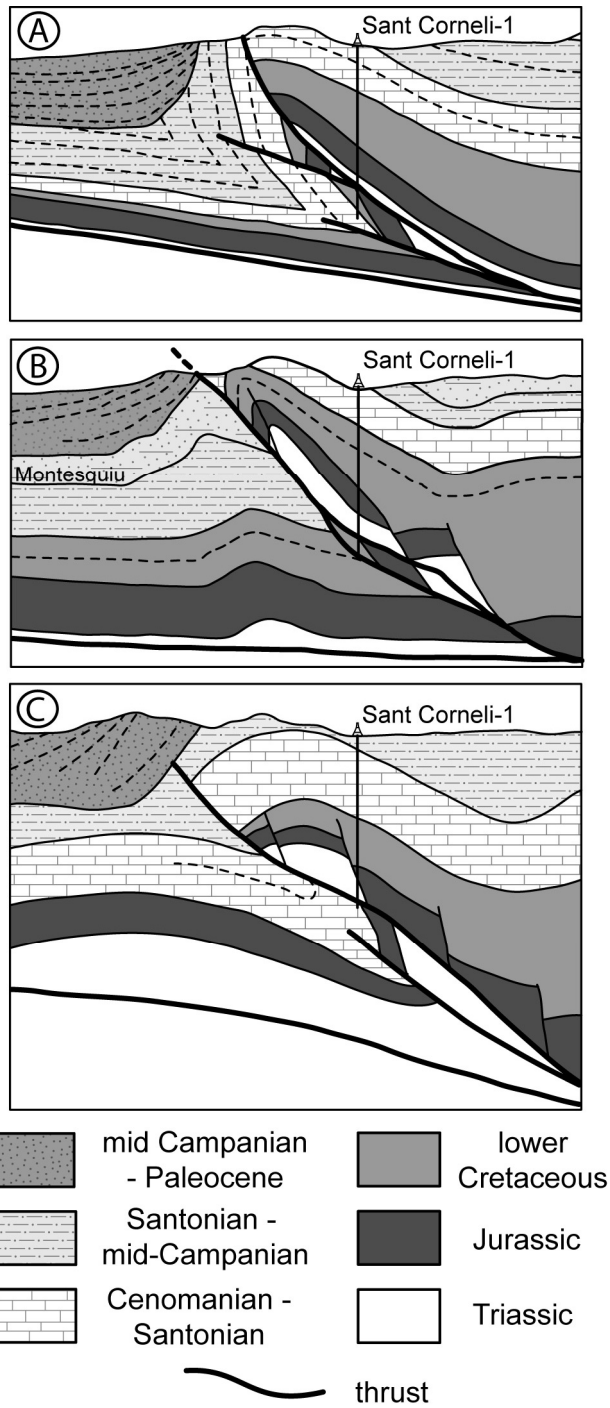


Figure 3.7 Cross sections through Sant Corneli anticline along or near the ECORS transect. A) Deramond and others (1993), B) Vergés (1993), and C) García-Senz (2002).

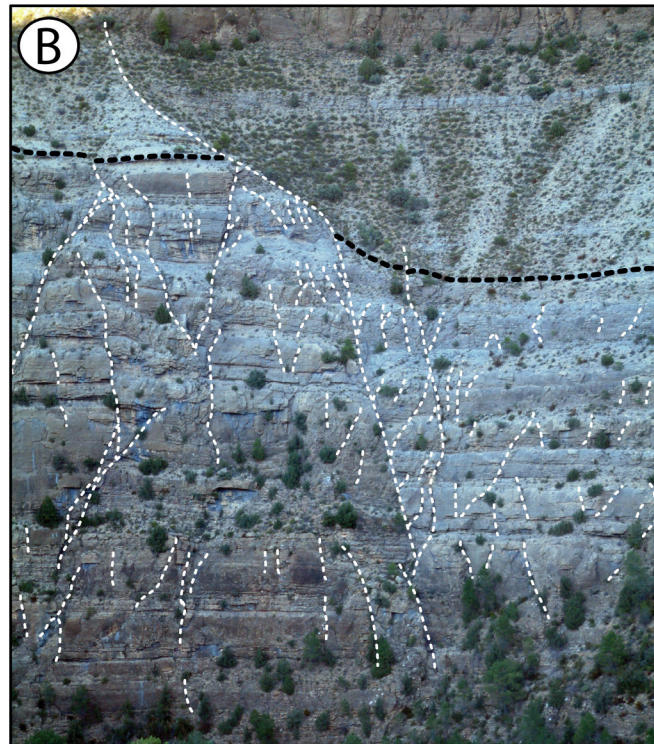


Figure 3.8 Photos of normal faults in the field area. A) View south at a typical N-S striking low-angle fault in the Vallcarga sequence (backlimb). The faults are mineralized with calcite and contain haloes of goethite and other Fe (Mn?) oxides that stain the wall rocks. B) View south of NW striking faults in the backlimb of Sant Corneli anticline. Faults are denoted by dotted white lines. An offset marker horizon at the base of an interbedded calc-arenite/marl unit is shown in black.

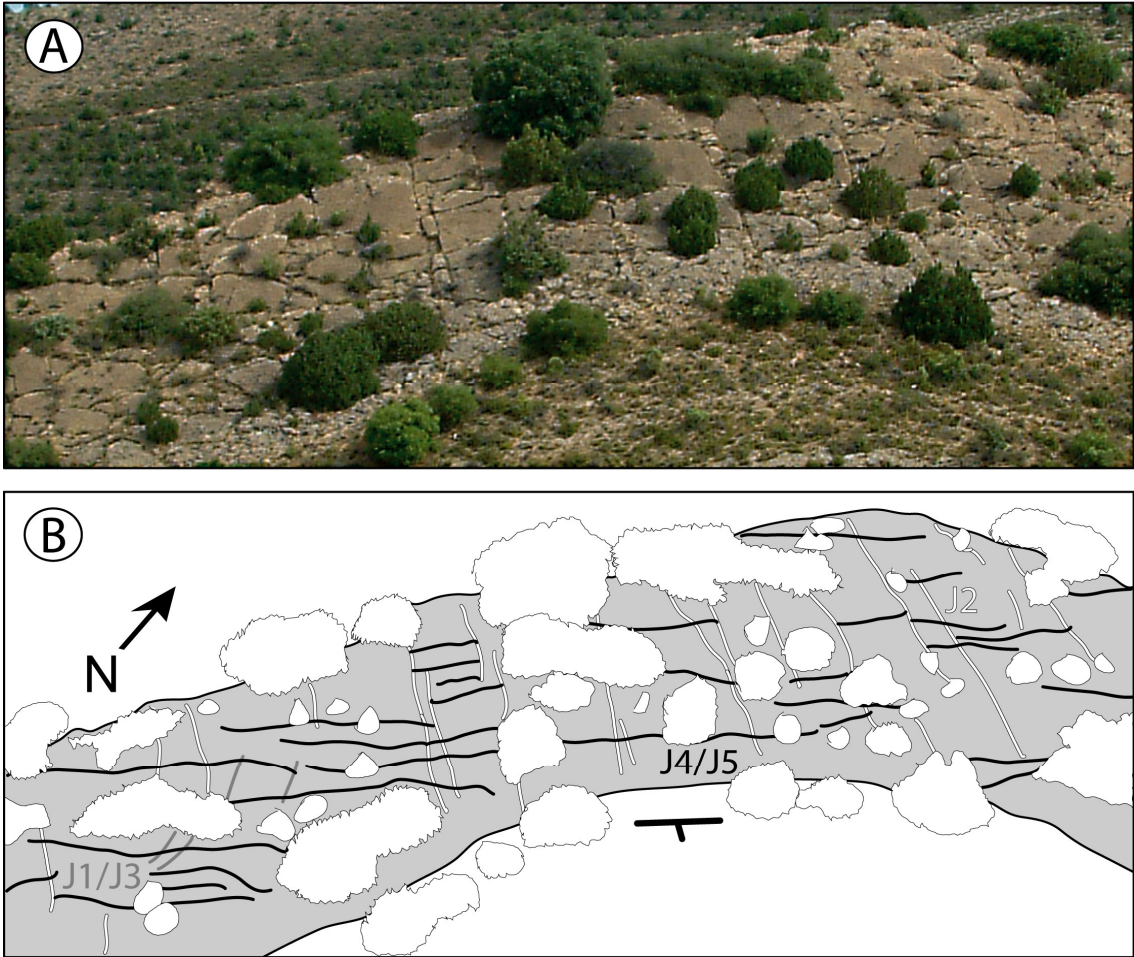


Figure 3.9 View northwest at a pavement outcrop in the Montesquiu sequence near Orcau. A) image, B) interpretive sketch.

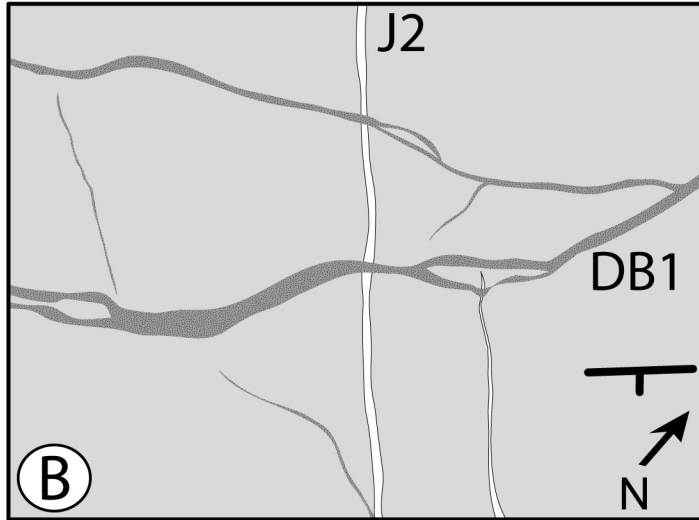


Figure 3.10 Close up view of calcite fill of J2 joints cross cut by deformation bands (DB1) in pavement view. A) image, B) interpretive sketch.



Figure 3.11 Map of J2 joint strikes in the study area. White ticks indicate the strikes of J2 joints rotated to bed-horizontal. Black ticks indicate the strikes of all other joint sets rotated to horizontal about the fold axis. Inset stereonet shows planes of J2 joints rotated to bed-horizontal. Circles with arrows indicate the numbers of figures showing J2 joints.

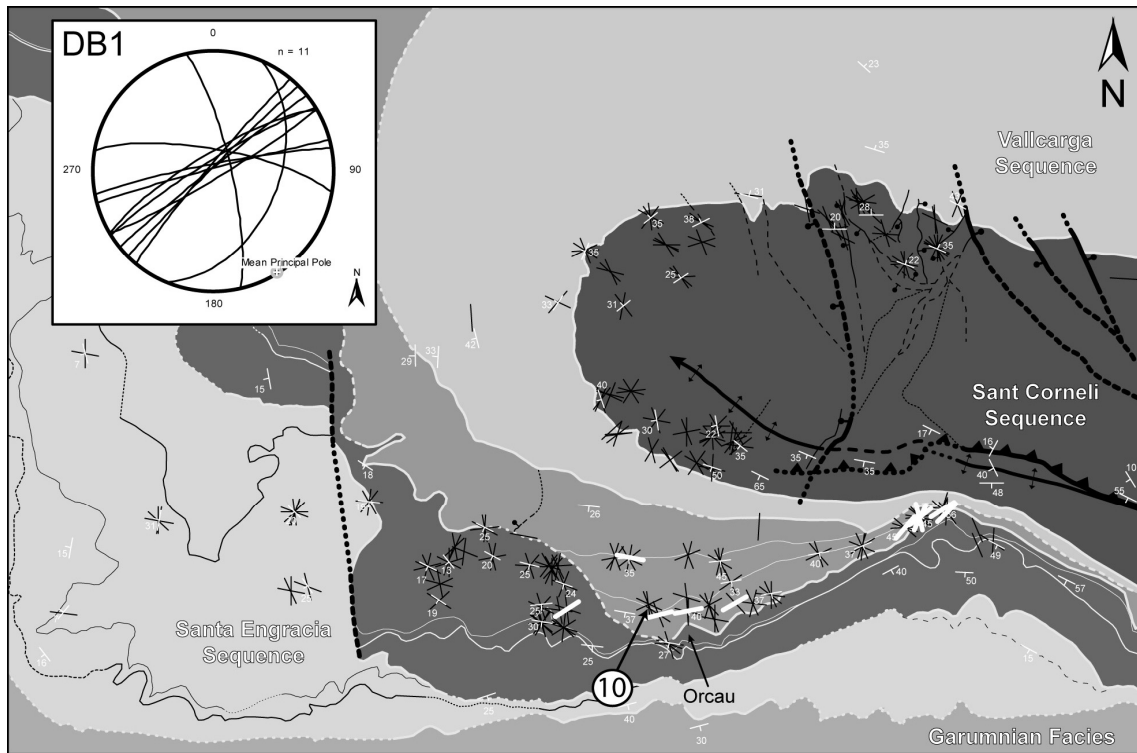


Figure 3.12 Map of deformation band strikes in the study area. White ticks indicate the strikes of deformation bands rotated to bed-horizontal. Black ticks indicate the strikes of all other joint sets rotated to horizontal about the fold axis. Inset stereonet shows planes of deformation bands (DB1) rotated to bed-horizontal. Circles with arrows indicate the numbers of figures showing deformation bands.

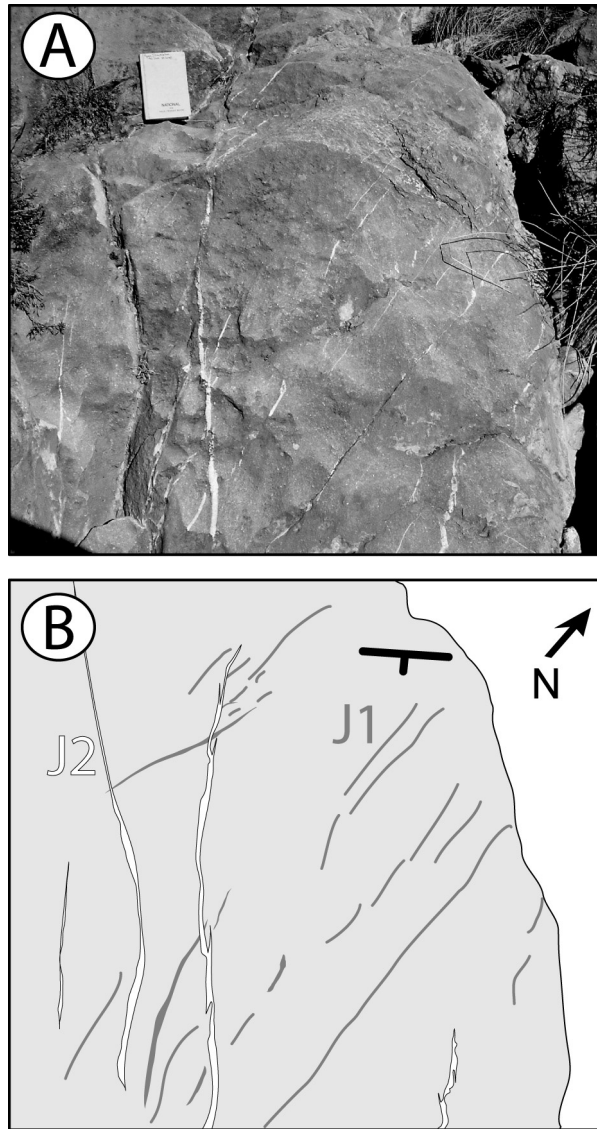


Figure 3.13 J2 joints cross cutting J1 joints in the Montesquiu sequence. A) image, B) interpretive sketch. At nearby outcrops, N-NE striking joints (J3) that are similar to the J1 joints cross cut, and therefore post date the J2 set, indicating subsets of N-NE striking joints.

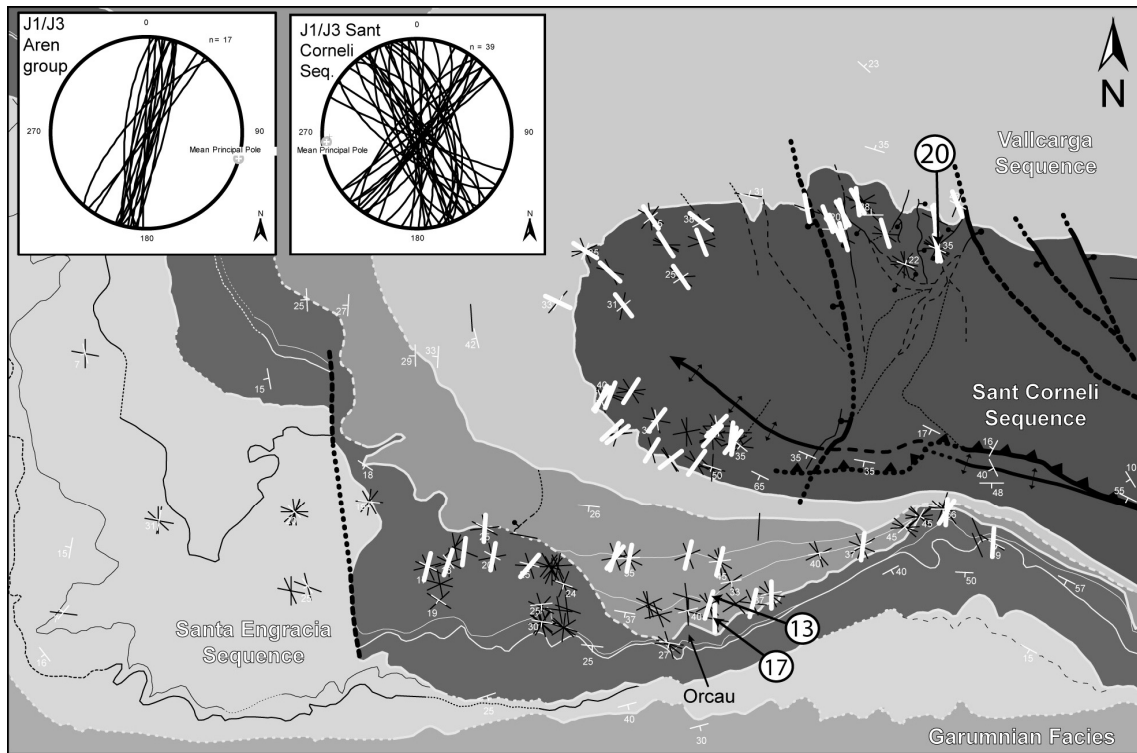


Figure 3.14 Map of J1/J3 strikes in the study area. White ticks indicate the strikes of J1/J3 joints rotated to bed-horizontal. Black ticks indicate the strikes of all other joint sets rotated to horizontal about the fold axis. Inset stereonet shows planes of J1/J3 joints in the Aren Group and Sant Corneli sequence rotated to bed-horizontal. Circles with arrows indicate the numbers of figures showing J1/J3 joints.

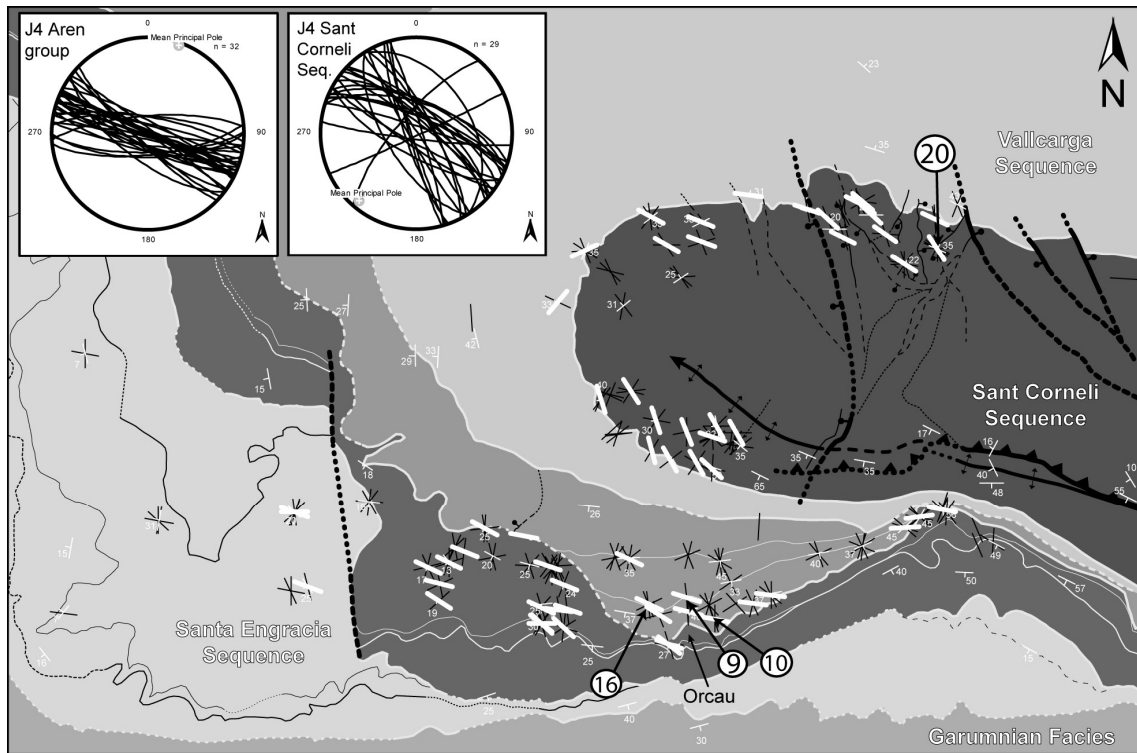


Figure 3.15 Map of J4 strikes in the study area. White ticks indicate the strikes of J4 joints rotated to bed-horizontal. Black ticks indicate the strikes of all other joint sets rotated to horizontal about the fold axis. Inset stereonet shows planes of J4 joints in the Aren Group and Sant Corneli sequence rotated to bed-horizontal. Circles with arrows indicate the numbers of figures showing J4 joints.

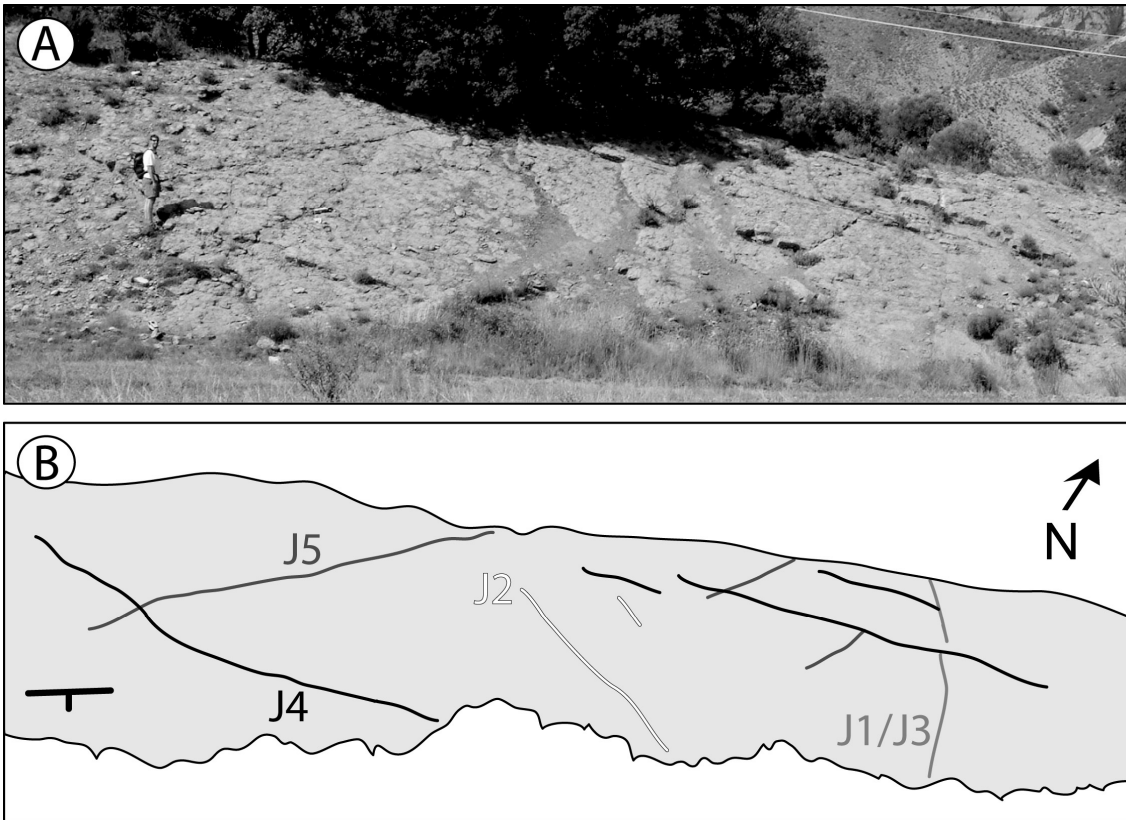


Figure 3.16 View northwest at a pavement outcrop in marls of the Montesquiu sequence showing relationships of joints to bed strike. A) image, B) interpretive sketch.

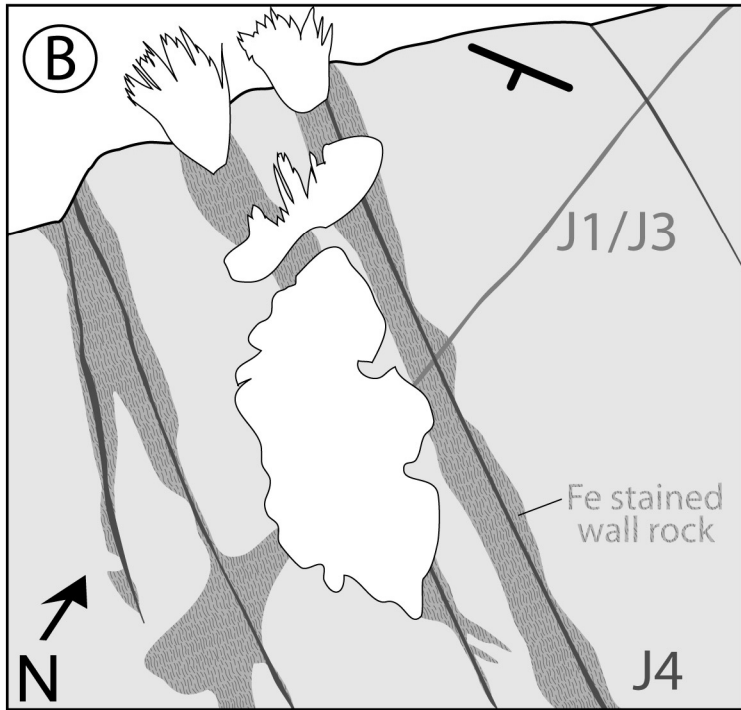
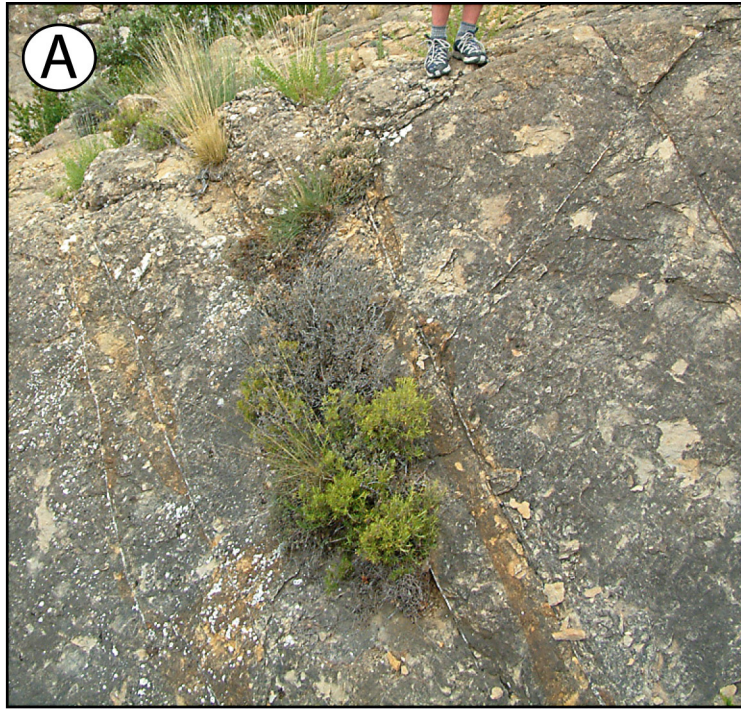


Figure 3.17 Bed-strike oblique (east) view of a pavement outcrop J4 joints showing reddish goethite “haloes”. A) image, B) interpretive sketch. Notice that J1/J3 joints immediately adjacent to the J4 joints have no associated oxidation.

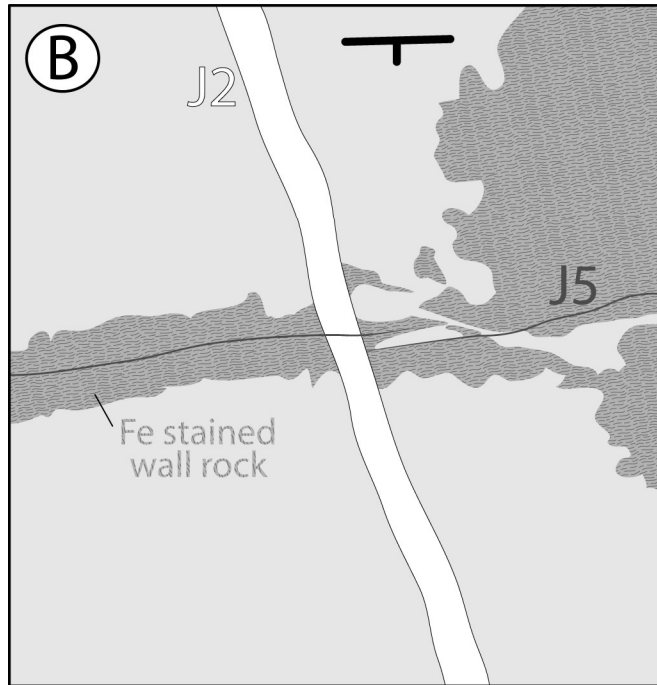
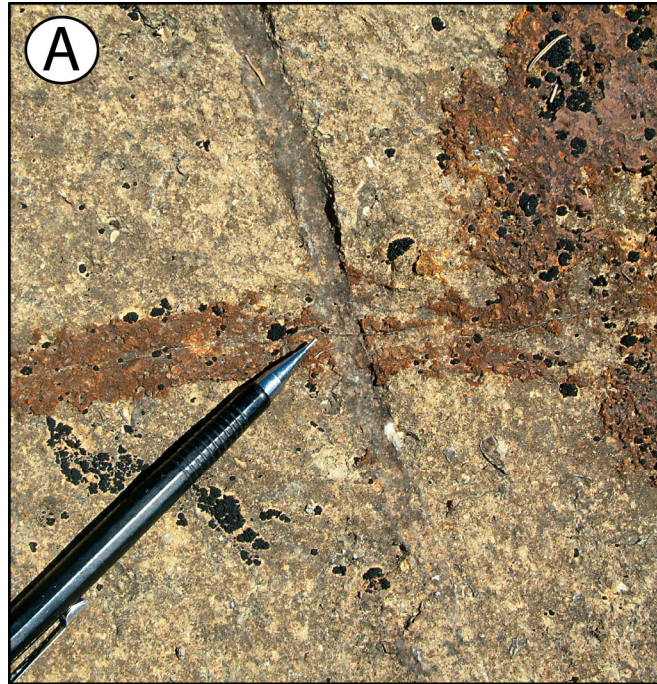


Figure 3.18 Secondary lise gang banding associated with a J5 joint. A) image, B) interpretive sketch. The sub-millimeter thick calcite(?) fill of the J5 joints cross cuts the calcite fill of a J2 joint indicating that the J5 joint cross cuts, and thus post-dates the J2 joint. Lise gang banding appears to be limited to a 2-3 cm thick zone adjacent to the J5 joints, with no lise gang banding associated with the J2 joints. Lise gang banding is probably a result of re-mobilization of oxidized iron in wall rock “haloes” like those shown in Fig. 3.17.

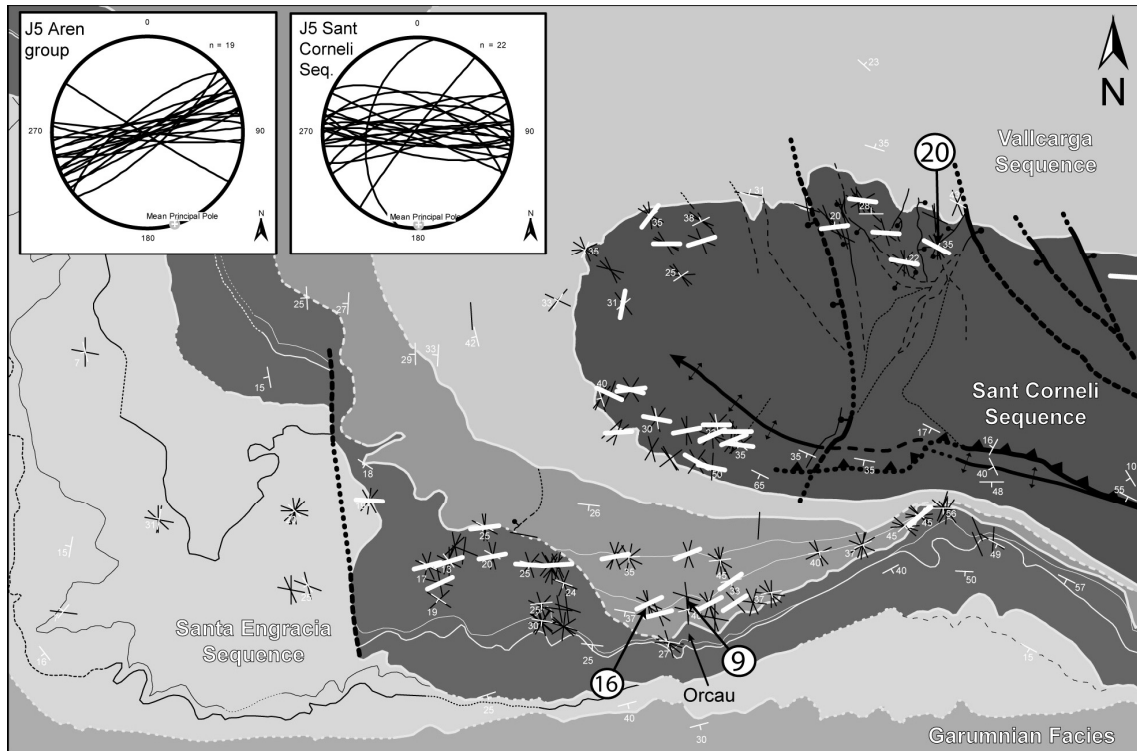


Figure 3.19 Map of J5 strikes in the study area. White ticks indicate the strikes of J5 joints rotated to bed-horizontal. Black ticks indicate the strikes of all other joint sets rotated to horizontal about the fold axis. Inset stereonet shows planes of J5 joints in the Aren Group and Sant Corneli sequence rotated to bed-horizontal. Circles with arrows indicate the numbers of figures showing J5 joints.

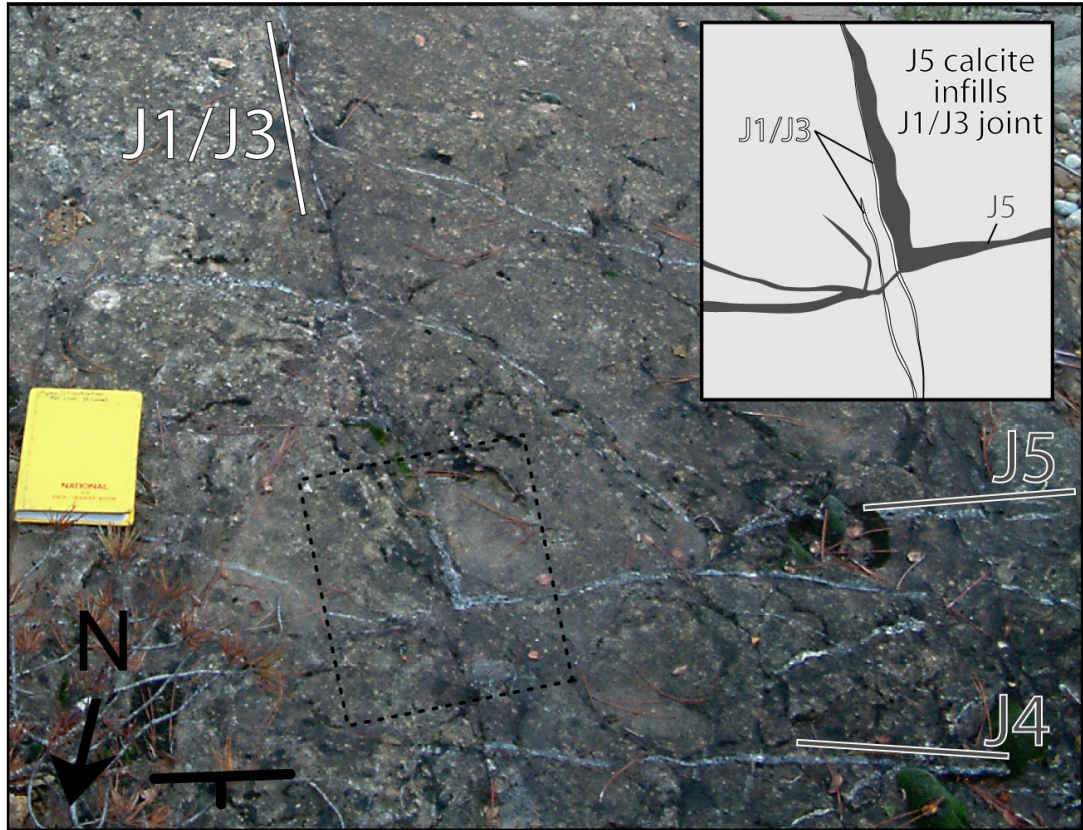


Figure 3.20 Photograph of an oblique cross section through bedding showing the relationship of J1/J3 to J4/J5 joints in the backlimb of the Sant Corneli Sequence. Inset sketch represents the area outlined by the dotted box in the image. The calcite fill of J4 and J5 joints infiltrate a previously filled J1/J3 joint. The inset sketch shows a J5 joint that terminates abruptly against the J1/J3 joint. The fill of the J5 joint heals the J1/J3 joint. A similar case is shown near the top of the image where a J4 joint curves into the J1/J3 joint. J4 and J5 joints appear to share calcite fill here, and locally stain the wall rock of all three joint sets with hematite/geothite cements.

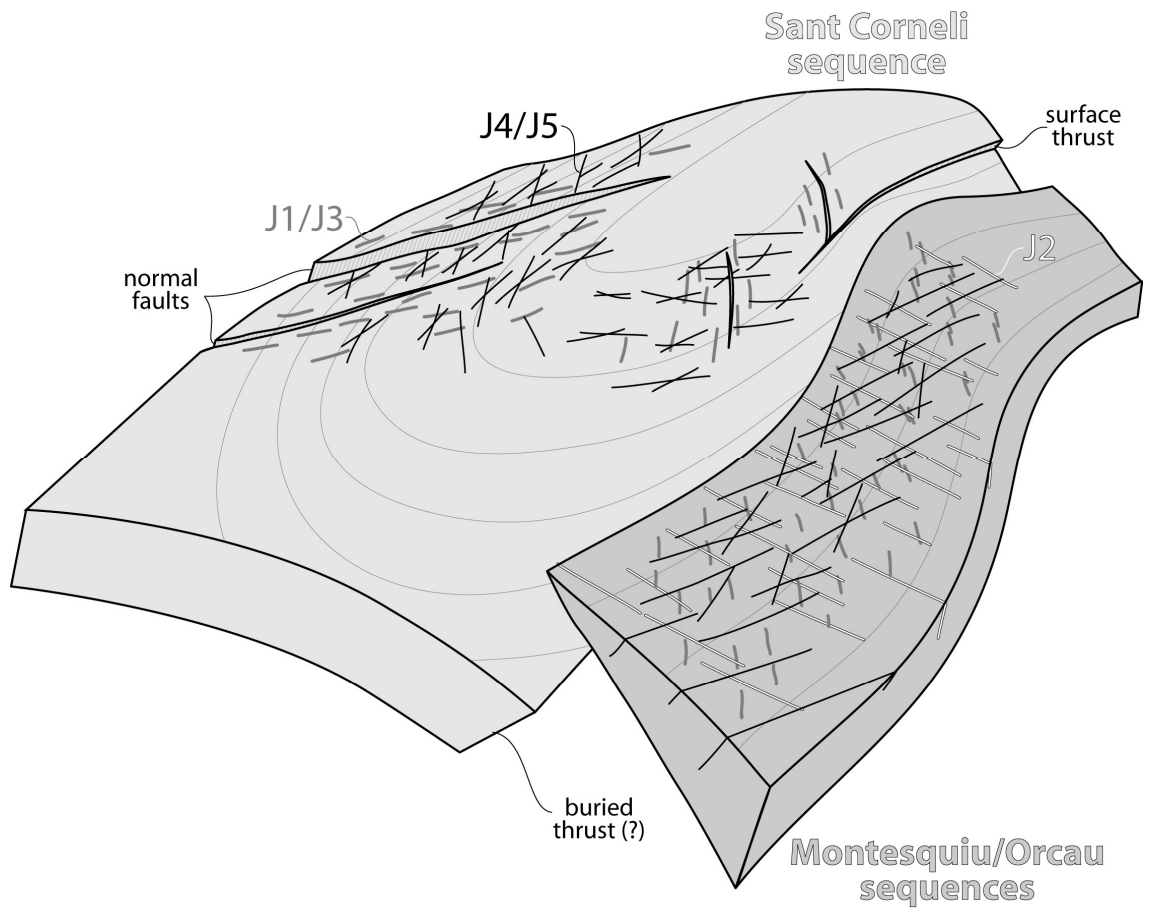


Figure 3.21 Simplified interpretive sketch of joints at Sant Corneli anticline showing the orientations of joints with respect to bedding and structural position.

CHAPTER 4

VALIDATION OF STRUCTURAL RESTORATION TECHNIQUES USING INCREMENTAL RESTORATION OF A WELL CONSTRAINED RESERVOIR ANALOG: SANT CORNELI ANTILCINE (SPAIN)

4.1 Introduction

Faults and fractures commonly serve as fluid flow pathways in otherwise low permeability aquifers and hydrocarbon reservoirs (the term “fracture” hereafter includes joints, shear fractures, and faults) (Hanks 1997, Hanks et al. 2006, Kirkwood 2000, Leftcariu 2005, Nelson 1985). Within fault-cored folds, fracturing and folding occur continuously through time such that fractures observed in the field or subsurface may have been associated with deformation events that occurred before, during and after folding (e.g. Hanks 1997). Thus, unraveling complex structural histories and interpreting the timing and origin of different fracturing events helps minimize uncertainty and manage risk associated with subsurface reservoirs and aquifers.

Conceptual and quantitative predictions of fracture patterns on three-dimensional folds have previously been based on fold curvature (e.g. Fischer & Wilkerson 2000, Hennings et al. 2000, Stearns 1967, Stearns & Friedman 1972). Plate bending theory predicts that the maximum curvature directions parallel the maximum principal (tensional) stress direction, which can be used to predict the orientation of joints and faults (Szilard 1974). However, curvature predictions based only on the final fold shape may not adequately represent stress patterns throughout the entire fold development because maximum curvature directions on transitional fold shapes may be different from

those on the final fold. This may explain why fractures observed on folds often do not match the fold curvature predictions (Cruikshank 1991, Davis 2004, Engelder 1997, Hennings et al. 2000). Thus, complete fracture network predictions require constraining the intervening steps of fold evolution between the initially un-deformed layers and the final fold shape.

Fault-cored folds with syn-tectonic strata have been used to constrain fold kinematics because each syn-tectonic horizon records a snapshot during the growth of the fold (e.g. Bernal & Hardy 2002, Ford et al. 1997, Novoa et al. 2000, Poblet et al. 1998, Salvini & Storti 2002, Vergés et al. 1996). Because syn-tectonic strata record incremental steps during fold evolution, they can constrain many aspects of fold kinematics such as limb rotation, hinge migration, and lateral fold propagation (e.g. Bernal & Hardy 2002, Ford et al. 1997). While syn-tectonic strata have been used widely to constrain fold growth, few studies have linked fold evolution constrained by syn-tectonic strata to fracturing (Nigro & Renda 2004, Chapter 3 of this thesis).

Most natural fault-cored folds lack direct evidence for transitional fold shapes that may be used to predict fracture patterns. Consequently, geologists have developed geometric and geomechanical restoration and forward modeling techniques to infer transitional fold shapes based on observed fold geometries (e.g. Erslev 1991, Griffiths et al. 2002, Maerten 1999, Moretti et al. 2006, Poblet & McClay 1996, Rouby et al. 2000, Suppe 1983, Suppe & Medwedeff 1990, Thibert et al. 2005). Most geometric restoration algorithms are virtually instantaneous in terms of computation time, but assume uniform transport direction for kinematic unfolding of folded strata. These restorations, sometimes termed, “pseudo three-dimensional” are conceptually similar to restoring serial

cross sections parallel to the fold axis (e.g. Griffiths et al. 2002). Chapter 2 of this thesis examines three-dimensional mechanical models of non-cylindrical fault-cored folds and confirms that two-dimensional plane strain restorations are not valid in many parts of plunging folds. These findings suggest that the calculation of stresses associated with the folding or unfolding of a plunging fold requires a fully three-dimensional approach that permits variations in transport directions around non-cylindrical folds(Rouby et al. 2000).

Improvements in computational capacity have allowed for increasingly complex structural modeling, including geomechanically based restorations of complex three-dimensional volumes with and without incorporating fault slip. Unlike many purely geometric algorithms, geomechanically based restorations allow for heterogeneous three-dimensional strain (non-plane strain), are based in the physical laws of motion, and can potentially model lithologic variation between strata. Though the availability and functionality of three-dimensional restoration techniques has increased significantly, few have been rigorously tested in terms of predicting fracture orientations based on fault or fold geometries (Bai et al. 2002).

In this chapter, I use three-dimensional restorations of Sant Corneli anticline in the Spanish Pyrenees to test the fracture prediction capability of a geomechanical restoration algorithm in fold and thrust belts. Sant Corneli anticline is a plunging thrust-related anticline, cored by fractured carbonates and overlain by a sequence of syn-tectonic sediments. Reconstruction of the three-dimensional architecture of the syn-tectonic strata above and below the topography provides a template for incrementally unfolding Sant Corneli anticline using geomechanical restoration techniques. To incrementally restore Sant Corneli anticline, I use a geomechanical solver that performs

full volumetric geomechanical finite element solutions (Dyne3D, www.igeoss.com).

Dyne3D is a commercial software package used in the petroleum industry that unfolds geologic strata and restores displacement on faults while minimizing strain within the surrounding rocks (Maerten & Maerten 2006).

To evaluate the stress/strain predictions produced by the restoration, I utilize the stress/strain history recorded by faults and joints at Sant Corneli anticline. Structural restoration provides the link between fold evolution and fracturing because unfolding and forward modeling of unfolded strata can be used to predict the orientation of faults and fractures. The goal of the restoration presented in this chapter is to predict the generalized strain patterns associated with fault-related folding within Sant Corneli anticline at different stages of deformation. Cross cutting relationships of joints suggest the following sequence of fractures associated with folding:

- Fracturing associated with early development of the anticline was characterized by approximately radial joints and faults (J1/J3, Fig. 3.11), possibly including faulting events as early as Montesquiu time (Fig. 3.5A).
- A N-NW striking jointing event that may be associated with lateral propagation and gravity faulting of the Orcau-Vell and Montesquiu sequences that only affects the Montesquiu and Orcau-Vell sequences (J2, Fig. 3.9).
- Pervasive and through-going joint sets that are closer to bed strike than previous joint sets (J4/J5, Figs. 3.13, 3.14) are interpreted to have formed during the latest stages of fold growth during or after deposition of the Garumnian sequence. This interpretation is based on the observation of significant iron oxidation that is probably associated with subaerial exposure.

Sant Corneli anticline offers a unique opportunity to evaluate the efficacy of structural restoration in predicting sub-seismic scale fractures and faults because each fracturing event is temporally constrained by relationships to growth strata that constrain fold evolution. Thus, the strains predicted by the restorations are compared to the fracture sets that formed over the corresponding time intervals. In this manner, I can directly evaluate the efficacy of the restoration in predicting fracture patterns.

4.2 Reconstruction of Sant Corneli anticline

Reconstructing geologic surfaces in three dimensions is useful as a descriptive exercise, an interpretive exercise, and as a template for structural restorations. Fernandez (2004) and Dhont and others (2005) describe techniques for reconstructing and projecting geologic surfaces using three dimensional traces of mapped contacts and dip data measured in the field. Such techniques are an improvement over surfaces created using serial cross sections because they continuously honor field data in three dimensions without creating artifacts by projecting geologic data onto cross sections and interpolating between them. Cross section based reconstructions are also more difficult in non-cylindrical folds where projection of geologic data onto cross sections may be complicated by changing orientations of the fold axis and bed strikes.

Sant Corneli anticline is well suited to three-dimensional reconstructions due to its excellent three-dimensional exposures. Guillaume and others (2008) reconstructed the subsurface geometry of the upper growth strata units (Orcau-Vell and Santa Engracia sequences) in three dimensions using techniques developed by Dhont and others (2005). In this study, I build upon and integrate the surfaces constructed by Guillaume and others

(2008) as well as published cross-sections to reconstruct the subsurface and eroded portions of Sant Corneli anticline, including the Montesquiú, Vallcarga, and Sant Corneli sequences. Reconstructions utilized similar techniques to Fernandez (2004) and Dhont and others (2005), and relied heavily on the reconstruction and projection techniques in Midland Valley Exploration's 3DMove software (www.mve.com). A description of each surface in the model and their significant constraints are described below and in Figs. 4.1-4.8.

- The topographic exposure of the Sant Corneli sequence outlines the shape of Sant Corneli anticline such that up- and down-dip projection of the outcrop trace, as well as stratigraphic projection of the eroded portions of the anticline constrains the reconstruction of the unit (Fig. 4.1). The top of the Sant Corneli sequence is locally offset by fold-axis perpendicular normal faults, though few of the larger faults are well exposed at the surface. The orientations of such faults are estimated using the orientations of secondary normal faults as well as the fault orientations in map view (e.g. Figs. 3.4, 3.7).
- Though Sant Corneli anticline is interpreted to be a fault-cored fold that reactivates a lower Cretaceous extensional fault (Bond & McClay 1995, García-Senz 2002), the subsurface geometry of the thrust is poorly constrained. The depth of the thrust beneath the backlimb of Sant Corneli anticline is constrained by the Sant Corneli 1 well, although various interpretations have been proposed for the cross sectional geometry of the anticline (interpretations are summarized in Section 3.4 and shown in Figs. 3.6, 4.2A). To construct the fault geometry in three dimensions, I use the

most recent cross section interpretation published by Garcia-Senz (2002, redrafted in Fig. 3.6C). The two dimensional fault geometry is projected E-W along strike to mimic the E-W strike of both the Sant Corneli anticline and the Boixols thrust to the east. Fault displacement is assumed to decrease toward the west, consistent with the abrupt termination of Sant Corneli anticline (Fig. 4.2B). For simplicity, normal faults within the lower Cretaceous-Triassic strata were ignored (Fig. 3.6).

- The depth or geometry of the Sant Corneli sequence in the footwall are poorly constrained south of the Sant Corneli 1 well. The Sant Corneli 1 well intersects an overturned section of lower Cretaceous strata at a depth of 2900 meters, which is generally interpreted to be a thrust slice (Fig. 3.6).

Therefore, the top of the Sant Corneli sequence, or rocks temporally equivalent to them, is probably at or below that depth (Fig. 3.6, Déramond et al. 1993, García-Senz 2002, Specht et al. 1991, Vergés 1993). The closest possible constraint on the depth of the Sant Corneli sequence to the south comes from the Isona 1 Well, which is 10 km to the southeast. In the model, the top of the Sant Corneli sequence in the footwall of the anticline is projected to the west with a regional dip of approximately 7° using the top of the correlative Cenomanian-Santonian calcite units in Garcia-Senz's (2002, Fig. 3.21b) cross section (Fig. 4.2). Because of the relatively poor constraint on this unit in the subsurface, the geometry should be considered schematic.

- The top of the Vallcarga sequence is constrained by projection of mapped contacts according to measured dips above and below the surface (Fig. 4.3).

Surface mapping and borehole data indicate that Vallcarga thickens dramatically to the northwest to a thickness of up to 1500 meters northwest of the study area (Simó 1989). To project the Vallcarga above the surface, the thickening profile formed by the topographic cross section (Fig. 3.4) is projected northeastward while honoring the dip discrepancy between the Sant Corneli sequence and the underlying Vallcarga sequence.

- Two shallow marine shoreface sandstones within the Montesquiú sequence form prominent hogbacks in the southern part of the study area. The intersection of mapped contacts with digital elevation models (Dhont et al. 2005, Fernandez Bellon 2004) constrains the dip and curvature of these surfaces in an E-W sense (Figs. 3.4, 4.4). These units are interpreted to have thinned gradually onto the Sant Corneli paleo-high to the northeast, with shorelines curving northwestward. These layers were reconstructed by maintaining and projecting the northwestward thickening profile observed in a cross section created from the topography over the Vallcarga sequence.
- A major unconformity separates the Montesquiú and Orcau-Vell depositional sequences and removes significant portions of the Montesquiú and Vallcarga sequences (Fig. 4.5). Guillaume and others (2008) reconstructed the unconformity at the base of the Orcau-Vell sequence in the subsurface, which is projected across across the top of the anticline in this reconstruction. In the northeastern end of the study area, the Eocene-Oligocene conglomerates lie directly on the Vallcarga sequence, thus constraining the upper limit of the unconformity to the northeast. The basal Orcau-Vell unconformity may be

cross cut by younger unconformities such as those at the bases of the Santa Engracia sequence and/or Garumnian sequences, however, for simplicity the majority of erosion is assumed to have taken place prior to deposition of the Orcau-Vell sequence. This interpretation is supported by the significantly shallower dips in the Orcau-Vell sequence as compared to the Montesquiu sequence, which probably indicates significant uplift and erosion during earliest Orcau-Vell time (Fig. 3.5B).

- The subsurface geometries of the Orcau-Vell and Santa Engracia sequences, including a N-NW striking gravity fault have been reconstructed by Guillaume and others (2008, Fig. 4.6). The Orcau-Vell and the lower portions of the Santa Engracia sequence are approximately parallel to the underlying unconformity, but gradually thin to the northeast and thicken to the southwest where the gravity fault created significant accommodation space (Fig. 4.6B). Guillaume and others (2008) interpreted that at depth, the gravity fault soles into a detachment 1000 m below the top of the Transgressive Systems Tract of the Santa Engracia Sequence, possibly corresponding with the top of the top of the Vallcarga Sequence in the model shown. Because the modeling in this study does not directly address the gravity faulting, the gravity fault is projected to depth, offsetting the top of the Vallcarga Sequence and ignoring the interpreted listric curvature of the fault.
- Three surfaces within the Santa Engracia sequence are reconstructed (Fig. 4.7). The most significant discrepancy in dip within the Santa Engracia sequence is between the transgressive systems tract and the highstand systems

tract (green and translucent yellow surfaces in Fig. 4.7). Up-dip projection of the highstand systems tract (HST) intersects many of the underlying surfaces, possibly indicating non-deposition and/or some erosion of the top of the anticline during this time. Because the highstand systems tract indicates a time of relatively high sea level when significant erosion is less likely, this surface is truncated against the older units (Fig. 4.7A). However, a dip-projected geometry of the HST has also been reconstructed below the older units, which is used to constrain aspects of the structural restoration.

- The Garumnian sequence is only exposed in the forelimb of the anticline and was deposited after much of the folding of Sant Corneli anticline. As such, the top of the Garumnian sequence is not reconstructed.

The reconstruction presented in Figs. 4.1-4.7 is interpretive in that surfaces must be extrapolated outside of the geometry constrained at the subsurface using assumptions based on the sedimentary and geometric relationships between strata (Fig. 4.8). As such, decisions made at each step of the reconstruction affect the later steps. Specifically, the reconstruction of each successive unit is based, in part, on the thickness and dip of the underlying strata such that model errors can be propagated up- or down-section. The largest uncertainty in this reconstruction is due to the uncertainty involved with projecting unconformity surfaces, whose geometries may be irregular and potentially have eroded multiple square kilometers of rock. However, the relatively simple and plausible assumptions that sedimentary strata in the anticline 1) should be concave, and 2) should bend in an approximately smooth shape around the anticline allows for

projection and reconstruction of eroded strata above unconformity surfaces as shown in Figs. 4.3 and 4.4. For these reasons, the reconstruction offers an internally consistent and plausible approximation to the surface and subsurface geology.

4.3 Restoration of Sant Corneli anticline

The following sections describe how the reconstruction of Sant Corneli anticline serves as a template for sequentially restoring two horizons in the growth strata that constrain the late stages of folding. The first section describes the construction of two template horizons and the following sections describe the restoration of each step in detail.

4.3.1 Construction of initial restoration template surfaces

Erosion of significant portions of the anticline (Fig. 4.5) limits the accuracy of the structural restoration because eroded surfaces must be reconstructed, sometimes without adequate constraints on their geometry. Thus, this restoration is limited to unfolding the Santa Engracia sequence, whose surfaces are relatively well constrained and where relatively little erosion has occurred. Two horizons are successively restored to horizontal. First, the highstand systems tract (HST) of the Santa Engracia sequence (translucent yellow surface in Fig. 4.7) represents the youngest reconstructed horizon before deposition of the Garumnian sequence, and therefore probably represents the last stages of Cretaceous folding of Sant Corneli anticline. The HST has a large angular discordance with the underlying transgressive systems tract (TST) of the Santa Engracia sequence, indicating a significant amount of folding during deposition of the HST. Unfortunately, the HST of the Santa Engracia sequence thins to zero thickness near the

culmination of Sant Corneli anticline and does not cover the top of the underlying TST. However, volumetric restoration requires full coverage of all strata in the model in order for a given stratigraphic unit to constrain the deformation behavior of underlying units.

In order to use the shape of the HST of the Santa Engracia sequence to govern the restoration of the underlying units, the HST surface must be projected above its present day geometry to create artificial volumetric space between the top of the unit and the older strata (Fig. 4.9A). The parallel projection (projection vectors normal to the surface) requires 330 meters of additional sediment to fully cover the older stratigraphic units and allow for creation of finite element volumes. Geologically, the projection is similar to creating more accommodation space and adding some volume of sediment above a given surface. In this case, the up-dip projection of the HST Santa Engracia is relatively well constrained by the orientation of the top of the unit to the south and west.

The up-dip projection of the TST of the Santa Engracia indicates that the unit onlaps the underlying Orcau-Vell sequence and thins gradually to zero thickness. The whole sedimentary package thins to zero thickness at the unconformable contact at the northeastern boundary of the study area. A similar methodology of parallel projection is used to create a restoration surface representing the top of the TST. In this case, projection vectors are computed from the top of the TST of the Santa Engracia sequence and the HST of the Orcau-Vell sequence (Fig. 4.9B). For the purposes of this restoration, 50 meters of additional thickness is added to allow for the creation of a reasonable volumetric thickness of the strata above the underlying strata.

4.3.2 Restoration step 1

4.3.2.1 Finite element meshing

To create finite element volumes for restoration the reconstructed model must be simplified to allow for reasonable tetrahedral mesh sizes which reduce computation time and computer memory requirements. To reduce the complexity of the finite element mesh, three geologic horizons are removed prior to mesh generation: the top of the deltaic units in the Santa Engracia sequence (Fig. 4.7), the lowstand systems tracts of the Santa Engracia and Orcau-Vell sequences (Figs. 4.7 and 4.8), and the Sant Corneli sequence in the footwall of the Boixols thrust (Fig. 4.2).

The surfaces used for finite element meshing of the first restoration step are shown in figure 4.10A. Because the purposes of this restoration are to mimic the large scale strain field associated with fault related folding, neither the gravity fault nor normal faults in the Sant Corneli sequence are included as discrete discontinuities in the tetrahedral mesh. Surfaces that are cross cut by the faults are re-tessellated across the fault boundaries. In this manner, the displacement associated with such faults is partially represented by the geometry of the layers, which retain the offset of the fault, but do not include the fault as a discrete boundary. The Boixols thrust, however, is included as a discrete fault discontinuity because it is likely that the fault significantly influenced the stress field during folding.

The volumetric mesh generated by Dynel3d for the first step of the restoration is shown in Fig. 4.10B. The average mesh size is set to approximately 300 meters, which captures the majority of the roughly kilometer scale surface undulations in the

reconstruction and approximates the scale over which fracture measurements are generalized. Larger mesh sizes capture the approximate bulk strain, but do not capture smaller scale changes in strain patterns. Mesh sizes below 300 meters, while preferred, led to program instability during rendering.

4.3.2.2 Boundary conditions

In the restoration, the uppermost horizon is constrained to a horizontal plane. All outer boundaries of the model are free to move in any direction. Faults and sliding bedding horizons have no traction and can therefore slide freely in any direction, but must remain in contact with one another without interpenetration. Because the model is artificially truncated along the eastern boundary, a vertical, N-S striking fault is included to simulate a sliding boundary condition at the eastern end of the field area. The fault is perpendicular to the fold axis, and therefore constrains restoration vectors to be approximately perpendicular to the fold axis (e.g. Fig. 2.5). Volumes are assigned isotropic elastic properties, which are described in Table 4.1. In general, the Aren Group is assigned the elastic properties for sandstone, the Vallcarga sequence is assigned the elastic properties of shale, and the Sant Corneli sequence is assigned the elastic properties for limestone.

Two boundary conditions on the reconstructed surfaces are presented here to explore the effect of bed slip on fracturing in the restoration. In the first case, no horizons are allowed to slide (no flexural slip) and in the second case, all horizons with the exception of the basal Orcau-Vell unconformity are allowed to slide freely (flexural slip). Slip on the unconformity surface is assumed to be unlikely because where

observed, the unconformity surface is not a discrete, planar discontinuity that would facilitate slip. In both cases, the Boixols thrust and the N-S striking, vertical fault at the eastern boundary are allowed to slip freely. No boundary condition is imposed on the base of the model.

4.3.2.3 Geometry of the restored strata

The results of the two restorations are shown in Figs. 4.11 and 4.12. Restoring the top of the Santa Engracia sequence with no flexural slip produces a relatively uniform unfolding pattern, with approximately 780 meters of shortening at the base of the model to the east, decreasing to approximately 70 meters of shortening at the base of the model to the west. Because there is no slip, the shear gradient along the originally vertical boundaries is uniform. Restoring the corresponding model with flexural slip produces remarkably similar overall geometries to a first order, although the shear gradient clearly differs between the two models as indicated by the offsets along sliding bedding interfaces in Figs. 4.11. Significant top-to-north offset of the upper Santa Engracia sequence is a consequence of the relatively large strain in this restoration step, combined with the traction-free boundary condition on the sliding bed surfaces. Despite the offset of the upper Santa Engracia sequence, the geometry of the underlying Santa Engracia and Orcau-Vell sequences in their restored state is remarkably similar in both models (Fig. 4.12).

4.3.2.4 Fault and fracture prediction

To predict fracture patterns based on the structural restoration, strains are computed in a forward sense, with the restored state representing the un-strained state,

and the deformed state representing the deformed state. Fig. 4.13 shows a comparison between the predicted joint strikes in both models and the observed field data. Because opening mode joints and normal faults would likely have similar strike, the joint strike maps can also be used to infer normal fault strike. In general, joint and fault strikes predicted by both the flexural and non flexural slip boundary conditions are very similar, with the exception of some areas near the model boundaries and along the eastern axis of the anticline.

To a first order, the strain patterns predicted by both restorations are consistent with many of the map scale extensional faults in the study area. Predicted strain patterns match the NE strike of normal faults in the eastern backlimb of the Sant Corneli sequence, as well as the gradual rotation of normal fault strike toward N-NW striking normal faults in the backlimb near the nose of the anticline. N-NE striking faults in the forelimb are not predicted by the restoration at this stage of fold development, although relatively few N-NE striking faults are observed on the forelimb. Predicted strain patterns in the southwestern end of the study area are consistent with the strike of the N-NW striking gravity fault, although the predictions deviate from the model slightly in the hanging wall west of the fault.

Strain predictions in the first restoration step fail to reproduce patterns formed by the youngest joint sets in the study area. Predicted joint strikes in the Orcau-Vell and Montesquiú sequences are typically more N-S striking than the observed J4 and J5 joint sets, which generally strike NE and NW (Fig. 4.13A). In the Sant Corneli sequence, joint strikes predicted by both restorations are similar to the J4 joints on the south side of the fold nose and in the easternmost backlimb, however, the overall fit of all J4 joints is

relatively poor. J1/J3 joint sets show a similarly poor fit to the predicted joint strikes (Fig. 4.13B). J2 joints fit the predictions remarkably well, despite the interpretation that such joints formed in response to N-NW striking gravity faulting at the end of Orcau-Vell time.

4.3.3 Restoration step 2

The restored state of first restoration step serves as an input for the second restoration step. The upper Santa Engracia sequence is removed and the TST of the Santa Engracia and Orcau-Vell sequences are restored to horizontal. Because Dynel3d requires surfaces as input into the mesh creation workflow, the top and bottom surfaces of each volume are extracted from the volumetric meshes, and the same model is re-meshed to create new volumes. Model boundaries are also reset such that the deformed and now dipping boundaries from the previous restoration step are removed (Fig. 4.14). The mesh sizes, elastic properties, and model boundaries are similar to the first restoration step in all respects.

4.3.3.1 Geometry of the restored strata

The results of the second step in the restoration are shown in Figs. 4.15 and 4.16. In general, similar patterns of flexural slip are observed in the first and second flexural slip restorations. The most significant difference between the two restoration steps lies in the magnitude of strain accommodated, which is consistent with the unfolding of steeper limb dips in the first restoration step. Removing the restored TST Santa Engracia and Orcau-Vell sequences reveals the unconformity surface that erodes the Montesquiu and

Vallcarga sequences. Restoration of surfaces below the unconformity would require reconstruction of the eroded Montesquiú and Vallcarga sequences.

4.3.3.2 Fault and fracture prediction

Fracture predictions based on forward modeling the second restoration step to the folded state shown in Fig. 4.17. The predicted joint strike patterns are broadly similar to those in the first restoration step, and also mimic the strike of the map scale faults in the field area. Predicted joints in the second restoration step show more heterogeneity in local strike, especially in the flexural slip restoration. Predicted joint strikes in the flexural slip restoration also tend to be more similar to local bed strike, much like the J4 and J5 joint sets, and therefore offer a relatively good fit to those sets. With the exception of the Orcau-Vell sequence immediately east of the gravity fault, the flexural slip restoration also accurately represents jointing in the Aren Group. Conversely, the restoration with no flexural slip tends toward a NW striking joints, and therefore mimics joint strike patterns associated with the J2 set relatively well. Neither restoration mimics the radial pattern of the J1/J3 joints.

To further explore the relationship between joint predictions in the flexural slip model and the J4 and J5 joint sets, the joints predicted by the flexural restoration are grouped by stratigraphic sequence (Fig. 4.18). In the Sant Corneli sequence, the flexural slip restoration produces a remarkably good fit to both the J4 and J5 joint sets. The restoration predicts both joint sets, but each joint prediction comes from a different stratigraphic horizon that is above or below the sliding boundary at the top of the Sant Corneli sequence. For example, in the inset image in Fig. 4.18, the blue N-S striking

joint predictions come from the Vallcarga sequence, whereas the orange W-NW striking joints come from the top of the Sant Corneli sequence. The J5 joints (light green in the inset image in Fig. 4.18) correlate well with joint predictions from the underlying Sant Corneli sequence (orange). At the same location, J4 joints (red) correlate well with the joint predictions from the overlying Vallcarga sequence (light blue). J4 joints show the inverse relationship in the backlimb, correlating remarkably well with joint predictions from the underlying Sant Corneli sequence. The J5 joints in the backlimb have relatively irregular strike that does not correlate well with either unit.

4.3.4. Discussion

4.3.4.1 Restoration step 1

Restoration of the top of the HST of the Santa Engracia sequence represents the latest stages during the folding of Sant Corneli anticline. Relatively steep limb dips as compared to the underlying strata suggest that significant shortening occurred over a relatively short interval during the deposition of the HST of the Santa Engracia sequence. Predictions of fracture strike from both the flexural, and non flexural slip cases correlate relatively well with the patterns of map scale normal faults in the area, but offer relatively poor correlations with many of the observed fracture sets in the study area, especially the youngest joint sets. The better correlation with larger scale faults than smaller scale fractures suggests that the first restoration step has captured the relatively long lived strain associated with large scale deformation during the latest stages of folding, but may miss many of the subtleties of smaller scale fracturing. Modeling strains associated with

jointing may require interpolation of transitional stages of folding within the restoration because fractures generally form at low strains.

Predictions of fracture strike in the first restoration show a strong component of E-SE extension in the central southwestern part of the growth strata (indicated by NW striking joint predictions in Fig. 4.13). This trend is consistent with the strike of the gravity fault in the same area and the J2 joint set, which is interpreted to have formed in response to the same stress field. This result is especially abnormal considering that these structures were interpreted to have formed during the intermediate stages of folding during Orcau-Vell time, before deposition of the Santa Engracia sequence that has been restored in this step. The relatively good correlation between the predicted fracture strikes and the N-NW oriented structures may be a result of eliminating the fault in the restoration. Displacement associated with the gravity fault would likely affect the restoration, especially considering that the fault tip is eroded and lies immediately to the west of many of the fracture mapping sites (Fig. 4.13).

4.3.4.2 Restoration step 2

Restoration of the TST of the Santa Engracia and HST of the Orcau Vell sequences represents a relatively small increment of deformation as compared to the first restoration step. Limb rotations in the second stage are on the order of 5-15° in contrast with the 15-25° limb rotations associated with the first restoration step. Predictions of fracture strike in the second restoration step are significantly more heterogeneous than in the first, and match many of the joint sets relatively well. Fracture predictions from the non-flexural slip restoration in the second restoration step do not correlate well with J4

and J5 joint sets in the Aren Group, but match J4 joints in the Sant Corneli sequence almost exactly (Fig. 4.17A). Conversely, fracture predictions in the flexural slip restoration match J4 and J5 joints in both the Aren and Sant Corneli sequences relatively well if the distinction between the two joint sets is ignored. Treating the J4 and J5 joints as one set is reasonable because the two sets are usually found together, have iron mineralization, and are only distinguished based on their orientation with respect to bed strike. Thus, fracture predictions based on the flexural slip restoration are considered to be a better match to than the non-flexural slip restoration.

Fracture predictions from the flexural slip restoration differ significantly across the flexural slip boundaries because each unit acts as a single mechanical unit. For example, at the boundary between the Sant Corneli and Vallcarga sequences, fracture predictions are nearly orthogonal (Fig. 4.18). The Sant Corneli sequence immediately below the sliding bed contact experiences outer arc extension associated with fold axis perpendicular bending of the anticline. Bending strains in the Vallcarga sequence immediately above the sliding bed contact indicate nearly fold axis-orthogonal extension, probably associated with the uplift of the anticline. The fact the both the J4/J5 joints are almost perfectly modeled by this system is peculiar because both joint sets are observed at the top of the Sant Corneli sequence and not in the Vallcarga sequence. A more complex system of multiple bedding slip surfaces may act to discretize this effect within smaller mechanical units, much in the same way that displacement fields are discretized within mechanical units (Fig. 2.6).

4.4 Conclusions and implications for fracture prediction in fault related folds

To a first order, both restorations produce realistic results when modeling the overall strain patterns in Sant Corneli anticline. The good correlation between observed and predicted fault strikes in the first restoration suggests that geomechanical restoration is an effective tool for predicting secondary faulting associated with fault related folding, but may not capture the smaller scale fracturing when modeled strains are large.

Conversely, when strain is modeled over relatively short time intervals, the model accurately predicts the patterns of smaller scale jointing and faulting. Although the syn-tectonic stratigraphy limits the time intervals over which restorations can be performed at Sant Corneli anticline, the strain patterns can be associated with the appropriate scale of deformation.

The shape of the Sant Corneli sequence is not unusual among plunging fold terminations, however, the predicted fracture patterns in both restoration steps are extremely complex and deviate significantly from both conceptual models for fold growth (Stearns 1967, Stearns & Friedman 1972) and plate bending models (Fischer & Wilkerson 2000, Szilard 1974). This suggests that modeling fractures in fault related cannot be as simple as applying conceptual models, or applying conceptual understandings of more complex models. The geomechanical restorations presented in this chapter show significant sensitivity to flexural slip, especially when folding and faulting is modeled over relatively short increments as the second restoration shows. This suggests that joint prediction in fault cored folds must utilize incremental deformation to constrain transitional fold shapes to accurately predict fractures associated with folding.

4.5 Figures

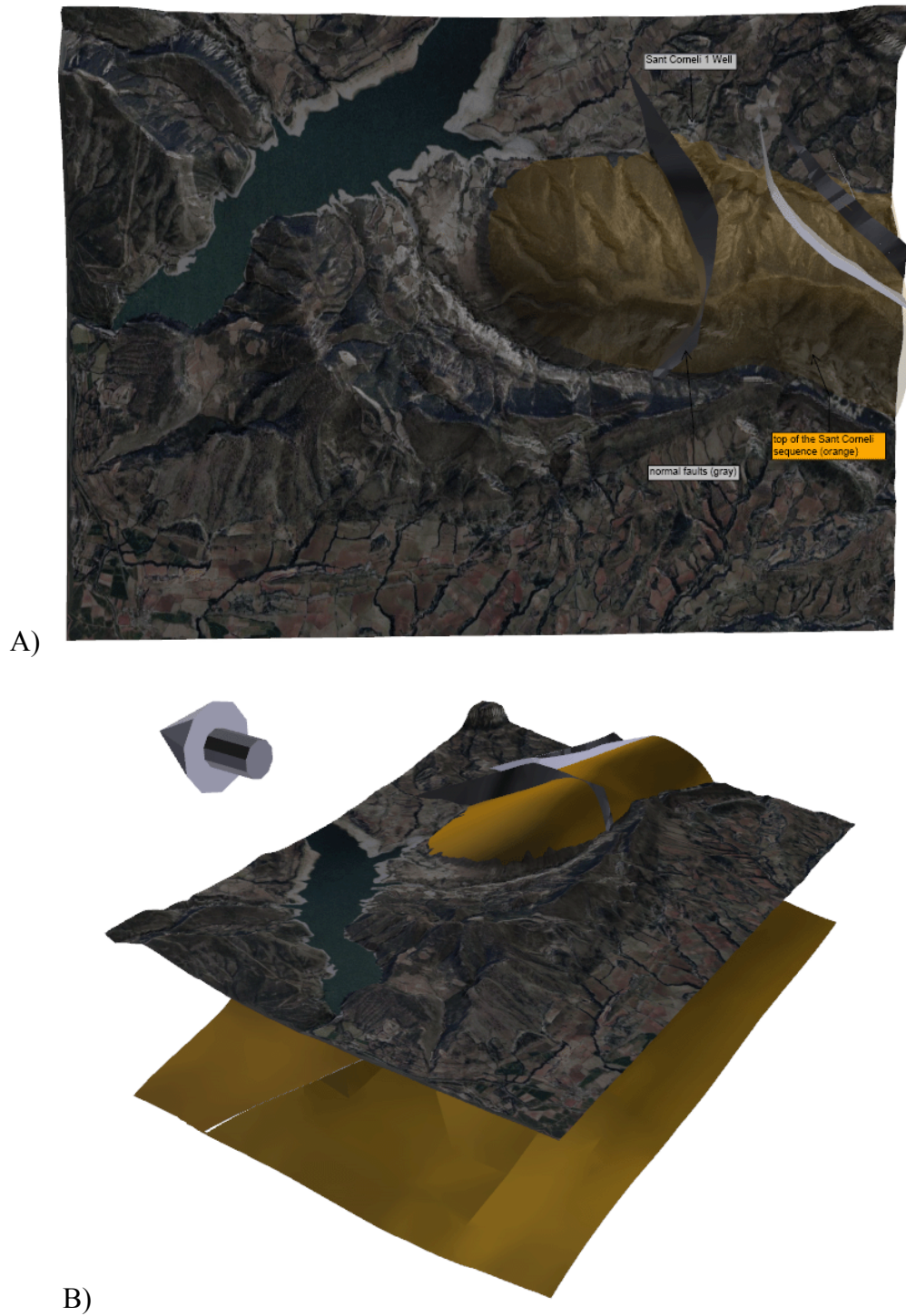
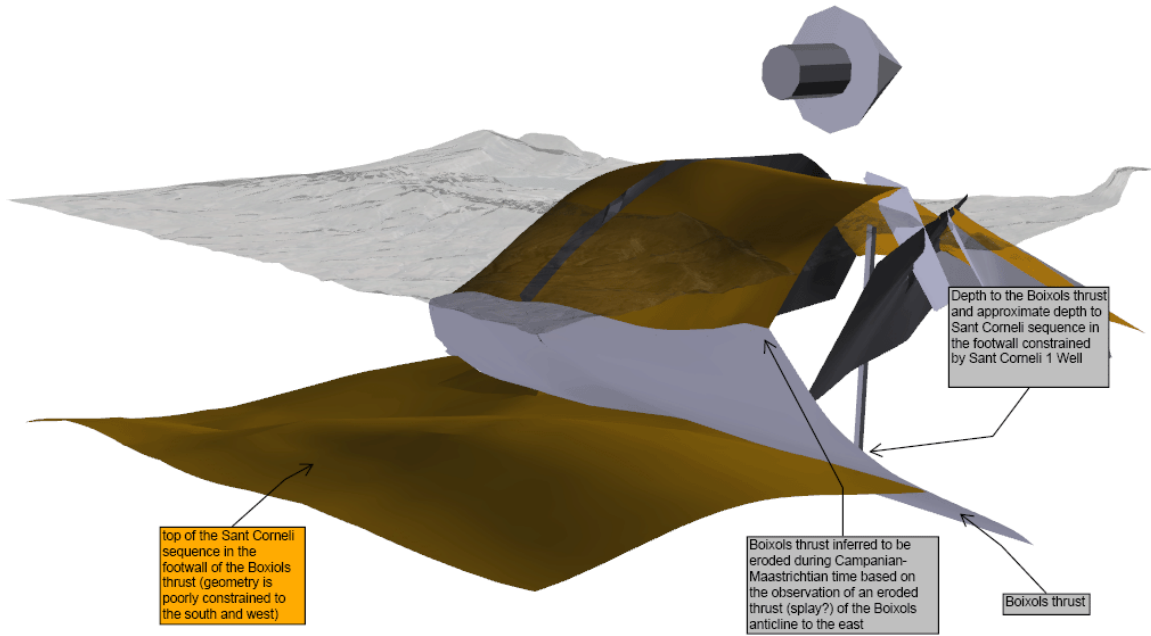


Figure 4.1 Sant Corneli sequence near the topographic surface. A) map view, B) NE view.

A)



B)

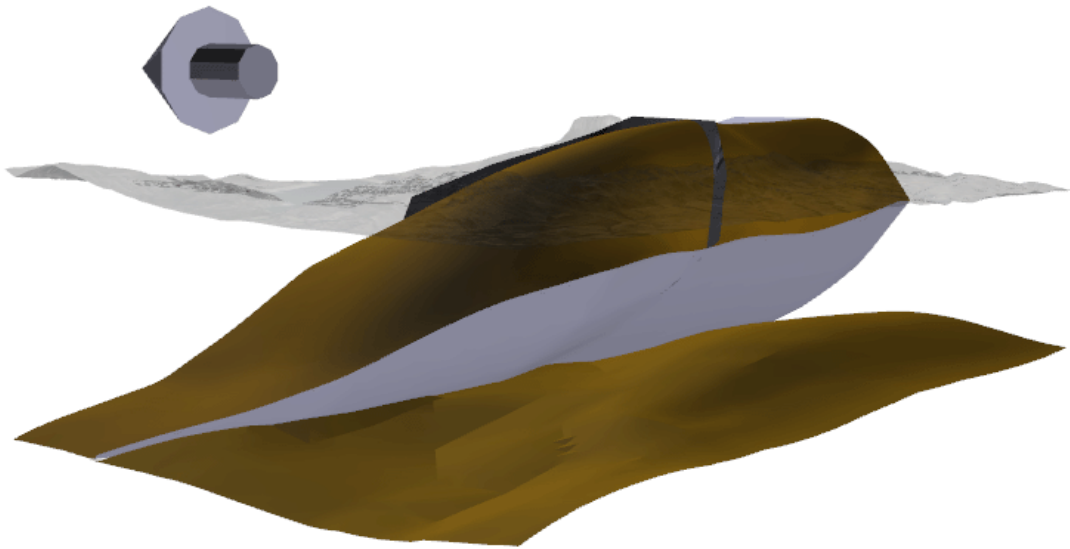
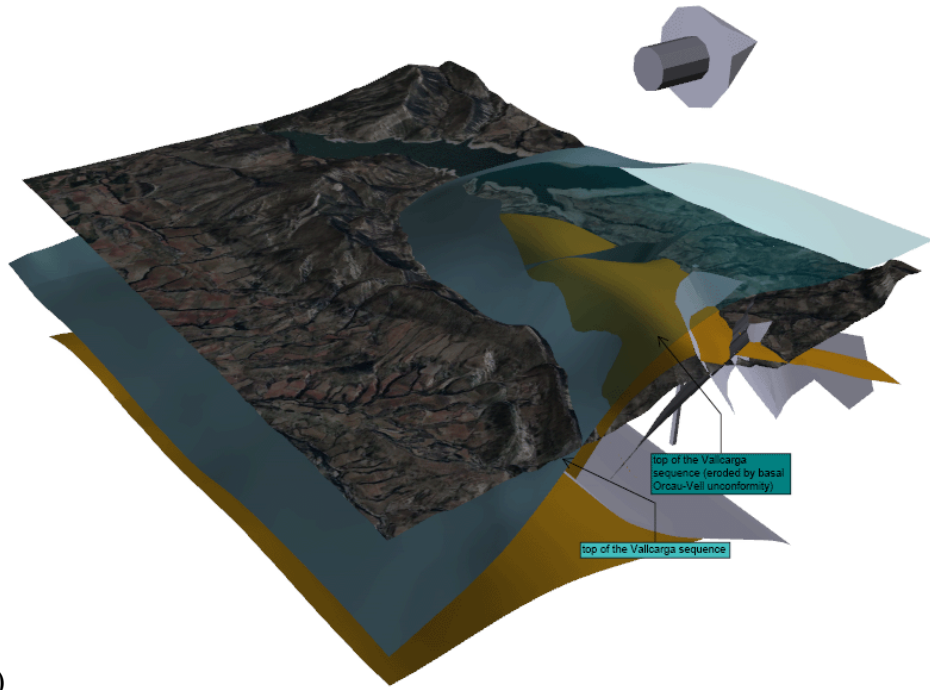
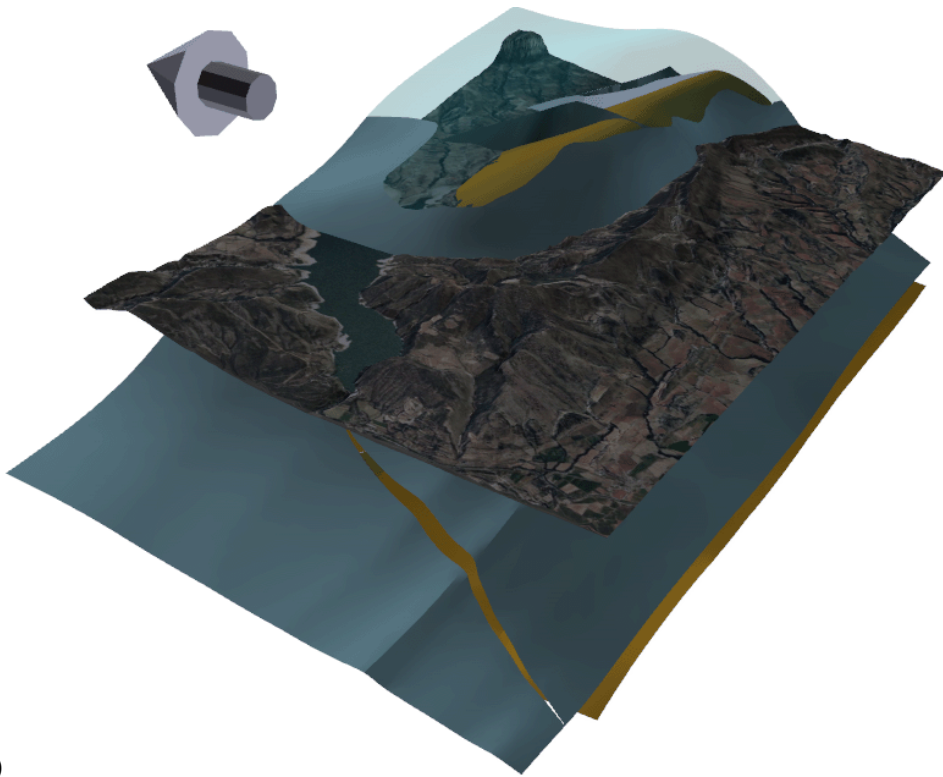


Figure 4.2 Sant Corneli sequence at depth. A) NW view, B) NE view.

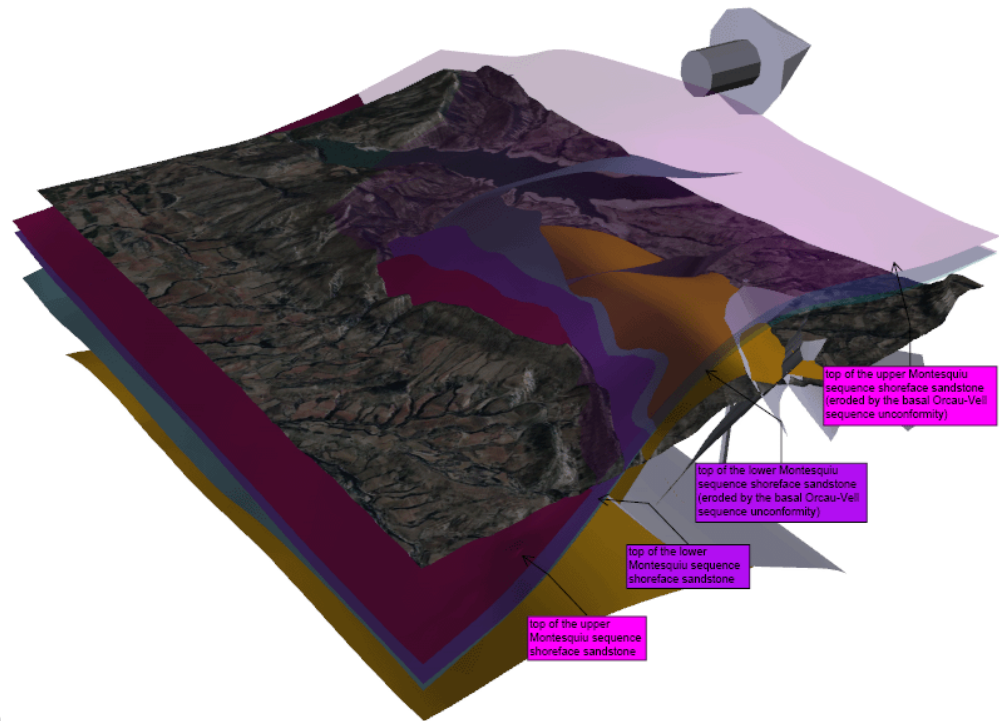


A)

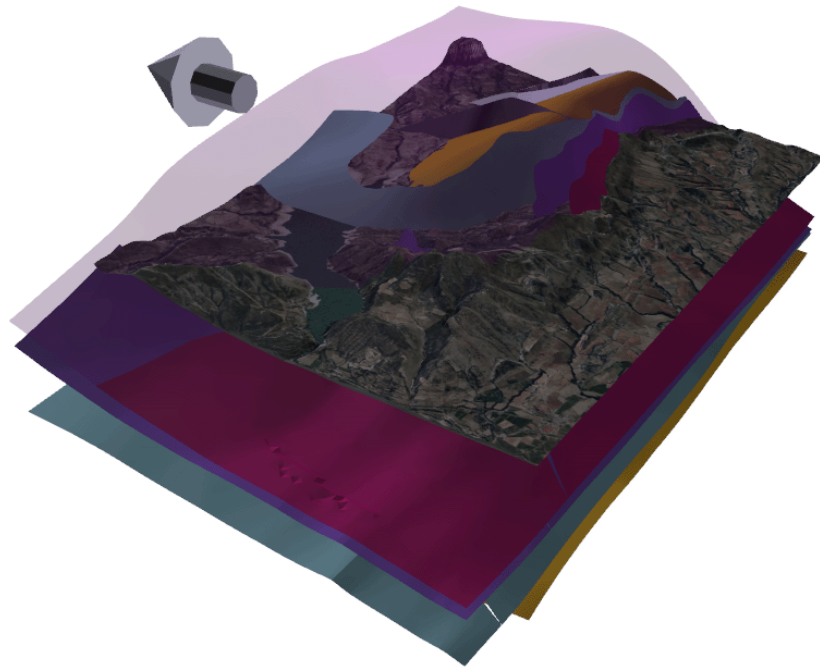


B)

Figure 4.3 Vallcarga sequence. A) NW view, B) NE view.

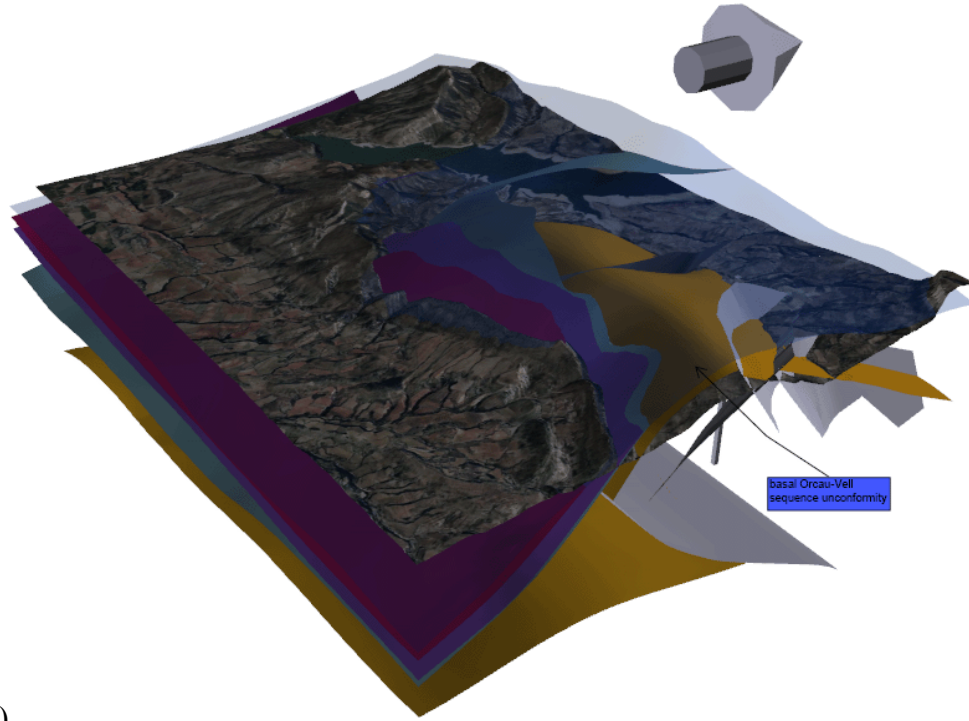


A)

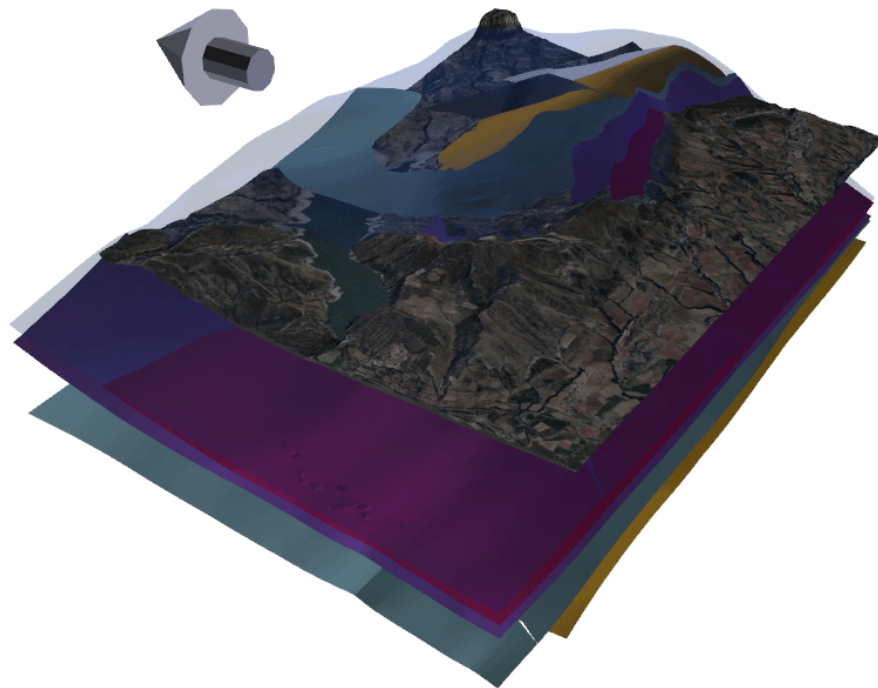


B)

Figure 4.4 Montesquiu sequence. A) NW view, B) NE view.



A)



B)

Figure 4.5 Orcau-Vell unconformity. A) NW view, B) NE view.

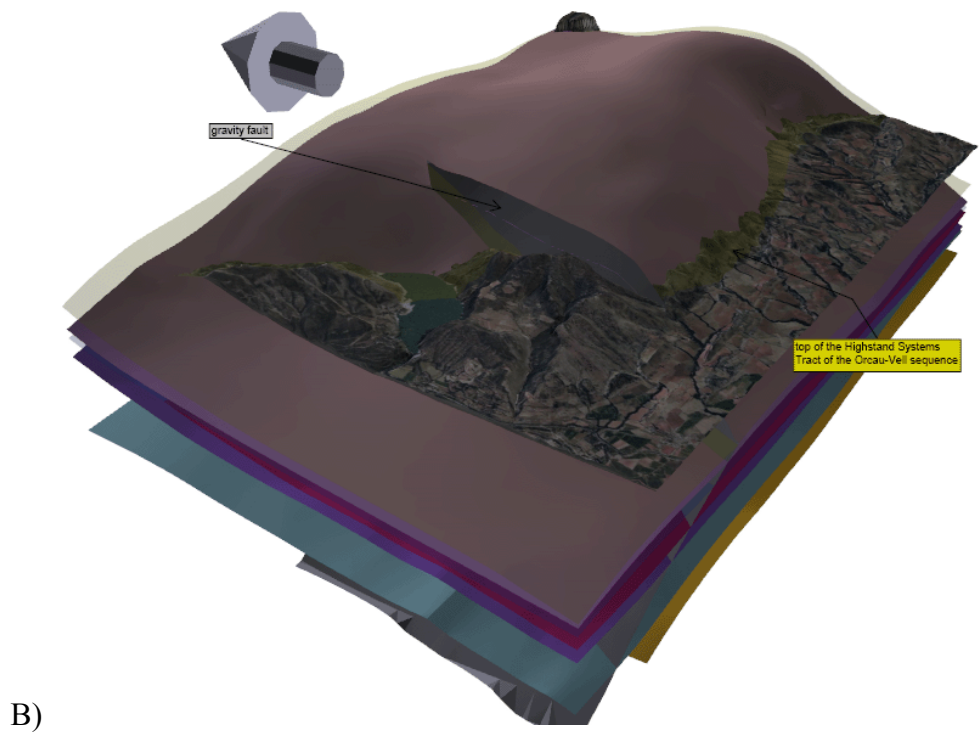
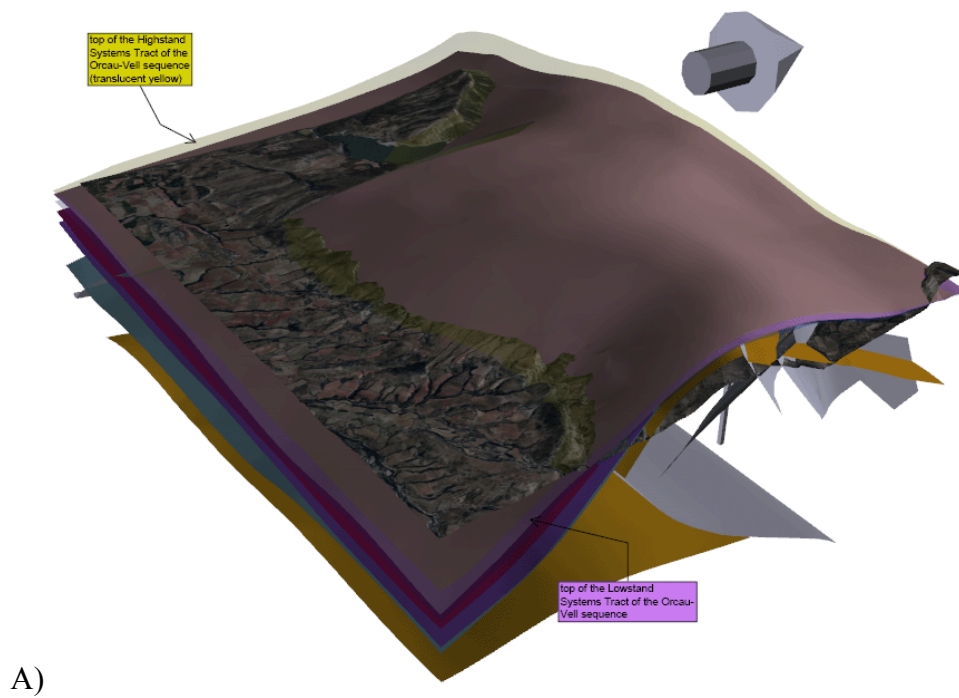
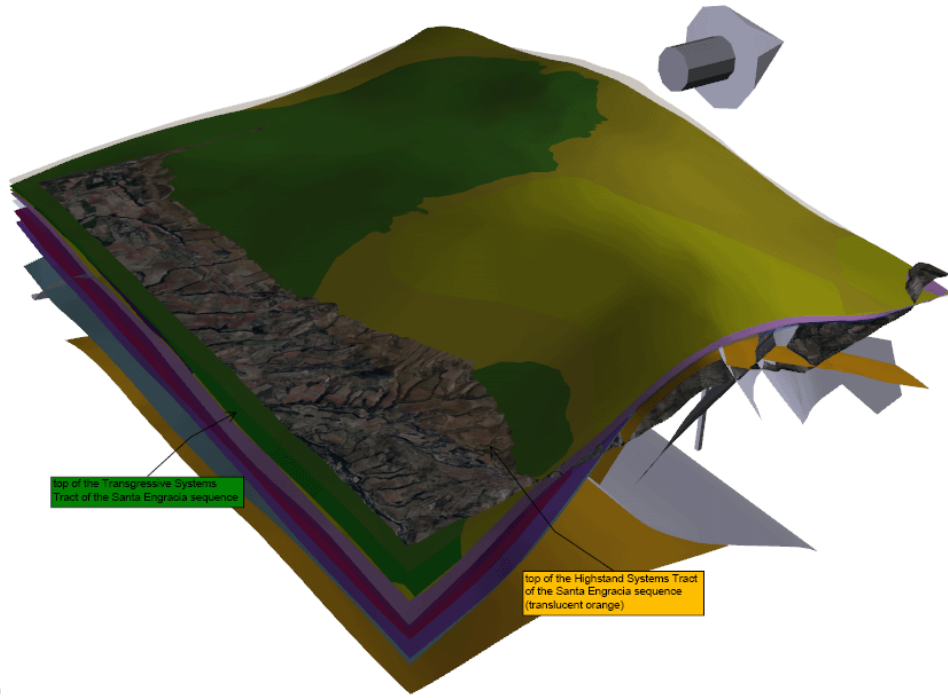
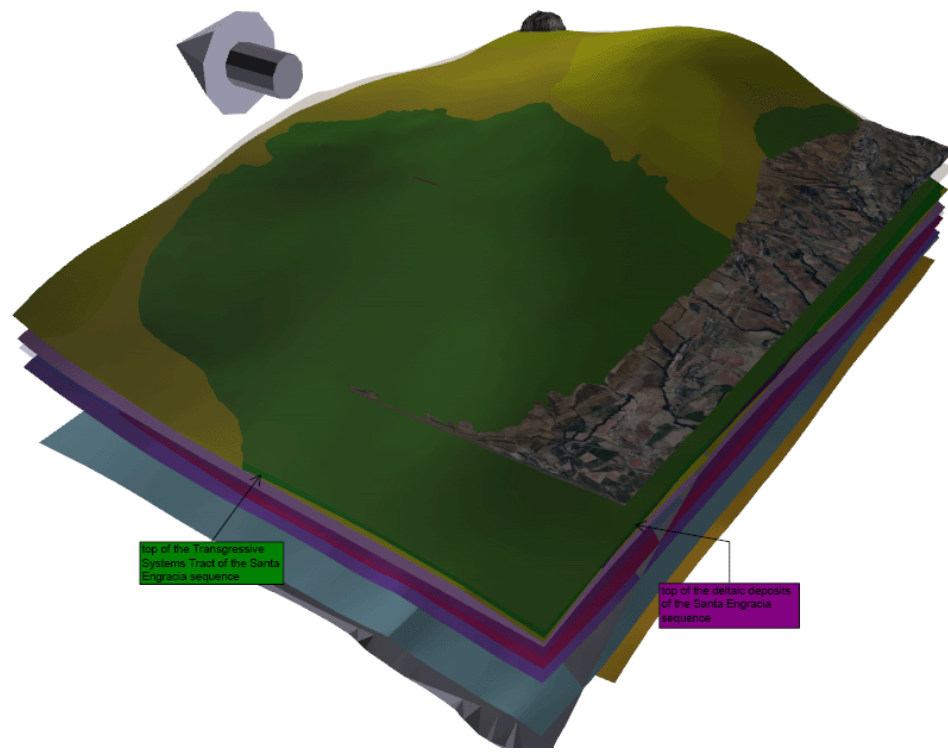


Figure 4.6 Orcau-Vell sequence. A) NW view, B) NE view.



A)



B)

Figure 4.7 Santa Engracia sequence. A) NW view, B) NE view.

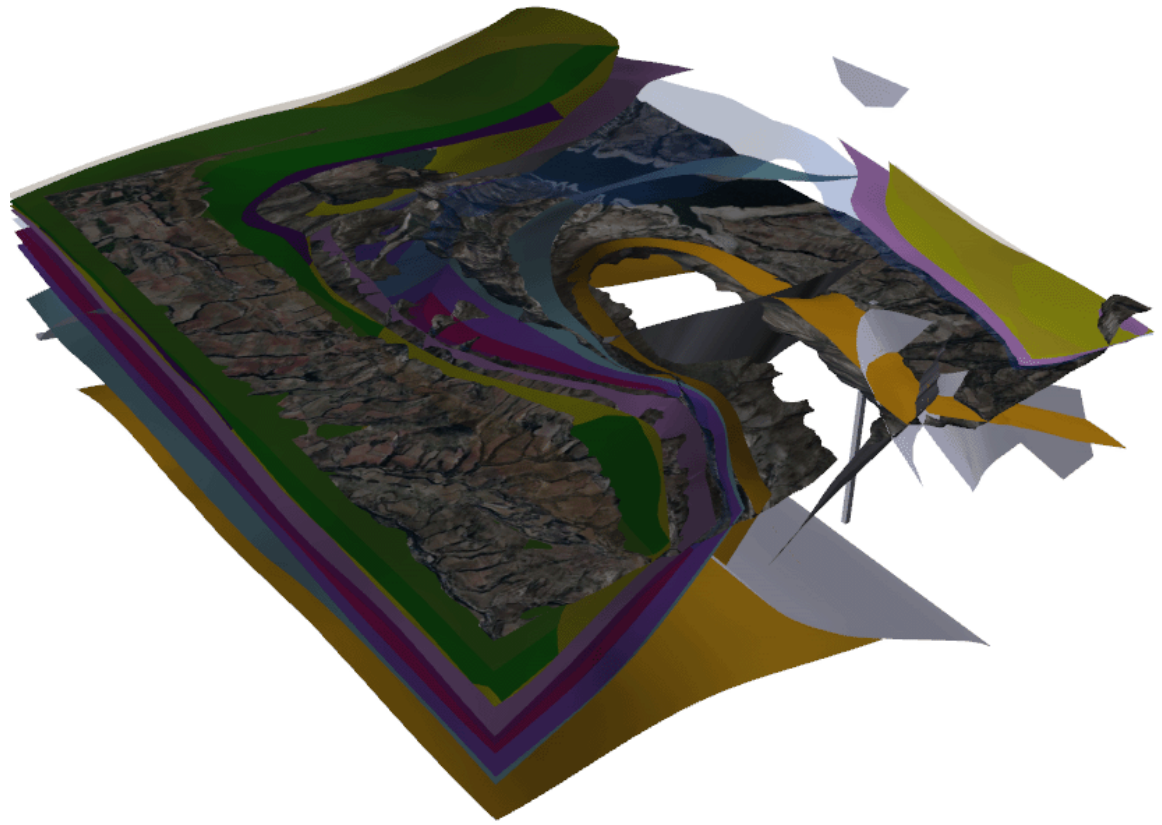
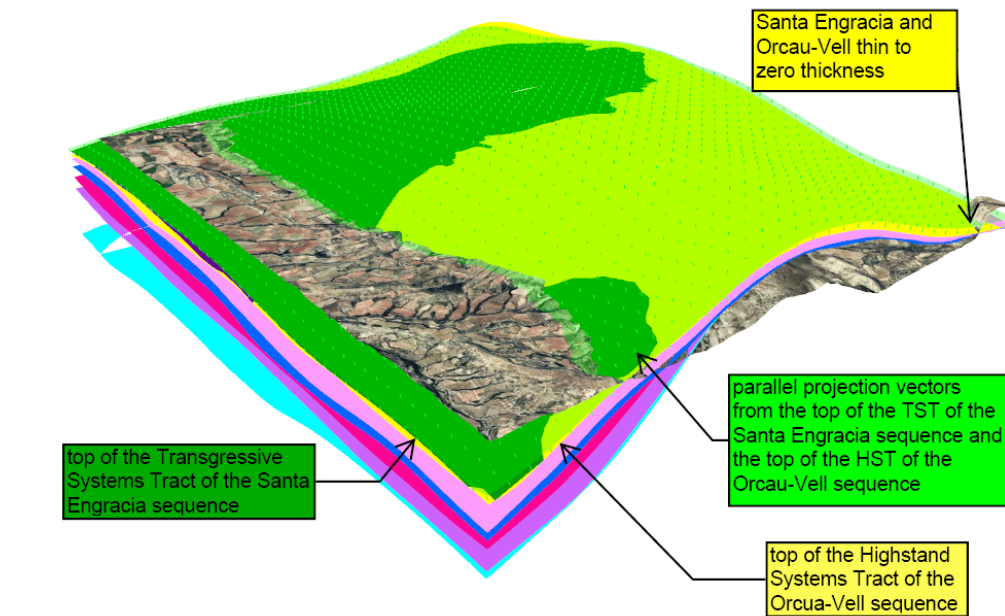
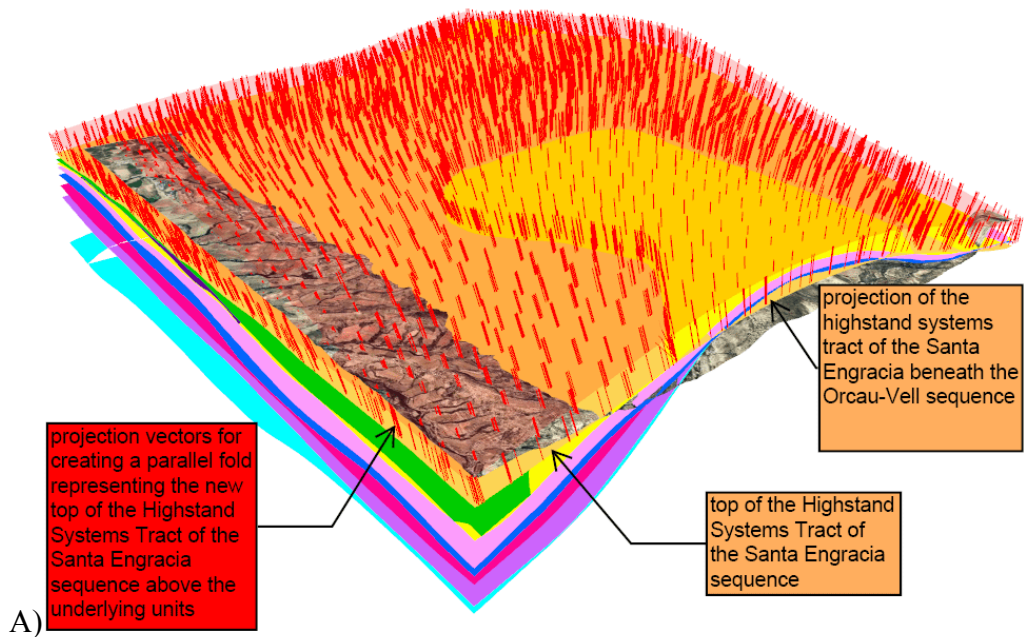


Figure 4.8 Horizontal slice showing the surface constraint on upwardly projected portions of the reconstruction (NW view).



B)

Figure 4.9 Creation of restoration surfaces. A) Projection vectors for creating a restoration surface representing the top of the Highstand Systems Tract of the Santa Engracia sequence. B) Projection vectors for creating a restoration surface representing the top of the Highstand Systems Tract of the Santa Engracia sequence.

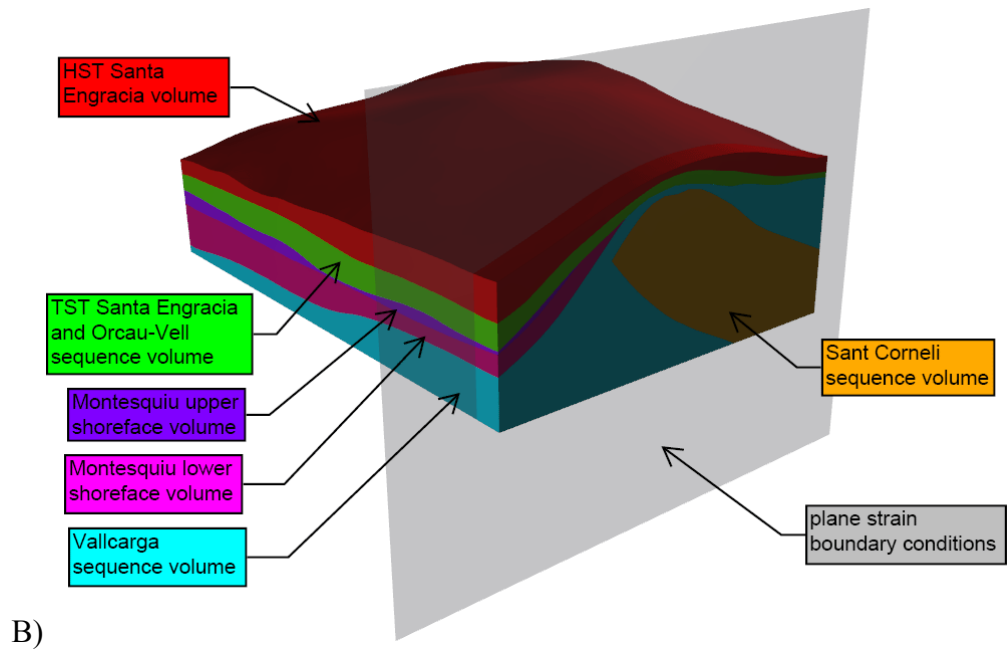
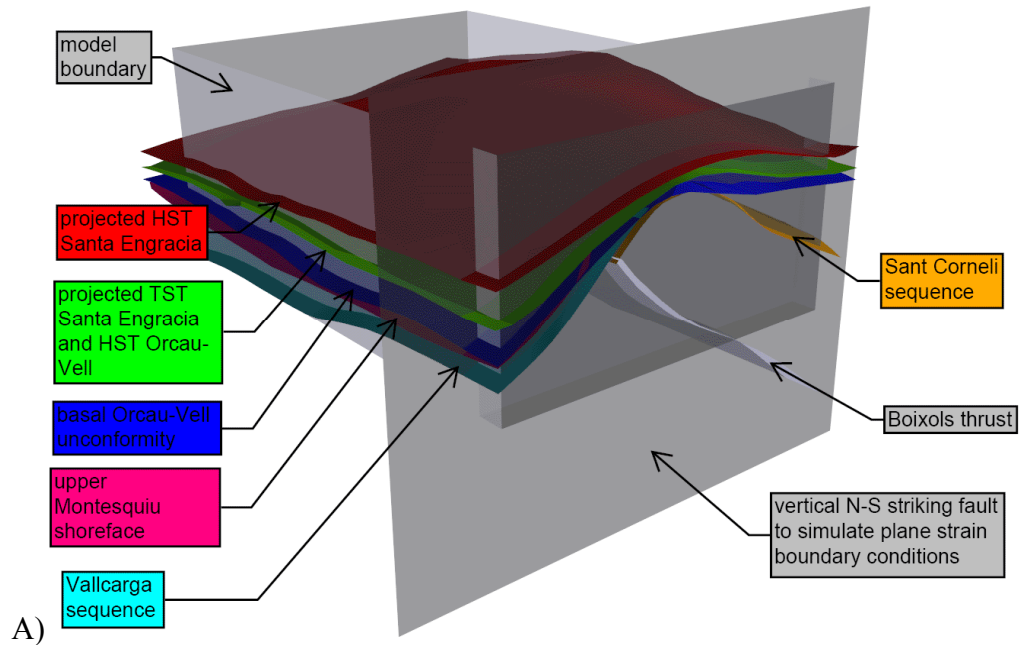


Figure 4.10 Setup for restoration step 1. A) Surfaces for finite element meshing of the first restoration step. B) Finite element volumes for the first restoration step.

Sequence	Young's Modulus (GPa)	Poisson's Ratio	Inferred lithology
Upper Santa Engracia	22	0.24	sandstone
Lower Santa Engracia and Orcau-Vell sequence	22	0.24	sandstone
Montesquiu sequence	22	0.24	sandstone
Vallcarga sequence	28	0.14	shale
Sant Corneli sequence	48	0.25	limestone

Table 4.1 Elastic parameters assigned to volumes in the restorations.

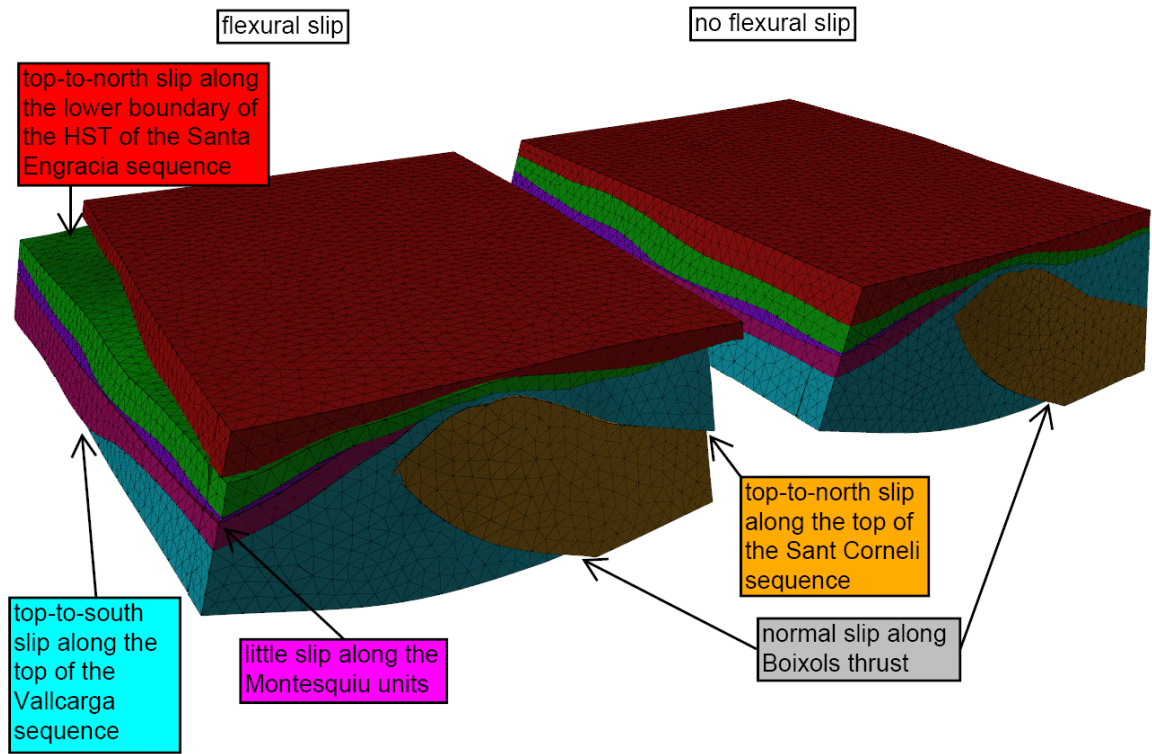


Figure 4.11 Restored geometries for the first restoration step showing the differences between flexural and no flexural slip conditions.

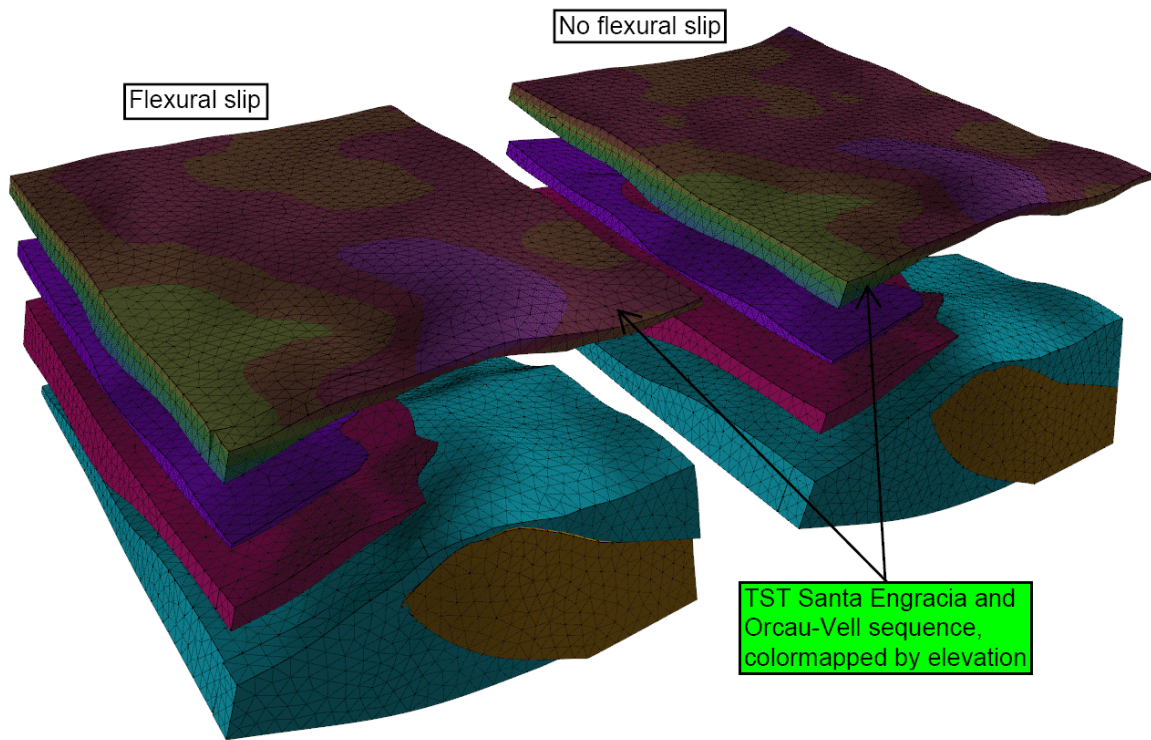


Figure 4.12 Expanded view of the restored geometries for the first restoration step with the upper Santa Engracia sequence removed. The elevation color map on the uppermost horizon shows the similarity in overall geometry between the two restorations despite the different boundary conditions.

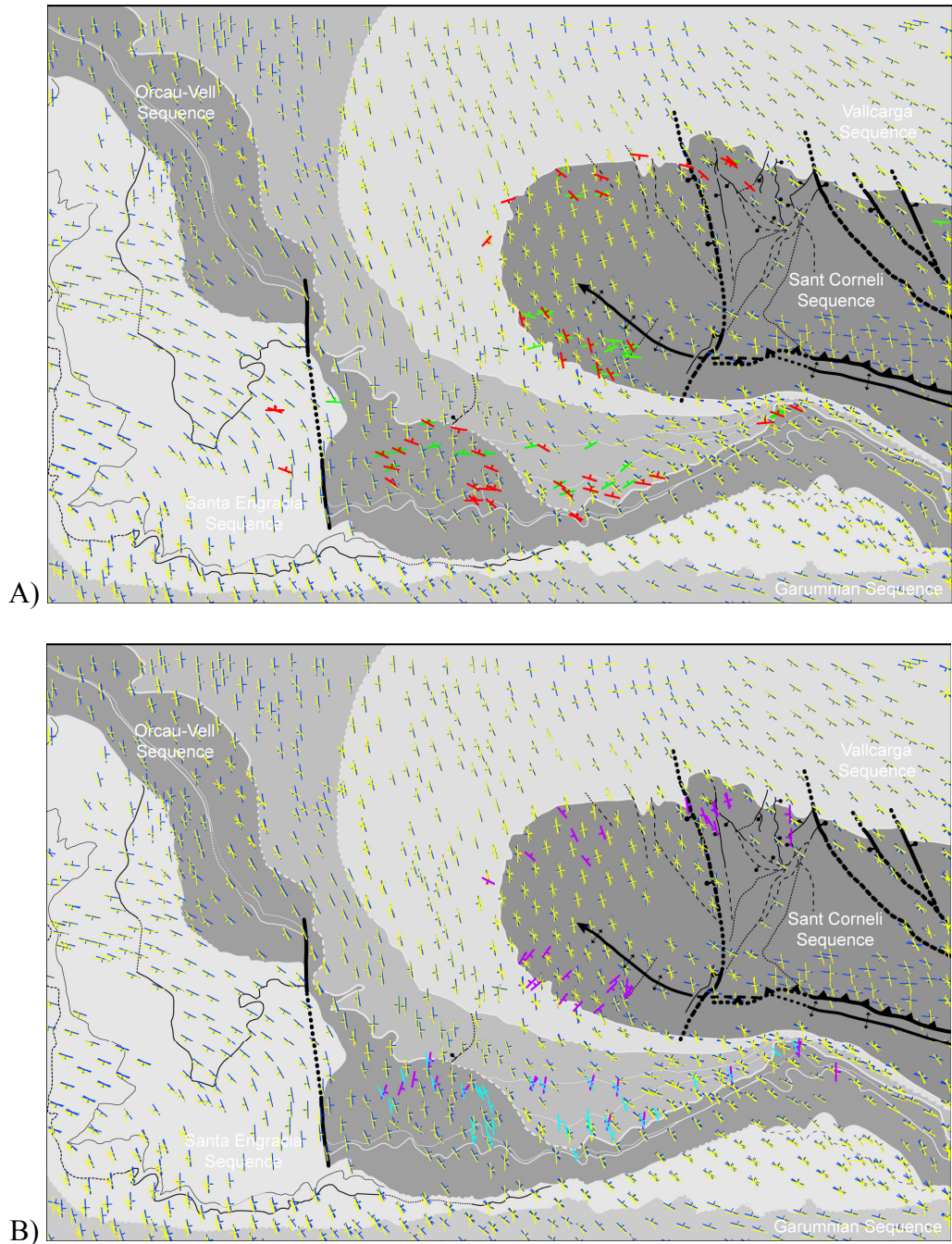


Figure 4.13 Comparison of fracture strike predictions from restoration step 1 to observed joint sets. Joint strike predictions from the non-flexural slip restoration are represented by blue dip symbols, and joint strike predictions from the flexural slip restoration are represented by the yellow dip symbols. The joint strikes shown are computed from vertices in the tetrahedral mesh that lie within 100 meters of the topographic surface. A) youngest joint sets: J4 joints are represented by red dip symbols, J5 joints are represented by green dip symbols. B) older joint sets J1/J3 joints are represented by purple dip symbols, J2 joints are represented by teal dip symbols.

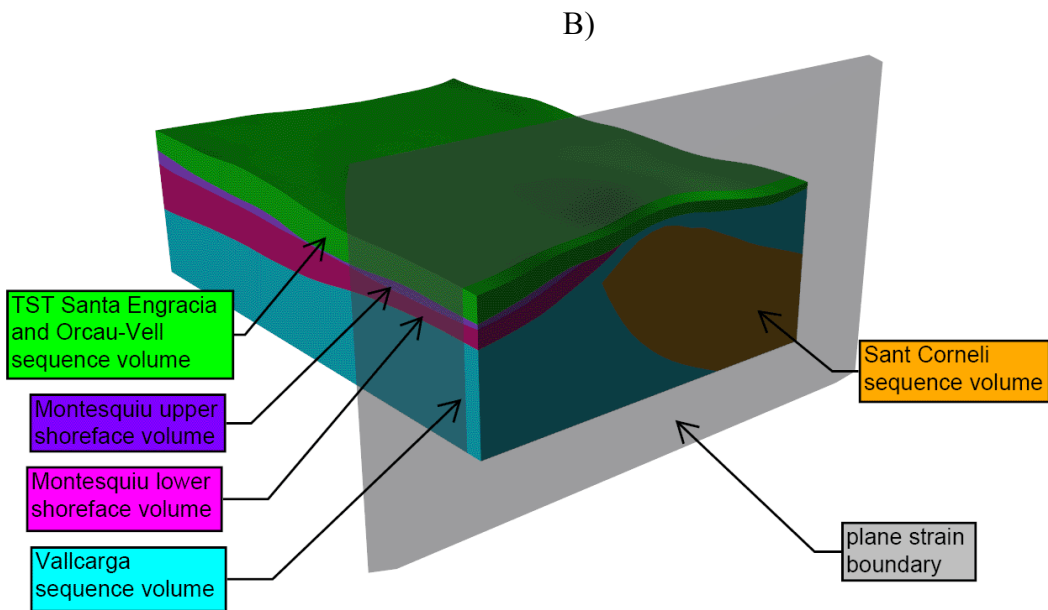
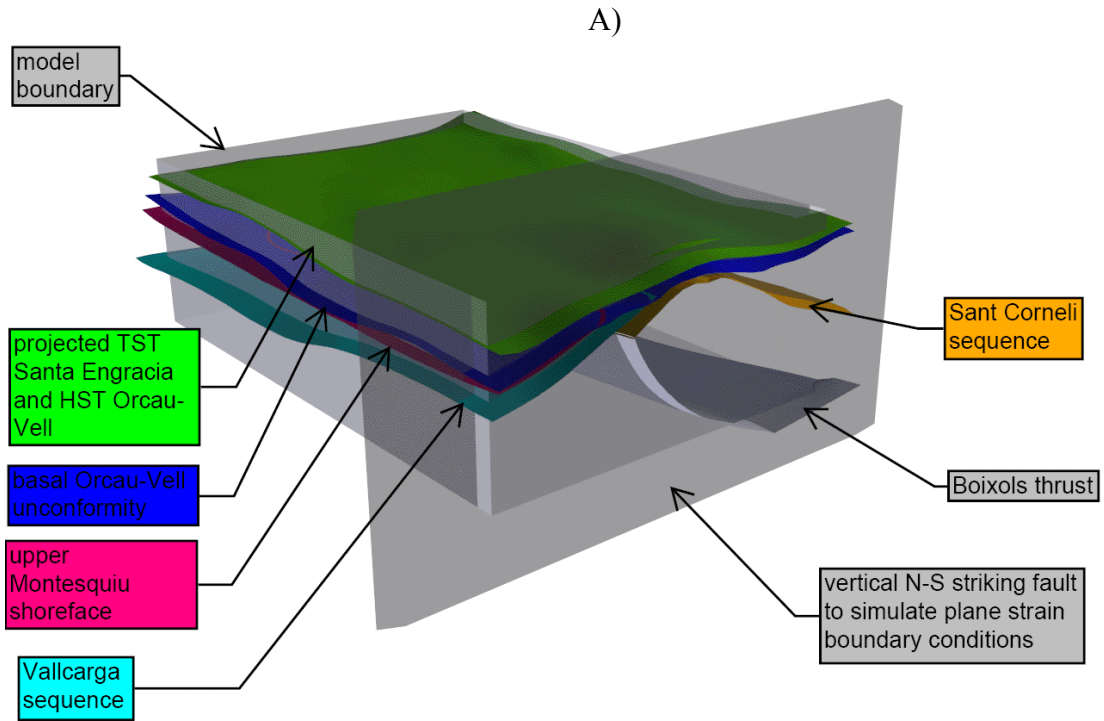


Figure 4.14 Setup for restoration step 2. A) Surfaces for finite element meshing of the second restoration step with no flexural slip. B) Finite element volumes for the second restoration step with no flexural slip.

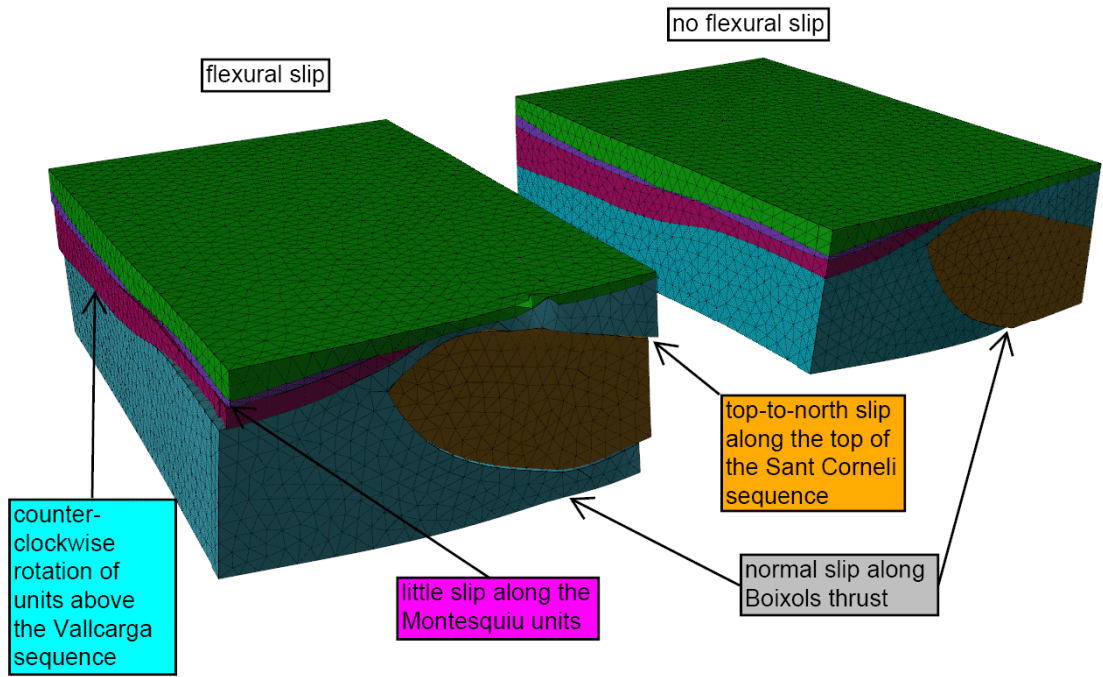


Figure 4.15 Restored geometries for the second restoration step showing the differences between flexural and no flexural slip conditions.

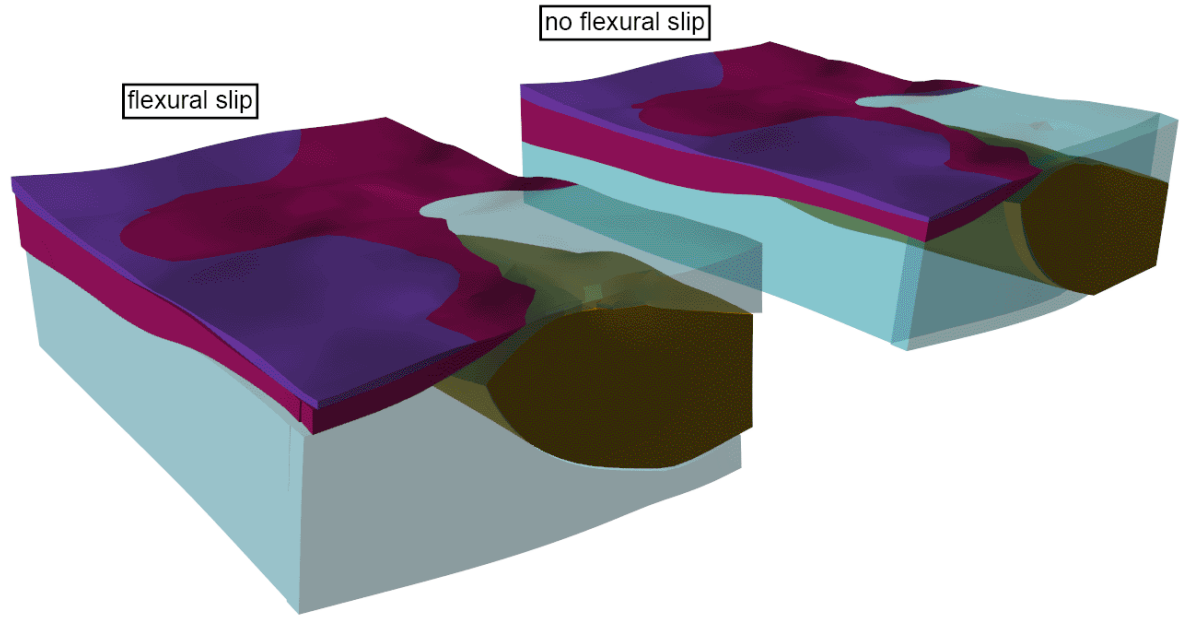


Figure 4.16 Restored geometries for the second restoration step with the lower Santa Engracia and Orcau-Vell sequences removed. The upper surface is the basal unconformity of the Orcau-Vell sequence. The Vallcarga sequence is translucent to show slight differences in the geometry of the Sant Corneli sequence.

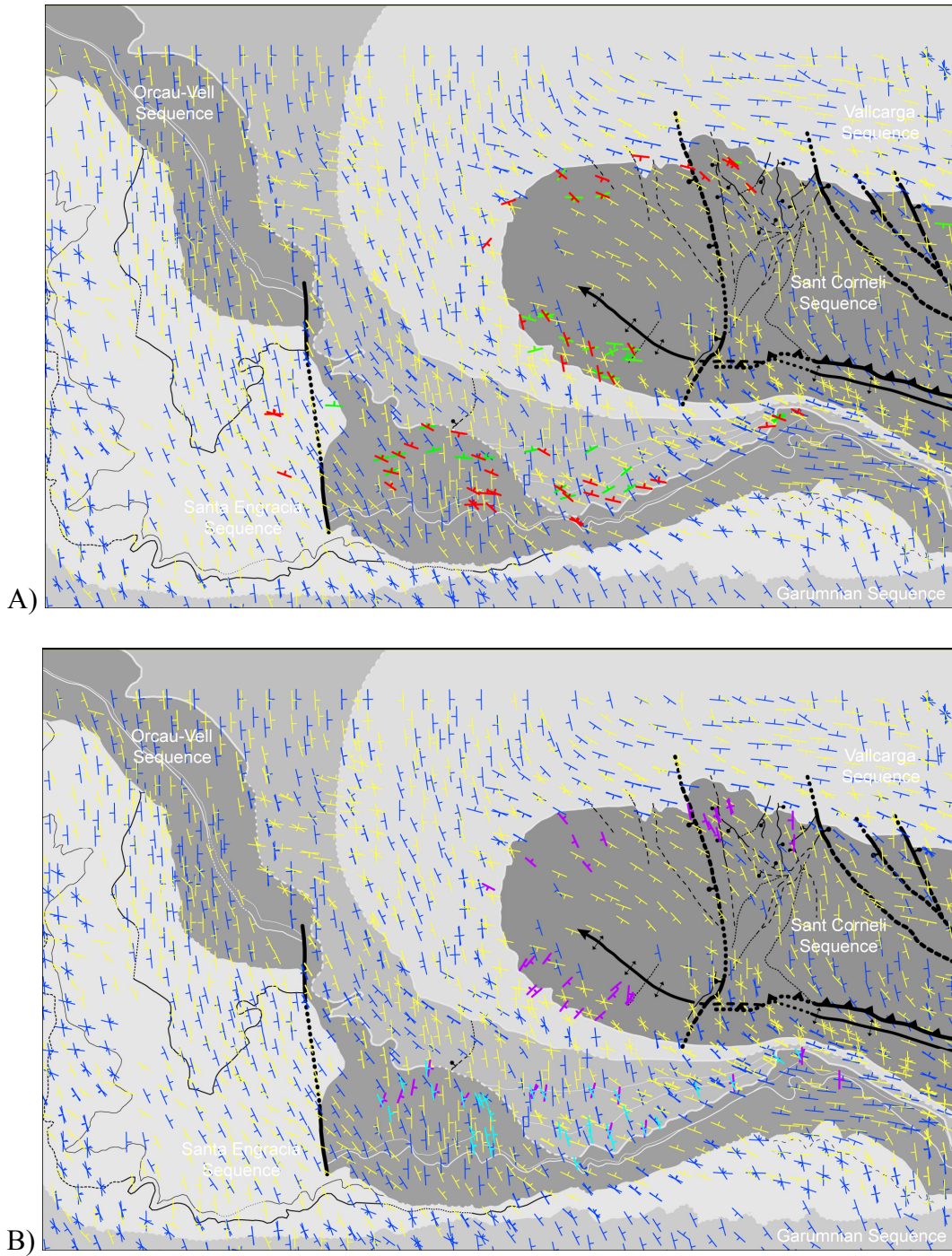


Figure 4.17 Comparison of fracture strike predictions from restoration step 2 to observed joint sets. Joint strike predictions from the non-flexural slip restoration are represented by blue dip symbols, and joint strike predictions from the flexural slip restoration are represented by the yellow dip symbols. A) youngest joint sets: J4 joints are represented by red dip symbols, J5 joints are represented by green dip symbols. B) older joint sets: J1/J3 joints are represented by purple dip symbols, J2 joints are represented by teal dip symbols.

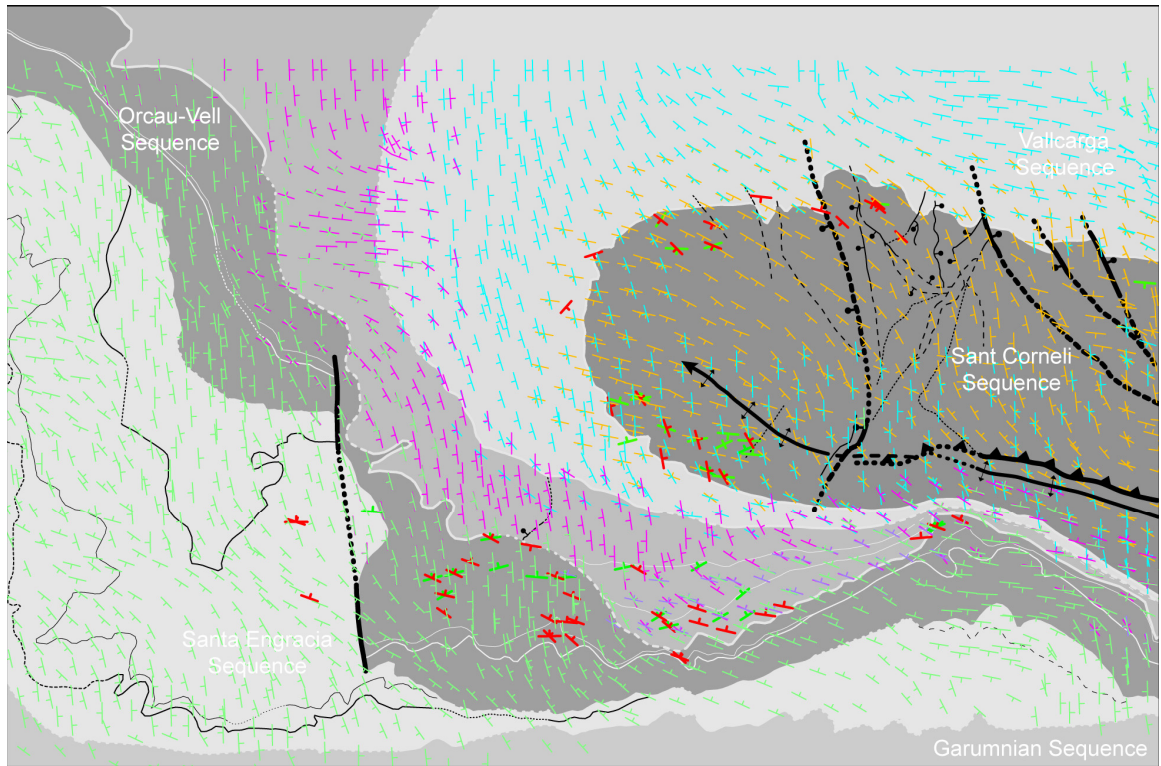


Figure 4.18 Comparison of fracture strike predictions from step 2 of the flexural slip restoration to young joint sets. Joint strike predictions from the flexural slip restoration are colored by sequence, with colors corresponding to those in Figs. 4.14 and 4.15. The joint strikes shown are computed from vertices in the tetrahedral mesh that lie within 200 meters of a topographic surface that has been restored to match the folded state of the second restoration step. J4 joints are represented by red dip symbols, J5 joints are represented by green dip symbols.

APPENDIX

**METHODOLOGY FOR SCHMIDT DATA COLLECTION AND CONVERSION
OF SCHMIDT REBOUND TO SHEAR MODULUS**

A.1 Introduction

This section explains the conversion of Schmidt hammer rebound number to shear modulus, and subsequently the determination of the rigidity contrast ratio in “Evidence for temporally changing mechanical stratigraphy and effects on joint-network architecture.” I also use this section to explain some of the errors and inaccuracies in the analysis. While the *in situ* measurements are problematic for precise absolute strength determination, the Schmidt hammer rebound number measured *in situ* can be used to establish relative strength among similarly weathered beds (Hucka 1965, Poole & Farmer 1980, Underwood et al. 2003).

A.2 Schmidt hammer sampling techniques

The greatest source of error in the *in situ* measurement of rock rigidity is related to the difficulty in obtaining representative rebound numbers. Nearby weaknesses such as fractures and bed planes as well as local surface irregularities can cause the apparent rigidity, measured by rebound, to be lower than the true rigidity. To eliminate the most significant contributors to these errors, sampling sites are chosen to avoid existing fractures and surface irregularities are removed with an abrasive stone. Additionally, Poole and Farmer (1980) recommends collecting five rebound measurements at each sampling locality and using the peak rebound number as representative of the rock strength/stiffness.

A.3 Correlation of Schmidt hammer rebound to Shear Modulus

The Schmidt hammer measures the rebound of a piston striking a surface, yielding a measure of the stiffness of that surface. In order to assess the rigidity contrast between beds, I need to convert these measured rebound values (R) to shear moduli. Deere and Miller (1966) published Schmidt hammer rebound values performed on cylindrical samples of a variety of different rock samples along with laboratory test results (e.g. Young's modulus, Poisson's ratio, dry unit weight) performed on those samples. Deere and Miller (1966) use this data to correlate rebound number and rock density (dry unit weight) to Young's modulus by calculating the best fitting curve through the data. Dry unit weight is considered in this analysis because I expect that the relationship between measured rebound and stiffness depends on the density of the rock.

Rather than using the general best fit determined by Deere and Miller (1966) for all lithologic types (igneous, metamorphic, and sedimentary), I calculate a linear regression using only the rebound and elastic moduli for the clastic sedimentary rocks published by Deere and Miller (1966). The values used for my conversion are shown converted to SI units in Table A1 below.

Heading:	Dry unit weight	Schmidt rebound	γ^2R	Young's Modulus	Poisson's ratio	Shear modulus
Symbol (units):	$\gamma^2(\text{g/cm}^3)$	R	$\frac{\gamma^2R (\text{g/cm}^3 * 10^4)}{}$	E (GPa)	(unitless)	μ (GPa)
<u>Rock Type and Locality</u>						
Berea ss, Amherst, Ohio	2.18	39	185.3	19.3	0.38	7.0
Crab orchard ss, Crossville, TN	2.53	44	281.6	39.2	0.46	13.4
Navajo ss, Glen Canyon, AZ	2.02	26	106.1	15.3	0.31	5.8
Siltstone, Hackensack, NJ	2.59	44	295.2	26.3	0.22	10.8

Table A1 Published Schmidt rebound, Dry unit weight, Young's modulus, and Poisson's Ratio Data for clastic sedimentary rocks (modified from Deere & Miller 1966).

Shear modulus (the rightmost column in Table A1) is calculated from Young's modulus, E, and Poisson's ratio, ν , using Equation 1.

$$\mu = \frac{E}{2(1 + \nu)} \quad (\text{Equation 1})$$

A correlation between shear modulus and γ^2R values is found using a linear regression that considers the dry unit weight of the sample, γ (Fig. A1).

$$\mu = 1.55 + 0.035\gamma^2R \quad (\text{Equation 2})$$

This regression introduces errors, largely because of the relatively few number of published values of hammer rebound values for samples whose elastic moduli are known. Additional data points on Figure A1 could better constrain the linear regression; however, augmenting the experimental database is both beyond my capabilities, and beyond the scope of my analysis.

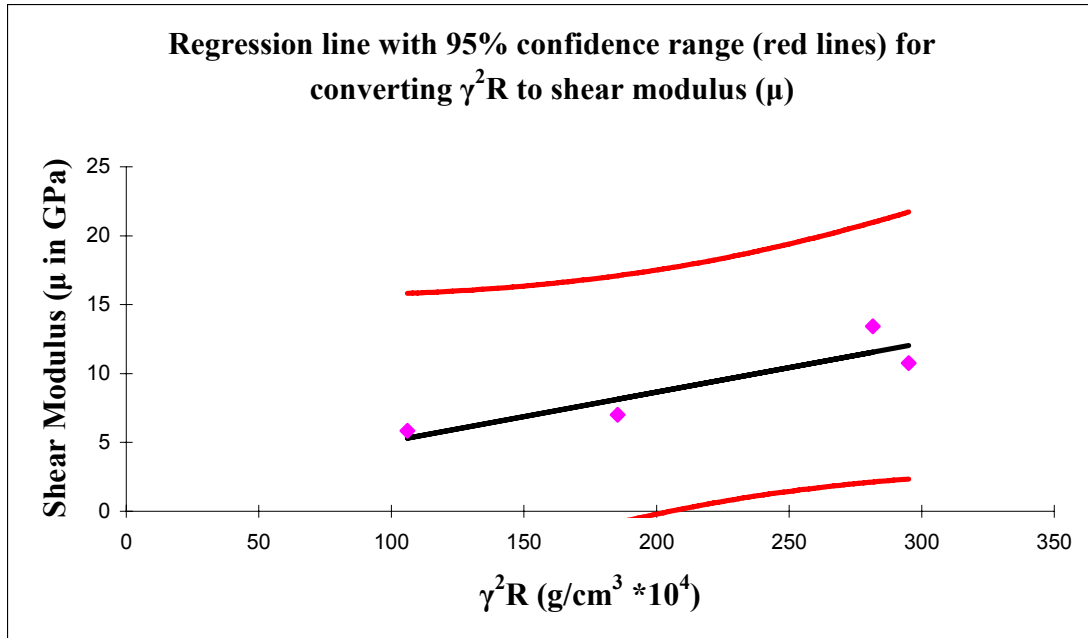


Figure A1 Regression line with 95% confidence range (red lines) for converting γ^2R to shear modulus (μ).

A.4 Conversion of Schmidt rebound at Oliana Anticline to shear modulus

I use the regression of Equation 2 to convert from measured rebound number to shear modulus. The ‘N-type’ rebound hammer that I used at Oliana anticline has greater energy release than the ‘L-Type’ hammer used by Deere and Miller (1966).

Consequently, I must add 7 rebound units (R) to my measured values (ELE International RM 710- Rock Classification hammer technical data). For this analysis I assume a dry unit weight of 2.5g/cm^3 for all of the sandstone and siltstone layers. The results of the conversion are shown in Figure 1.4 of the paper.

BIBLIOGRAPHY

- Ardévol, L., Klimowitz, J., Malagón, J. & Nagtegaal, P. J. C. 2000. Depositional Sequence Response to Foreland Deformation in the Upper Cretaceous of the Southern Pyrenees, Spain. *American Association of Petroleum Geologists Bulletin* **84**(4), 566-587.
- Bai, T., Maerten, L., Gross, M. R. & Aydin, A. 2002. Orthogonal cross joints; do they imply a regional stress rotation? *Journal of Structural Geology* **24**(1), 77-88.
- Banbury, N. 2001. The role of hanging-wall structure in thrust systems, examples from the South Pyrenean foreland fold and thrust belt, northern Spain. Unpublished Master of Research thesis, University of Edinburgh.
- Bellahsen, N. 2006. *The role of fractures in the structural interpretation of Sheep Mountain Anticline, Wyoming*. Elsevier : Oxford, International, International.
- Bellahsen, N., Fiore, P. E. & Pollard, D. D. 2006. From spatial variation of fracture patterns to fold kinematics; a geomechanical approach. In: *Geophysical Research Letters* **33**. American Geophysical Union : Washington, DC, United States, United States.
- Berástegui, X., García-Senz, J. M. & Losantos, M. 1990. Tecto-sedimentary evolution of the Organyà extensional basin (central south Pyrenean unit, Spain) during the Lower Cretaceous. *Bulletin de la Societe Geologique de France*(2), 264-251.
- Bergbauer, S. & Pollard, D. D. 2004. A new conceptual fold-fracture model including prefolding joints, based on the Emigrant Gap Anticline, Wyoming. In: *Geological Society of America Bulletin* **116**. Geological Society of America (GSA) : Boulder, CO, United States, United States, 294.
- Bernal, A. & Hardy, S. 2002. Syn-tectonic sedimentation associated with three-dimensional fault-bend fold structures; a numerical approach. *Journal of Structural Geology* **24**(4), 609-635.
- Birch, F. 1966. Compressibility; elastic constants, Sec 7. *Geological Society of America Memoir* **97**, 97-173.
- Bond, R. M. G. & McClay, K. R. 1995. Inversion of a Lower Cretaceous extensional basin, south central Pyrenees, Spain. *Geological Society Special Publications* **88**, 415-431.
- Buczowski, D. L. & Cooke, M. L. 2004. Compaction and shrinkage over buried impact craters: Implications for thickness and nature of cover material in Utopia Planitia, Mars. *Journal of Geophysical Research - Planetary* **109**(doi:10.1029/2003JE002144.).
- Burbank, D. W., Vergés, J., Muñoz, J. A. & Bentham, P. 1992. Coeval hindward and forward imbricating thrusting in the south-central Pyrenees, Spain: Timing and rates of shortening and deposition. *Geological Society of America Bulletin* **104**, 3-17.
- Chan, M. A., Beitler, B., Parry, W. T. & Ormo, J. 2004. A possible terrestrial analogue for hematite concretions on Mars. *Nature* **429**, 731-734.
- Chan, M. A., Johnson, C. M., Beard, B. L., Bowman, J. R. & Parry, W. T. 2006. Iron isotopes constrain the pathways and formation mechanisms of terrestrial oxide concretions; a tool for tracing iron cycling on Mars? *Geosphere*(7), 332-324.

- Chan, M. A., Parry, W. T., Petersen, E. U. & Hall, C. M. 2001. (super 40) Ar/ (super 39) Ar age and chemistry of manganese mineralization in the Moab and Lisbon fault systems, southeastern Utah. *Geology Boulder*(4), 334-331.
- Chapple, W. M. & Spang, J. H. 1974. Significance of Layer-Parallel Slip During Folding of Layered Sedimentary Rocks. *Geological Society of America Bulletin* **85**(10), 1523-1534.
- Chester, J. S., Logan, J. M. & Spang, J. H. 1991. Influence of layering and boundary conditions on fault-bend and fault-propagation folding. *Geological Society of America Bulletin, August* **103**(8), 1059-1072.
- Cook, T. S. & Erdogan, F. 1972. Stresses in bonded materials with a crack perpendicular to the interface. *International Journal of Engineering Science* **10**, 677-697.
- Cooke, M. L. 1997. Predicting fracture localization in folded strata from mechanical stratigraphy and fold shape; case study of East Kaibab Monocline, Utah. *International Journal of Rock Mechanics and Mining Sciences & Geomechanics Abstracts, June* **34**, 3-4.
- Cooke, M. L. & Kameda, A. 2002. Mechanical Fault Interaction within the Los Angeles Basin: A Two-Dimensional Analysis using Mechanical Efficiency. *Journal of Geophysical Research*.
- Cooke, M. L., Mollema, P., Pollard, D. D. & Aydin, A. 2000. Interlayer slip and joint localization in East Kaibab Monocline, Utah: Field evidence and results from numerical modeling. In: *Geological Society of London Special Publication on Forced Fold and Associated Fractures* (edited by Cosgrove, J. W. & Ameen, M. S.) **169**, London, 23-49.
- Cooke, M. L. & Pollard, D. D. 1997. Bedding-plane slip in initial stages of fault-related folding. *Journal of Structural Geology, April* **19**, 3-4.
- Cooke, M. L. & Underwood, C. A. 2001. Fracture termination and step-over at bedding interfaces due to frictional slip and interface opening. *Journal of Structural Geology* **23**, 223-228.
- Cooper, M. 1992. The analysis of fracture systems in surface thrust structures from the foothills of the Canadian Rockies. Chapman & Hall : London, United Kingdom, United Kingdom, 391.
- Corbett, K., Friedman, M. & Spang, J. 1987. Fracture development and mechanical stratigraphy of the Austin Chalk, Texas. *American Association of Petroleum Geologists Bulletin* **71**, 17-28.
- Cristallini, E. O. & Allmendinger, R. W. 2001. Pseudo 3-D modeling of trishear fault-propagation folding. *Journal of Structural Geology, December* **23**(12), 1883-1899.
- Crouch, S. L. 1979. Computer simulation of mining and faulted ground. *Journal of the South African Institute of Mining and Metallurgy* **79**, 159-173.
- Crouch, S. L. & Starfield, A. M. 1990. *Boundary element methods in solid mechanics*. Unwin Hyman, London.
- Cruikshank, K., Zhao, G., and Johnson, A. 1991. Analysis of minor fractures associated with joints and faulted joints. *Journal of Structural Geology*(865-886).
- Cuevas, J. L. 1992. Estratigrafía del "Garumniense" de la Conca de Tremp. Prepirineo de Lerida. *Acta Geologica Hispanica* **27**(1-2), 95-108.

- David, C., Menendez, B. & Bernabe, Y. 1998. The mechanical behavior of synthetic sandstone with varying brittle cement content. *International Journal of Rock Mechanics and Mining Sciences and Geomechanics Abstracts* **35**, 759-770.
- Davis, E. M. 2004. Do Joints Rotate with Lateral Fold Growth at Sheep Mountain Anticline, Wyoming. Unpublished M.S. Thesis, University of Massachusetts.
- Deere, D. U. & Miller, R. P. 1966. Engineering classification and index properties for intact rock. In: *Air Force Weapons Laboratory Technical Report AFWL-TR-65-116*, 277.
- Déramond, J. D., Souquet, P., Fondécave-Wallez, M. J. & Specht, M. 1993. Relationships between thrust tectonics and sequence stratigraphy surfaces in foredeeps: model and examples from the Pyrenees (Cretaceous-Eocene, France, Spain). In: *Tectonics and Seismic Sequence Stratigraphy* (edited by Williams, G. D. & Dobb, A.) **71**. Geological Society Special Publication, London, 193-219.
- Dhont, D., Luxey, P. & Chorowics, J. 2005. 3-D modeling of geologic maps from surface data. *American Association of Petroleum Geologists Bulletin* **89**(11), 1465-1474.
- Dunne, W. M., Ferrill, D. A., Crider, J. G., Hill, B. E., Waiting, D. J., La Femina, P. C., Morris, A. P. & Fedors, R. W. 2003. Orthogonal jointing during coeval igneous degassing and normal faulting, Yucca Mountain, Nevada. *Geological Society of America Bulletin* **115**, 1492-1509.
- Eberli, G. P., Baechle, G. T., Anselmetti, F. S. & Ince, M. L. 2003. Factors controlling elastic properties in carbonate sediments and rocks. In: *Carbonate geophysics* (edited by Dong, W., Tura, A. & Sparkman, G.) **22**. Society of Exploration Geophysics, The Leading Edge, Special Issue, 654-660.
- Engelder, G. a. P. 1997. *Joint development in clastic rocks of the Elk Basin anticline, Montana-Wyoming: an analysis of fracture spacing versus bed thickness in a basement involved Laramide structure*. Rocky Mountain Association of Geologists.
- Epard, J. L. & Groshong, R. H. 1995. Kinematic model of detachment folding including limb rotation, fixed hinges and layer-parallel strain. *Tectonophysics* **247**, 85-103.
- Erdogan, F. 1972. Fracture problems in composite materials. *Journal of Engineering and Fracture Mechanics* **4**, 811-840.
- Erickson, S. G. 1996. Influence of mechanical stratigraphy on folding vs. faulting. *Journal of Structural Geology* **18**, 443-450.
- Erslev, E. A. 1991. Trishear fault-propagation folding. *Geology* **19**, 617-620.
- Fernandez Bellon, O. 2004. Reconstruction of geological structures in 3D: an example from the Spanish Pyrenees. Unpublished PhD thesis, Universitat de Barcelona.
- Fischer, M. P. & Keating, D. P. 2005. Photogrammetric techniques for analyzing displacement, strain, and structural geometry in physical models; application to the growth of monoclinial basement uplifts. *Geological Society of America Bulletin, April* **117**, 3-4.
- Fischer, M. P. & Wilkerson, M. S. 2000. Predicting the orientation of joints from fold shape; results of pseudo-three-dimensional modeling and curvature analysis. *Geology Boulder, January* **28**(1), 15-18.

- Fisher, M. P., Woodward, N. B. & Mitchell, M. M. 1992. The kinematics of break-thrust folds. *Journal of Structural Geology* **14**, 451-460.
- Ford, M., Williams, E. A., Artoni, A., Vergés, J. & Hardy, S. 1997. Progressive evolution of a fault-related fold pair from growth strata geometries, Sant Llorenç de Morunys, SE Pyrenees. In: *Journal of Structural Geology* **19**. Pergamon : Oxford-New York, International, International, 413.
- García-Senz, J. 2002. Cuencas extensivas del Cretácico inferior en los Pirineos Centrales, formación y subsecuente inversión. Unpublished Ph.D. thesis, University of Barcelona, Spain.
- Garrido-Megías, A. & Ríos Aragües, L. M. 1972. Síntesis geológica del Secundario y Terciario entre los ríos Cinca y Segre (Pirineo Central de la vertiente sur pirenaica, provincias de Huesca y Lérida). *Boletín Geológico y Minero* **83**, 1-47.
- Grelaud, S., Malo, M., Vergés, J. & Taberner, C. 2003. Structure of the Boixols - Sant Corneli anticline (SE Pyrenees): Fractures and Fluid Flow. In: *AAPG International Conference* **87**. AAPG Bulletin, Barcelona, Spain.
- Griffiths, P., Jones, S., Salter, N., Schaefer, F., Osfield, R. & Reiser, H. 2002. A new technique for 3-D flexural-slip restoration. *Journal of Structural Geology* **24**(4), 773-782.
- Gross, M. R. 1995. Fracture partitioning: Failure mode as a function of lithology in the Monterey Formation of coastal California. *Geological Society of America Bulletin* **107**, 779-792.
- Gross, M. R., Fischer, M. P., Engelder, T. & Greenfield, R. J. 1995. Factors controlling joint spacing in interbedded sedimentary rocks: Integrating numerical models with field observations from the Monterey Formation, USA. In: *Fractography: Fracture topography as a tool in fracture mechanics and stress analysis* (edited by Ameen, M. S.) **92**. Geological Society Special Publication, London, 215-233.
- Guillaume, B., Dhont, D. & Brusset, S. 2008. Three-dimensional geologic imaging and tectonic control on stratigraphic architecture: Upper Cretaceous of the Tremp Basin (south-central Pyrenees, Spain). *American Association of Petroleum Geologists Bulletin* **92**(2), 249-269.
- Hanks, C. L., Lorenz, J., Teufel, L., and Krumhardt, A. 1997. Lithologic and Structural Controls on Natural Fracture Distribution and Behavior Within the Lisburne Group, Northeastern Brooks Range and North Slope Subsurface, Alaska. *American Association of Petroleum Geologists Bulletin* **81**(10), 1700-1720.
- Hanks, C. L., Parris, T. M. & Wallace, W. K. 2006. Fracture paragenesis and microthermometry in Lisburne Group detachment folds: Implications for thermal and structural evolution of the northeastern Brooks Range, Alaska. *American Association of Petroleum Geologists Bulletin* **90**(1), 1-20.
- Helgeson, D. E. & Aydin, A. 1991. Characteristics of joint propagation across layer interfaces in sedimentary rocks. *Journal of Structural Geology*. **13**, 897-911.
- Hennings, P. H., Olson, J. E. & Thompson, L. B. 2000. Combining outcrop data and three-dimensional structural models to characterize fractured reservoirs; an example from Wyoming. *AAPG Bulletin, June* **84**(6), 830-849.

- Holbrook, P. 2002. The primary controls over sediment compaction. In: *Pressure regimes in sedimentary basins and their prediction: American Association of Petroleum Geologists Memoir* (edited by Buffman, A. R. & Bowers, G.) **76**, 21-32.
- Houseknecht, D. W. 1987. Assessing the relative importance of compaction processes and cementation to reduction of porosity in sandstones. *American Association of Petroleum Geologists Bulletin* **71**, 633-642.
- Hucka, V. 1965. A rapid method of determining the strength of rocks in situ. *International Journal of Rock Mechanics and Mining Sciences* **2**, 127-134.
- International, E. RM 710- Rock Classification hammer technical data. Loveland, CO.
- Johnson, K. M. & Johnson, A. M. 2000. Localization of layer-parallel faults in San Rafael Swell, Utah and other monoclinial folds. *Journal of Structural Geology*, October **22**(10), 1455-1468.
- Johnson, K. M. & Johnson, A. M. 2002. Mechanical models of trishear-like folds. *Journal of Structural Geology* **24**(2), 277-287.
- Kirkwood, D., Ayt Ougougdal, M., Gayot, T., Beaudoin, G., and Pironon, J. 2000. Paleofluid-flow in a foreland basin, Northern Appalachians: from syntectonic flexural extension to Taconian overthrusting. *Journal of Gechemical Exploration* **69-70**, 269-273.
- Ladeira, F. L. & Price, N. J. 1981. Relationship between fracture spacing and bed thickness. *Journal of Structural Geology* **3**, 179-183.
- Lebraña, G. 2004. Evolució de fluids en un anticlinal. Unpublished M.S. Thesis thesis, University of Barcelona, Spain.
- Leftcariu, L., Eugene, P.C., Fischer, M.P., and Banner, J.L. 2005. Evolution of fluid compartmentalization in a detached fold complex. *Geology* **33**, 69-72.
- Lorenz, J. C., Sterling, J. L., Schechter, D. S., Whigham, C. L. & Jensen, J. J. 2002. Natural fractures in the Sprayberry Formation, Midland Basin, Texas: The effects of mechanical stratigraphy on fracture variability and reservoir behavior. *American Association of Petroleum Geologists Bulletin* **86**, 505-524.
- Maerten, F. & Maerten, L. 2006. Chronologic modeling of faulted and fractured reservoirs using a geomechanically based restoration: Technique and industry applications. *AAPG Bulletin* **90**(8), 1201-1226.
- Maerten, L. 1999. Mechanical interaction of intersecting normal faults; theory, field examples and applications. Unpublished Ph.D. thesis, Stanford University.
- Maerten, L., Gillespie, P., Pollard, D.D., 2001. Effect of local stress perturbation on secondary fault development. *Journal of Structural Geology* **24**, 145-153.
- Maerten, L., Pollard, D. D. & Karpuz, R. 2000. How to constrain 3-D fault continuity and linkage using reflection seismic data: a geomechanical approach. *AAPG Bulletin* **84**, 1311-1324.
- Maxwell, J. C. 1960. Experiments on compaction and cementation of sand. In: *Rock deformation: A symposium: Geological Society of America Memoir* (edited by Griggs, D. T.) **79**, 105-132.
- McGrath, A. G. & Davison, I. 1995. Damage zone geometry around fault tips. *Journal of Structural Geology* **17**, 1011-1024.

- Medwedeff, D. A. & Krantz, R. W. 2002. Kinematic and analog modeling of 3-D extensional ramps; observations and a new 3-D deformation model. *Journal of Structural Geology* **24**(4), 763-772.
- Mellere, D. 1993. Thrust generated, back-fill stacking of alluvial fan sequences, south-central Pyrenees, Spain (La Pobla de Segur Conglomerates). *International Association of Sedimentologists, Special Publication* **20**, 259-276.
- Moretti, I., Lepage, F. & Guiton, M. 2006. KINE3D: a New 3D Restoration Method Based on a Mixed Approach Linking Geometry and Geomechanics. *Oil & Gas Science and Technology* **61**(2), 277-289.
- Muñoz, J. A. 1992. Evolution of a continental collision belt. ECORS - Pyrenees crustal Balanced cross-section. In: *Thrust Tectonics* (edited by McClay, K. R.). Chapman & Hall, London, 235-246.
- Nagtegaal, P. J. C., Van Vliet, A., and Brouwer, J. 1983. Sytectonic coastal offlap and concurrent turbidite deposition: the upper Cretaceous Aren sandstone in the south-central Pyrenees, Spain. *Sedimentary Geology* **34**, 185-218.
- Narr, W. & Suppe, J. 1991. Joint spacing in sedimentary rocks. *Journal of Structural Geology* **13**, 1037-1048.
- Nelson, R. A. 1985. *Geological analysis of naturally fractured reservoirs*. Gulf Publishing Company, Houston, Texas.
- Nigro, F. & Renda, P. 2004. *Growth pattern of underlithified strata during thrust-related folding*. Elsevier : Oxford, International, International.
- Nino, F., Philip, H. & Chery, J. 1998. The role of bed-parallel slip in the formation of blind thrust faults. *Journal of Structural Geology, May* **20**(5), 503-516.
- Novoa, E., Suppe, J. & Shaw, J. H. 2000. Inclined-shear restoration of growth folds. *AAPG Bulletin* **84**(6), 787.
- Pavlis, T. L. & Bruhn, R. L. 1988. Stress history during propagation of a lateral fold-tip and implications for the mechanics of fold-thrust belts. *Tectonophysics, January* **145**, 1-2.
- Poblet, J. & McClay, K. 1996. Geometry and kinematics of single-layer detachment folds. *American Association of Petroleum Geologists Bulletin* **80**, 1085-1109.
- Poblet, J., Muñoz, J. A., Travé, A. & Serra-Kiel, J. 1998. Quantifying the kinematics of detachment folds using three-dimensional geometry; application to the Mediano Anticline (Pyrenees, Spain). *Geological Society of America Bulletin* **110**(1), 111-125.
- Pollard, D. D. & Aydin, A. 1988. Progress in understanding jointing over the past century. *Geological Society of America Bulletin* **100**, 1181-1024.
- Poole, R. W. & Farmer, L. W. 1980. Technical note: Consistency and repeatability of Schmidt hammer rebound data during field testing. *International Journal of Rock Mechanics and Mining Sciences and Geomechanics Abstracts* **17**, 167-171.
- Puigdefàbregas, C., Muñoz, J. A. & Vergés, J. 1992. Thrusting and foreland basin evolution in the Southern Pyrenees. In: *Thrust Tectonics* (edited by McClay, K.). Chapman & Hall, London, 247-254.
- Puigdefàbregas, C. & Soquet, P. 1986. Tecto-sedimentary cycles and depositional sequences of the mesozoic and tertiary from the Pyrenees. *Tectonophysics* **129**, 173-203.

- Quane, S. L. & Russell, J. K. 2002. Rock strength as a metric of welding intensity in pyroclastic deposits. *European Journal of Mineralogy* **15**, 855-864.
- Ramsay, J. G. & Huber, M. I. 1987. *The techniques of modern structural geology; Volume 2; Folds and Fractures*. Academic Press, London, United Kingdom.
- Renshaw, C. E. & Pollard, D. D. 1995. An experimentally verified criterion for propagation across unbounded frictional interfaces in brittle, linear elastic materials. *International Journal of Rock Mechanics and Mineral Sciences and Geomechanics Abstracts* **32**, 237-249.
- Rijken, P. & Cooke, M. L. 2001. Role of shale thickness on vertical connectivity of fractures: Application of crack-bridging theory to the Austin Chalk, Texas. *Tectonophysics* **337**, 117-133.
- Roest, W. R., and Srivastava, S.P. 1991. Kinematics of the plate boundaries between Eurasia, Iberia, and Africa in the North Atlantic from the late Cretaceous to the present. *Geology* **19**, 613-616.
- Rosell, J., Linares, R. & Llombart, C. 2001. El "Garumniense" Prepirenaico. *Rev. Soc. Geol. Espana* **14**(1-2), 47-56.
- Rouby, D., Xiao, H. & Suppe, J. 2000. 3-D restoration of complexly folded and faulted surfaces using multiple unfolding mechanisms. *AAPG Bulletin, June* **84**(6), 805-829.
- Rudnicki, J. W. & Wu, M. 1995. Mechanics of dip-slip faulting in an elastic half-space. *Journal of Geophysical Research* **100**(B11), 22173-22186.
- Salvini, F. & Storti, F. 2002. Three-dimensional architecture of growth strata associated to fault-bend, fault-propagation, and decollement anticlines in non-erosional environments. *Sedimentary Geology, January* **146**, 1-2.
- Savage, H. M. & Cooke, M. L. 2003. Can flat-ramp-flat fault geometry be inferred from fold shape? A comparison of kinematic and mechanical models. *Journal of Structural Geology* **25**, 2023-2034.
- Savage, H. M. & Cooke, M. L. 2004. The effect of non-parallel thrust fault interaction on fold patterns. *Journal of Structural Geology, May* **26**(5), 905-917.
- Shackleton, J. R. 2003. The Relationship between Fracturing, Asymmetric Folding, and Normal Faulting in Lisburne Group Carbonates: West Porcupine Lake Valley, Northeastern Brooks Range, Alaska. Unpublished Unpublished Masters Thesis thesis, University of Alaska.
- Simó, J. A. 1985a. Secuencias Depositionales del Cretacio superior de la Unidad del Montsec Pirineo Central. Unpublished Ph.D. thesis, University of Barcelona.
- Simó, J. A. 1989. Upper Cretaceous platform-to-basin depositional-sequence development, Tremp basin, south-central Pyrenees, Spain. In: *Controls on carbonate platforms and basin development* (edited by Crevello, P. D., Wilson, J.L., Sarg, J.F., and Read, J.F.) **44**. SEPM Special Publication, 365-378.
- Simó, J. A., Puigdefábregas, C., and Gili, E. 1985b. Transition from shelf to basin on an active slope, Upper Cretaceous Tremp area, southern Pyrenees. In: *International Association of Sedimentologists, Sixth European Regional Meeting: Excursion Guidebook* (edited by Mila, M. D., and Rosell, J.), 63-108.

- Specht, M., Deramond, J. & Souquet, P. 1991. Relations tectonique-sédimentation dans les bassins d'avant-pays; utilisation des surfaces stratigraphiques isochrones comme marqueurs de la déformation. *Bulletin de la Société Géologique de France* **162**(3), 562-553.
- Stearns, D. W. 1967. Certain aspects of fractures in naturally deformed rocks. In: *NSF advanced science seminar in rock mechanics* (edited by Riecker, R. E.). Air Force Cambridge Research Lab Report, Bedford, MA, 97-118.
- Stearns, D. W. & Friedman, M. 1972. Reservoirs in Fractured Rock. *Memoir American Association of Petroleum Geologists* **16**(10), 82-106.
- Strayer, L. M. & Suppe, J. 2002. Out-of-plane motion of a thrust sheet during along-strike propagation of a thrust ramp; a distinct-element approach. *Journal of Structural Geology* **24**(4), 637-650.
- Suppe, J. 1983. Geometry and kinematics of fault-bend folding. *American Journal of Science* **283**, 684-721.
- Suppe, J. & Medwedeff, D. A. 1990. Geometry and kinematics of fault-propagation folding. *Ecologiae Helvetiae* **83**, 409-454.
- Sussman, A. J. 2002. Thrust belt curvature: Structural and paleomagnetic analyses in the Catalunyan Pyrenees and Sevier orogen. Unpublished Ph.D. thesis, University of Arizona.
- Szilard, R. 1974. *Theory and analysis of plates: classical and numerical methods*. Prentice Hall.
- Thibert, B., Gratier, J.-P. & Morvan, J.-M. 2005. A direct method for modeling and unfolding developable surfaces and its application to the Ventura Basin, California. *Journal of Structural Geology* **27**(2), 303-316.
- Thomas, A. L. 1994. POLY3D: A Three-Dimensional, Polygonal Element, Displacement Discontinuity Boundary Element Computer Program with Applications to Fractures, Faults, and Cavities in the Earth's Crust. Unpublished MS thesis, Stanford University.
- Underwood, C. A., Cooke, M. L., Simó, J. A. & Muldoon, M. A. 2003. Stratigraphic controls on vertical fracture patterns in Silurian dolomite, northeastern Wisconsin. *American Association of Petroleum Geologists Bulletin* **87**, 121-142.
- Van Hoorn, B. 1970. Sedimentology and Paleogeography of an upper Cretaceous turbidite basin in the South-Central Pyrenees, Spain. *Leidse Geologische Mededelingen* **45**, 73-154.
- Vasconcelos, P. M. 1999. K-Ar and (super 40) Ar/ (super 39) Ar geochronology of weathering processes. *Annual Review of Earth and Planetary Sciences*, 229-183.
- Vergés, J. 1993. Estudi geològic del versant sud del Pirineu oriental i central: Evolució cinemàtica en 3D. Unpublished Ph.D. thesis, University of Barcelona, 203 p.
- Vergés, J., Burbank, D. W. & Meigs, A. 1996. Unfolding; an inverse approach to fold kinematics. In: *Geology Boulder* **24**. Geological Society of America (GSA) : Boulder, CO, United States, United States, 175.
- Vergés, J. & Muñoz, J. A. 1990. Thrust sequence in the southern central Pyrenees. *Bulletin de la Société Géologique de France* **6**, 265-271.